Fine structure of tremor migrations beneath the Kii Peninsula, Southwest Japan, extracted with a space-time Hough transform

Kodai Sagae[1], Hisashi Nakahara[2], Takeshi Nishimura[3], and Kazutoshi Imanishi[1]

[1]Geological Survey of Japan, AIST
[2]Unknown
[3]Tohoku University

December 14, 2022

Abstract

Tectonic tremors occurring on subducting plate boundaries are known to migrate at various timescales and migration speeds. Spatiotemporal patterns of tremor migration are key to investigating the rupture growth of slow earthquakes. However, spatiotemporal patterns are not sufficiently simple to visually define tremor migrations. This study developed a space-time Hough transform to objectively extract tremor migrations. The space-time Hough transform enables the extraction of multiple tremor migrations with various durations, migration directions, and migration speeds. We applied this method to a catalog of tremors for the period from 2012 to 2014, which was determined from the data analysis of a dense seismic array deployed in the Kii Peninsula, Southwest Japan. We successfully extracted 1,010 tremor migrations with durations ranging from 10 min to 24 h. Along-strike migrations propagating southwestward were predominant in the northeastern part of the Kii Peninsula, whereas those propagating northeastward were principal in the southwestern part. Regarding the along-dip direction, tremor migrations propagating in the up-dip directions were predominant in the deep part, and those propagating in the down-dip directions were principal in the shallow part. The patterns of along-strike migrations were related to the distribution of tremor energies, suggesting that tremor migrations may be controlled by heterogeneous structures of frictional properties on the plate interface. We further found that the migration speed is proportional to the inverse of the square root of the duration. This relation implies that a diffusion process controls the growth of fault ruptures behind tremor migrations.

Fine structure of tremor migrations beneath the Kii Peninsula, Southwest Japan, extracted with a space-time Hough transform

Kodai Sagae[1,2]*, Hisashi Nakahara[1], Takeshi Nishimura[1], and Kazutoshi Imanishi[3]

[1]Department of Geophysics, Graduate School of Science, Tohoku University, 6-3, Aramaki Aza-Aoba, Aoba-ku, Sendai, Miyagi, 980-8578, Japan.

[2]Now at Geological Survey of Japan, National Institute of Advanced Industrial Science and Technology (AIST), Tsukuba Central 7, 1-1-1 Higashi, Tsukuba, Ibaraki, 305-8567, Japan.

[3]Geological Survey of Japan, National Institute of Advanced Industrial Science and Technology (AIST), Tsukuba Central 7, 1-1-1 Higashi, Tsukuba, Ibaraki, 305-8567, Japan.

Corresponding author: Kodai Sagae (k.sagae@aist.go.jp)

Key Points:

- We developed a new method using a space-time Hough transform to objectively extract tremor migrations.
- Tremor migrations show fine structures in which multiple short-duration tremor migrations occur during long-duration tremor migration.
- The relation between migration speed (V_{mi}) and duration (T) follows $V_{mi} \propto T^{-0.5}$.

Abstract

Tectonic tremors occurring on subducting plate boundaries are known to migrate at various timescales and migration speeds. Spatiotemporal patterns of tremor migration are key to investigating the rupture growth of slow earthquakes. However, spatiotemporal patterns are not sufficiently simple to visually define tremor migrations. This study developed a space-time Hough transform to objectively extract tremor migrations. The space-time Hough transform enables the extraction of multiple tremor migrations with various durations, migration directions, and migration speeds. We applied this method to a catalog of tremors for the period from 2012 to 2014, which was determined from the data analysis of a dense seismic array deployed in the Kii Peninsula, Southwest Japan. We successfully extracted 1,010 tremor migrations with durations ranging from 10 min to 24 h. Along-strike migrations propagating southwestward were predominant in the northeastern part of the Kii Peninsula, whereas those propagating northeastward were principal in the southwestern part. Regarding the along-dip direction, tremor migrations propagating in the up-dip directions were predominant in the deep part, and those propagating in the down-dip directions were principal in the shallow part. The patterns of along-strike migrations were related to the distribution of tremor energies, suggesting that tremor migrations may be controlled by heterogeneous structures of frictional properties on the plate interface. We further found that the migration speed is proportional to the inverse of the square root of the duration. This relation implies that a diffusion process controls the growth of fault ruptures behind tremor migrations.

Plain Language Summary

Tectonic tremors, which are continuous seismic signals with a predominant frequency of 2–8 Hz, have been discovered in subduction zones worldwide. The tremor activity continues for several hours to days, and source locations migrate at speeds ranging from 10 km/day to 1,000 km/day. Tremor migrations provide us with key to understanding the associated fault ruptures. However, their durations, migration directions, and migration speeds have variations that are too large to be characterized visually. Therefore, it is necessary to objectively extract the characteristics of tremor migrations. We developed a space-time Hough transform to extract tremor migrations and applied it to data from a tremor catalog in the Kii Peninsula, Southwest

Japan. We extracted 1,010 tremor migrations with durations ranging from 10 min to 24 h. The tremor migrations consist of long-duration migrations at slow speeds and short-duration migrations at high speeds. The migration speeds decreased as the durations increased, suggesting that there was a diffusive process behind tremor migrations. We identified four areas where tremor migration was active. Migration patterns are different in each area and are related to the distribution of tremor energies. The results suggest that the migration patterns may reflect the frictional properties of the plate interface.

Keywords: Tectonic tremor, Tremor migration, space-time Hough transform, Kii Peninsula, Rapid tremor reversal (RTR), slow earthquakes

1 Introduction

Slow earthquakes are phenomena in which fault ruptures grow more slowly than regular earthquakes and have been observed in subduction zones worldwide (e.g., Obara & Kato, 2016; Schwarz & Rokosky, 2007). Events with various durations detected using geodetic and seismic data are categorized as slow earthquakes: low-frequency earthquake (LFE), tectonic tremor, very low-frequency earthquake (VLFE), and slow slip event (SSE) (Obara & Kato, 2016). These events occur in the deep or shallow extensions of megathrust-locked zones. Some previous studies have detected slow earthquakes in advance of megathrust earthquakes (e.g., Ito et al., 2013; Kato et al., 2012; Radiguet et al., 2016; Socquet et al., 2017). Therefore, it is important to understand the physical processes of slow earthquakes and their connection to megathrust earthquakes.

Slow earthquakes have a significant characteristic that the source locations migrate (e.g., Hirose & Obara, 2010; Shelly et al., 2007; Takemura et al., 2019). Tremor migrations are known to exhibit the following characteristics depending on the timescale. Tremor migration with a duration ranging from several hours to days is one of the major characteristics, and this tremor migration is referred to as the main front in the present study. The main front propagates along the strike of the subducting plate at a speed of approximately 10 km/day (e.g., Houston et al., 2011; Obara, 2010). On a timescale of several hours, tremor migration at a speed of approximately 100 km/day propagates in the reverse direction of the main front, which is called rapid tremor reversal (RTR) (Houston et al., 2011). A tremor streak is a tremor migration that propagates parallel to the subducting direction at a speed of approximately 1,000 km/day on a timescale of several hours (e.g., Ghosh et al., 2010; Shelly et al., 2007). Fault ruptures of SSEs are suggested to occur behind these tremor migrations because slow earthquakes occur simultaneously (e.g., Hirose & Obara, 2010). Spatiotemporally coupled slow earthquakes are referred to as episodic tremor and slip (ETS) (Rogers & Dragert, 2003). Therefore, by assuming an ETS, it may be possible to investigate SSEs from tremor migrations (Bletery et al., 2017). Tremor migration is key to understanding the growth of fault ruptures of slow earthquakes.

Tremor migrations have been discussed as the spatiotemporal evolutions of source locations projected on the axis along the strike of a subducting plate (e.g., Houston et al., 2011; Obara, 2010). However, when we discuss the patterns of tremor migrations in detail, it is not sufficient to investigate the spatiotemporal evolutions of tremor migrations only along the strike axis. We must consider the spatiotemporal changes on an axis perpendicular to the along-strike axis as well. Moreover, because tremor migrations show complex spatiotemporal structures (e.g., Houston et al., 2011; Sagae et al., 2021), we need to develop a method to objectively extract tremor migrations and investigate their fine structures. Previous studies have developed methods for automatically extracting tremor migrations. Obara et al. (2012) extracted tremor migrations beneath the Kii Peninsula in Southwest Japan by using a two-step process. First, a linear trend was extracted from a spatiotemporal plot of tremor locations projected on the along-strike axis. Second, a tremor migration was extracted by applying the principal component analysis to the data for tremor locations and occurrence times. Bletery et al. (2017) extracted tremor migrations in Cascadia by using a different two-step process from Obara et al. (2012). In the first step, a clustering process was performed to identify clusters of tremor events and their durations. In the next step, they extracted a tremor migration in the cluster by applying linear regression to spatiotemporal plots of tremor locations projected on multiple axes.

These previous studies commonly estimated tremor migrations using linear regression on the projected axis. Thus, their methods are constrained in that there is only one migration in one time window or one cluster. To investigate the fine structures of tremor migrations, a method to extract multiple tremor migrations, regardless of the lengths of the time windows and projected axes, is necessary. Therefore, in the present study, we developed a space-time Hough transform to objectively extract tremor migrations and applied the method to data of tectonic tremors beneath the Kii Peninsula, Southwest Japan. We investigated the spatial characteristics of tremor migrations and discussed the factors controlling the growth of tremor migrations.

2 Data and Method

2.1 Data of tremor catalog

We used a catalog of tremors determined using a dense seismic array on the Kii Peninsula, Southwest Japan (Sagae et al., 2021). The catalog contained 25,155 tremor events that occurred between July 2012 and July 2014 (Figure 1). Tremor locations were determined by backprojection onto the interface of the Philippine Sea Plate (Hirose et al., 2008), and the number of detections was 2.2 times more than that obtained by the envelope correlation method (Obara, 2002) using network stations (Imanishi et al., 2011). The temporal resolution of the catalog was 1 min, and the uncertainty of the horizontal location was approximately 2.0 km on average. The tremor locations showed a belt-like distribution along the strike at depths of 30–35 km (Figure 1a). The present study defined the region where the tremor events occur as the tremor zone. We clearly observed the locations where the number of tremor events was high or low (Figure 1b). During the two years, 12 tremor episodes with durations longer than 12 h were detected, in which various tremor migrations (e.g., RTR, tremor streak) were observed.

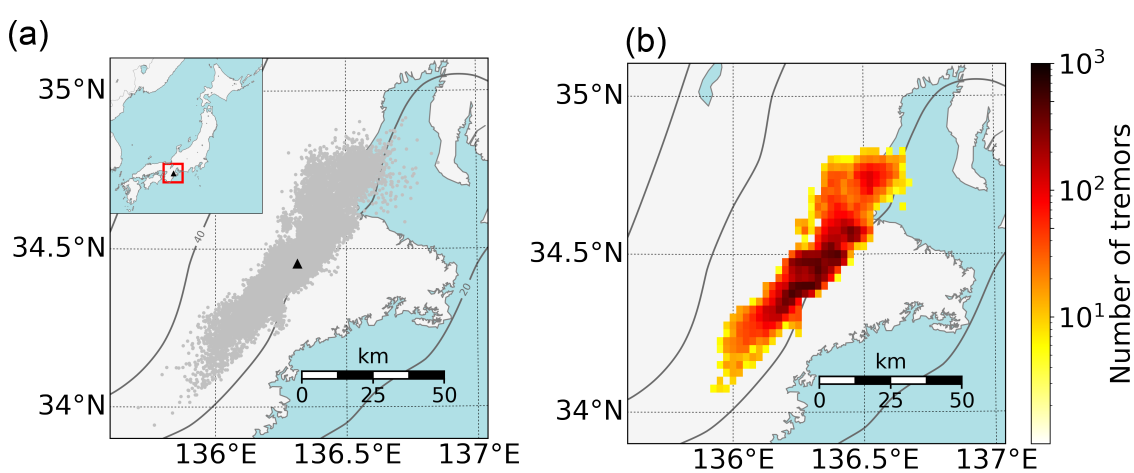

Figure 1. (**a**) Distribution of tremor locations beneath the Kii Peninsula, Southwest Japan from July 2012 to July 2014. The gray dots show tremor locations, and the black triangle shows the location of the seismic array. The solid curves show depth contours of the Philippine Sea Plate

(Hirose et al., 2008). (**b**) The number of tremor events. Colors show the cumulative number of tremor events inside cells separated by intervals of 0.025° along longitude and latitude.

2.2 Space-time Hough transform

We focused on the Hough transform (Hough, 1962) for extracting multiple tremor migrations in one time window. The Hough transform is an image-processing technique that can extract straight lines from a 2-D image. In the 2-D Hough transform, any straight line is represented by $\rho = x \cos\theta + y \sin\theta$, where x and y are the locations of an event point, ρ is the distance from the origin to the straight line, and θ is the direction of perpendicular to the straight line. Some combinations of (ρ, θ) express straight lines with different slopes that pass through an event point (x, y). These combinations of (ρ, θ) constitute a sine curve in the space of (ρ, θ). The best straight line is extracted by searching for the combination of (ρ, θ) where the sine curve calculated for each event point intersects the most. A technique of counting the number of intersections is called "vote". Even if there are multiple straight lines in a 2-D image, the method can distinguish these lines as different combinations of (ρ, θ). Therefore, the 2-D Hough transform enables us to extract multiple straight lines from the image by the technique of "vote". The Hough transform in 3-D space can be used to extract planes. In seismology, the 3-D Hough transform has the potential to extract a fault plane by applying the method to the data of seismic source locations (longitude, latitude, and depth). However, a previous study has established some limitations of the Hough transform (Ouillon et al., 2008). First, the method cannot determine the spatial extent of the straight line or plane because those represented by the combination of parameters have an infinite length or size. Second, the Hough transform cannot deal with the spatial spread of a straight line or plane (e.g., fault thickness) because the equations that express them do not consider the uncertainty of the source location. Given our situation, we consider the plate boundary as the fault plane by assuming that tremors occur on the plate interface because previous studies have reported that LFEs and tremors occur near the plate boundary (e.g., Ghosh et al., 2012; Shelly et al., 2006). Tremor migration (temporal evolution of tremor locations on the plane) is represented by a straight line in a (2+1)-D space-time (2-D in the plane and 1-D in time) by assuming a constant migration speed in a duration. However, the conventional Hough transform cannot extract a straight line because additional information on the direction vector within the plane is necessary. Therefore, we must introduce a new Hough transform to extract a straight line in the (2+1)-D space-time, considering the uncertainties of the tremor locations.

A previous study in astronomy extracted a straight line in the (2+1)-D space-time using the Hough transform to investigate the movements of celestial bodies in observed images (Morii, 2019). Motivated by a previous study, we newly developed a space-time Hough transform to extract tremor migrations as straight lines in the (2+1)-D space-time. A new point of our method is that we can consider the uncertainties of tremor locations in the extraction of tremor migration by giving spatial spread to the straight line (by considering a cylinder). We consider (x, y, t) as a coordinate of a tremor event, where x is the longitude (the east is positive), y is the latitude (the north is positive), and t is the detection time. An arbitrary position of the straight line in the (2+1)-D space-time is represented using tyt-Euler angle (Figure 2). The tyt-Euler angle shows rotations of the coordinate system by θ, ϕ, and ψ, where θ is the zenith angle, ϕ is the azimuth, and ψ is the rotation angle. The details of the Euler angle are provided in the Supporting Information (Text S1). The equation of the straight line in (2+1)-D space-time is represented as follows:

$$\begin{pmatrix} x \\ y \\ t \end{pmatrix} = (\rho + r\cos\lambda)\,\vec{\alpha} + (r\sin\lambda)\,\vec{\beta} + m\,\vec{\gamma}\,, \tag{1}$$

where

$$\vec{\alpha} = \begin{pmatrix} -\sin\phi\sin\psi + \cos\theta\cos\phi\cos\psi \\ \cos\phi\sin\psi + \cos\theta\sin\phi\cos\psi \\ -\sin\theta\cos\psi \end{pmatrix}$$

$$\vec{\beta} = \begin{pmatrix} -\sin\phi\cos\psi - \cos\theta\cos\phi\sin\psi \\ \cos\phi\cos\psi - \cos\theta\sin\phi\sin\psi \\ \sin\theta\sin\psi \end{pmatrix} \tag{2}$$

$$\vec{\gamma} = \begin{pmatrix} \sin\theta\cos\phi \\ \sin\theta\sin\phi \\ \cos\theta \end{pmatrix},$$

ρ is the distance from the origin to the straight line (cylindrical axis), λ is the parameter that expresses the angle around the cylindrical axis measured counterclockwise from the vector $\vec{\alpha}$, and m is the parameter that determines the position on the straight line. r is the radius of the cylinder, with values ranging from zero to r_{max}, where r_{max} corresponds to the location uncertainty. $\vec{\gamma}$ is the unit direction vector of the straight line, $\vec{\alpha}$ is the unit vector in the same direction as the foot of the perpendicular line ($\rho\vec{\alpha}$), and $\vec{\beta}$ is the unit vector perpendicular to both $\vec{\alpha}$ and $\vec{\gamma}$. The vectors of $\vec{\alpha}$ and $\vec{\beta}$ are within the plane shown by the large blue circle in Figure 2a. Thus, any position of the cylinder in (2+1)-D space-time can be represented by four parameters (ρ, θ, ϕ, ψ). In particular, we can represent the migration speed as $\tan\theta$ and the migration direction as ϕ. When a tremor event is included inside the cylinder, the parameter m is eliminated from Equation 1:

$$\begin{cases} X = \rho\sin\psi + r\sin(\lambda+\psi) = -x\sin\phi + y\cos\phi \\ Y = \rho\cos\psi + r\cos(\lambda+\psi) = x\cos\theta\cos\phi + y\cos\theta\sin\phi - t\sin\theta \end{cases} . \quad (3)$$

The parameter λ is eliminated using Equation 3:

$$(X - \rho\sin\psi)^2 + (Y - \rho\cos\psi)^2 \leq r_{max}^2 . \quad (4)$$

In the space-time Hough transform, we prepare bins of parameters (ρ, θ, ϕ, ψ) that correspond to straight lines. We perform a "vote" to the corresponding "bin" when a tremor event satisfies Equation 4. The bin with the maximum number of votes represents the straight line that best explains the event data. When there are multiple straight lines that show large number of votes in the same time window, these lines can be extracted separately by the Hough transform because votes for different lines are cast on different "bins". This advantage enables us to relax the constraint of one migration in one time window imposed in previous studies. The square root of the left-hand side of Equation 4 expresses the space-time distance (D_{st}) between the tremor event and the cylindrical axis:

$$D_{st} = \sqrt{\delta x^2 + \delta y^2 + C^2 \delta t^2}\,, \tag{5}$$

where δx and δy are spatial errors with respect to the cylindrical axis, δt is the temporal error, and C is the parameter that connects space and time with a unit of speed. When we set the radius of the cylinder (r_{max}) based on the uncertainty of the tremor location, the space-time Hough transform can extract tremor migrations by considering the tremor uncertainties. In this case, parameter C should be set such that r_{max}/C is equal to the temporal resolution of the tremor catalog. If C is set smaller than the above value, the time series of tremor events projected onto the straight line may change from the original values because the temporal error is allowed up to r_{max}/C (the temporal error may exceed the temporal resolution of the catalog).

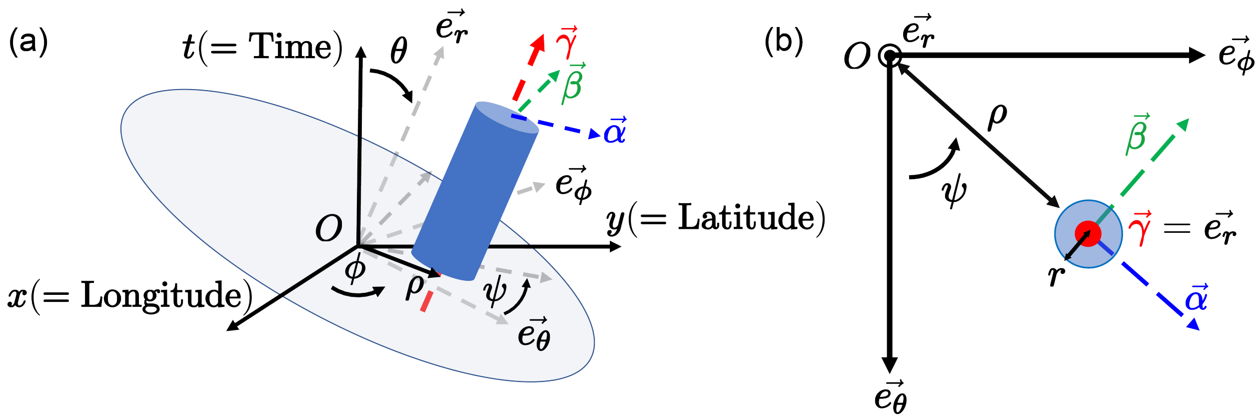

Figure 2. (**a**) Schematic diagram of the space-time Hough transform. x is the longitude (the east is positive), y is the latitude (the north is positive), and t is the detection time. ρ is the distance from the origin to the straight line (cylindrical axis), θ is the zenith angle, ϕ is the azimuth, and ψ is the rotation angle. The large blue circle shows a plane perpendicular to the unit direction vector of the straight line ($\vec{\gamma}$). (**b**) Schematic diagram of the coordinate around the vector $\vec{\gamma}$. The vectors of $\overrightarrow{e_\theta}$, $\overrightarrow{e_\phi}$, and $\overrightarrow{e_r}$ are standard unit vectors, which are consistent with those in the polar coordinate system. r is the radius of the cylinder.

2.3 Data processing

Before applying the space-time Hough transform to the tremor catalog data, we set the values of parameters r_{max} and C. In the present study, r_{max} was set to 2.5 km based on the mean uncertainty of the horizontal location in the tremor catalog (Sagae et al., 2021). C was set to 150 km/hr (= 2.5 km/min) because the temporal resolution of the catalog was 1 min. The tremor locations (longitude, latitude) were converted to a plane rectangular coordinate system (x, y) in kilometers, with the origin set at the center of the seismic array (136.31°E, 34.45°N) by using the code of EPSG:6674. We prepared bins of parameters (ρ, θ, ϕ, ψ) to extract tremor migrations using the space-time Hough transform. ρ was set in a range of 0–120 km with an interval of 0.25 km, ϕ and ψ were set in a range of 0–350° with an interval of 10 °, and θ ($\tan\theta$) was set in a range of 2–60 km/hr with an interval of 1 km/hr in addition to (0.125, 0.25, 0.5, 0.75, 1.0, 1.25, and 1.5) km/hr.

We prepared time windows with lengths (T_w) of 1, 2, 3, 4, 6, 8, 12, and 24 h to extract tremor migrations for various durations. In each time window, we applied a clustering process to a time series to determine the temporal extent of tremor migrations. Our clustering process for time series is different from that of Bletery et al. (2017), who identified a cluster of tremor events with a length of time window by clustering. Firstly, we define a first tremor event in the time window and make a "cluster". The detection time for the first tremor event is t_1. Secondly, we define the i-th tremor event that occurred after the first tremor event as the i-th target event with a detection time of t_i. We calculate the time interval $t_i - t_{i-1}$ between the target event and the previous event that occurred immediately before. Finally, if the time interval is shorter than $5\times T_w$ minutes, the target event is classified into a "cluster" to which the previous event belongs. For example, when $t_2 - t_1$ is shorter than $5\times T_w$, the second target event is classified into the cluster to which the first tremor event belongs. If the time interval is longer than $5\times T_w$ minutes, the target event is classified into a new "cluster". We determined the time interval ($5\times T_w$) for the clustering by trial and error, while visually checking tremor migrations extracted in the time window of $T_w = 1$ h. The time interval is considered to be related to the detection capability of the tremor catalog. As the tremor distribution becomes spatiotemporally sparse in the low-quality catalog, tremor migrations are not visible on a short timescale. In this case, the time interval should be increased.

After clustering, we applied the space-time Hough transform to the clusters of tremor events in the time window of each length (T_w) as follows:

(A) We select a time window that contains ten or more tremor events while moving the window from the beginning of the catalog without overlapping.

(B) We perform a "vote" to a corresponding "bin" when a tremor event within a cluster estimated by clustering satisfies Equation 4. We extract a tremor migration whose "bin" (ρ, θ, ϕ, ψ) shows the maximum number of votes. In the present study, the number of votes must be eight or more. When multiple "bins" show the same maximum number of votes, we extract the tremor migration that minimizes the mean values of space-time distances (D_{st}, Equation 5) averaged over voted tremor events.

(C) Tremor events belonging to the tremor migration are removed from the cluster. If the cluster still contains ten or more tremor events, we return to (B) and further extract tremor migrations in the cluster. When the maximum "bin" contains eight or more votes, we perform a "re-vote", which is a "vote" including the removed tremor events. This is because there may be tremor events belonging to multiple tremor migrations among the removed ones. If there are less than ten tremor events in the cluster or the maximum number of votes is less than eight, we deal with other clusters in the time window. When the searches of all clusters in the time window are completed, we return to (A) and select the other time windows that satisfy the condition of (A).

A detailed flowchart of the above process is shown in Figure 3. We define the duration of the tremor migration as $t_{max} - t_{min}$, where t_{min} is the detection time of the first tremor event included in the tremor migration and t_{max} is the detection time of the last tremor event. After tremor migrations are extracted in all time windows, overlapping ones with the same parameters (e.g., date and time, duration, ρ, and ϕ) extracted in multiple time windows are removed.

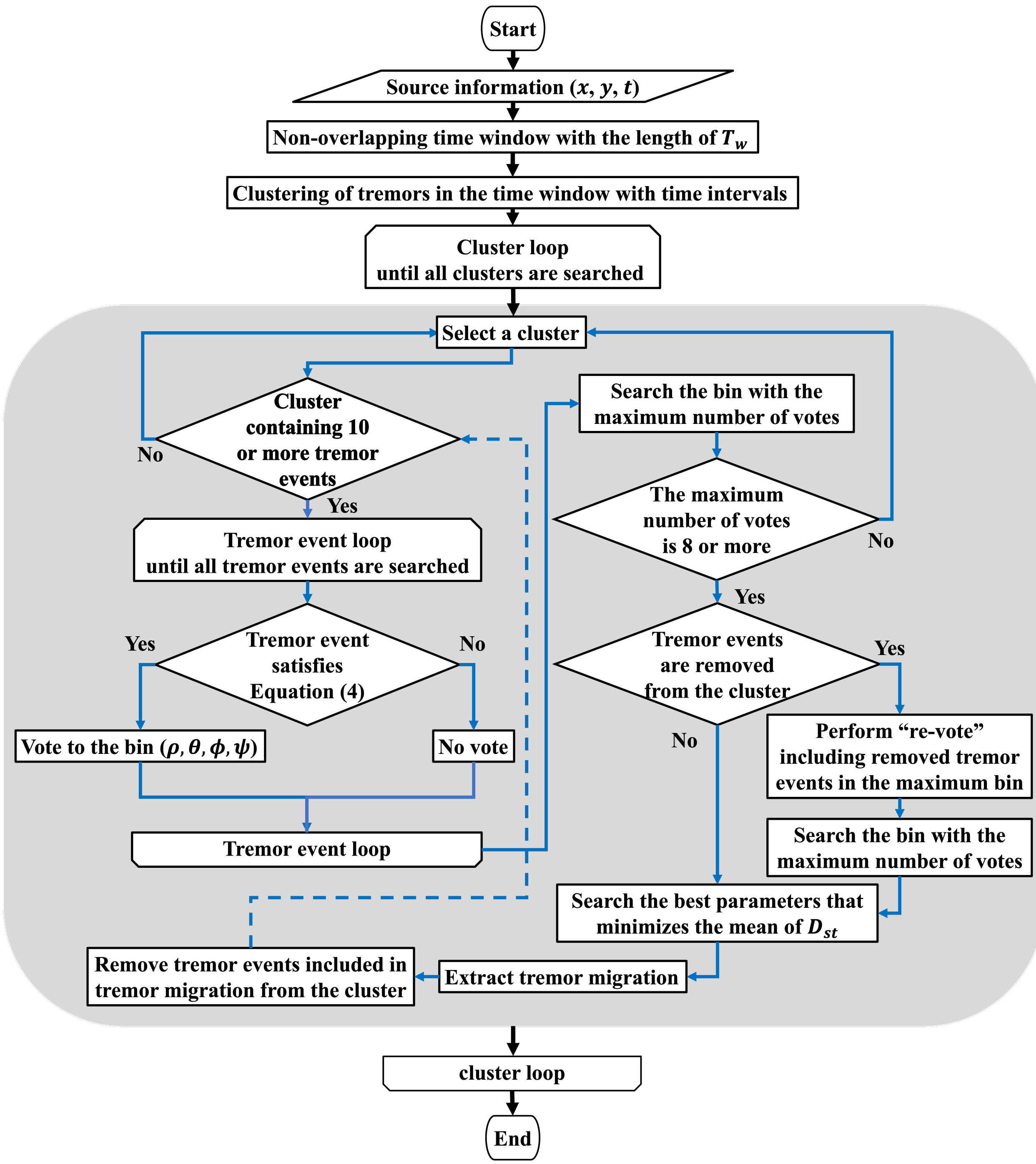

Figure 3. Flowchart of the space-time Hough transform.

Figure 4 shows an example of votes for a tremor migration with a duration of 22 min. Each panel shows the number of votes for the two parameters by fixing the remaining two parameters to the best values. In this tremor migration, the maximum number of votes is 20, as shown by the white stars in Figure 4. From the maximum values, the space-time Hough transform objectively determines candidates of the best parameters for tremor migrations by the technique of “vote”. When there are multiple candidates with the same maximum number of votes, we use the space-time distance (D_{st}, Equation 5) to identify the best parameters. Figure 5 shows the distribution of the space-time distance (D_{st}) for the candidate parameters in Figure 4. The red dots are the mean values of D_{st} for the candidates, and the black cross is the minimum value. The minimum value of the mean D_{st} enables determination of the best parameters among the candidates (ρ, θ, ϕ, ψ) with the maximum number of votes. Figure 6 shows an example of tremor migrations extracted in a time window with a length of 2 h. We succeeded in extracting three different tremor migrations with the durations of 22 min, 36 min, and 53 min during the 2 h. The tremor migration with the duration of 22 min (red line) is the example shown in Figures 4 and 5. Our method can objectively extract the complex patterns of tremor migrations in a zigzag style. This result means that the space-time Hough transform newly developed in the present study enables us to extract multiple tremor migrations with various durations regardless of the length of the time window.

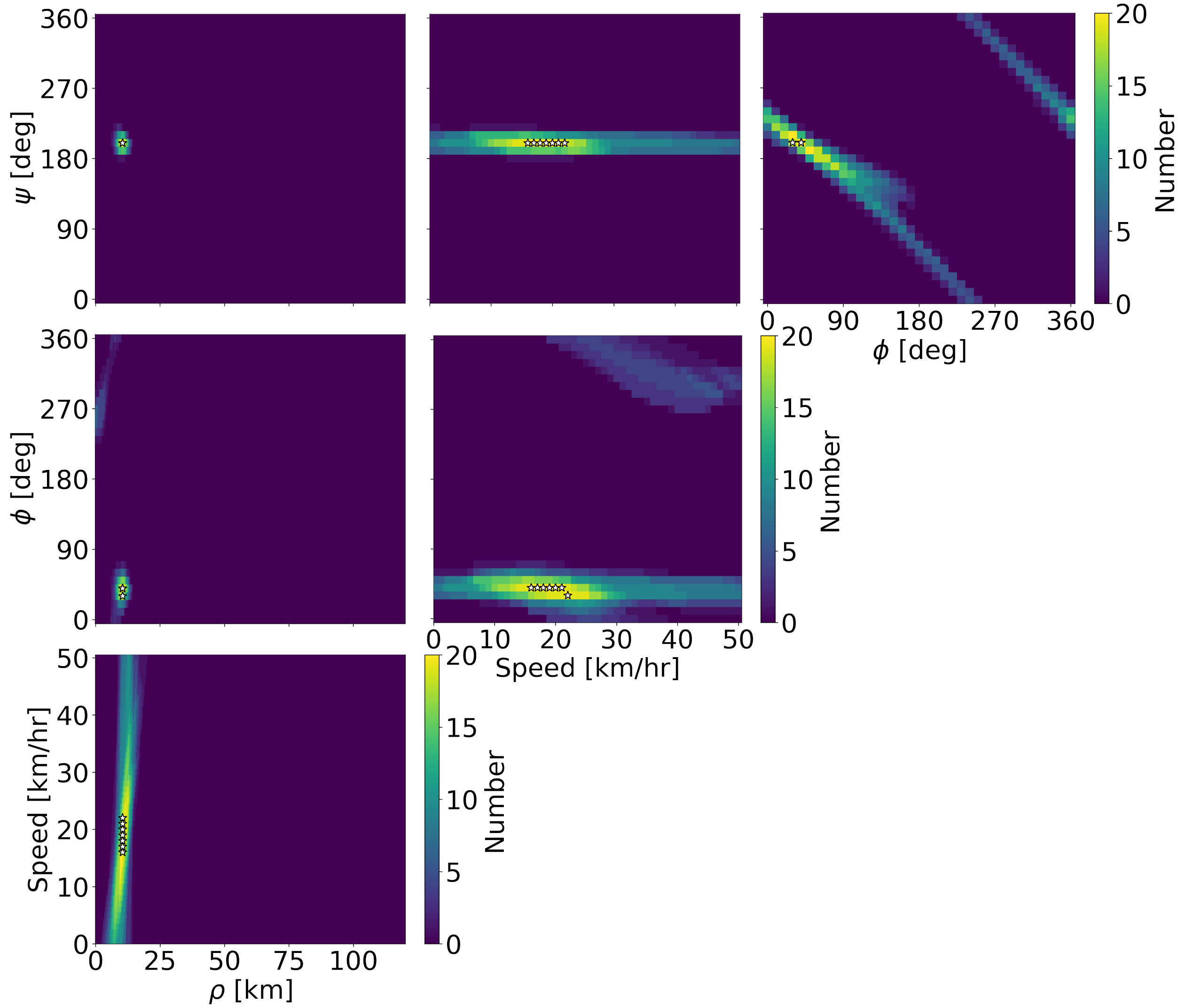

Figure 4. The number of votes for tremor migration with the duration of 22 min. Color bar shows the number of votes. Each panel shows the number of votes for two parameters by fixing the remaining two parameters to the best ones. The maximum number of votes is 20. The white stars show candidates of the best parameters with the same maximum votes. The best parameters of the tremor migration are $\rho = 10.5$ km, migration speed ($= \tan\theta$) $= 17$ km/hr, $\phi = 40°$, and $\psi = 200°$ as shown in Figure 5.

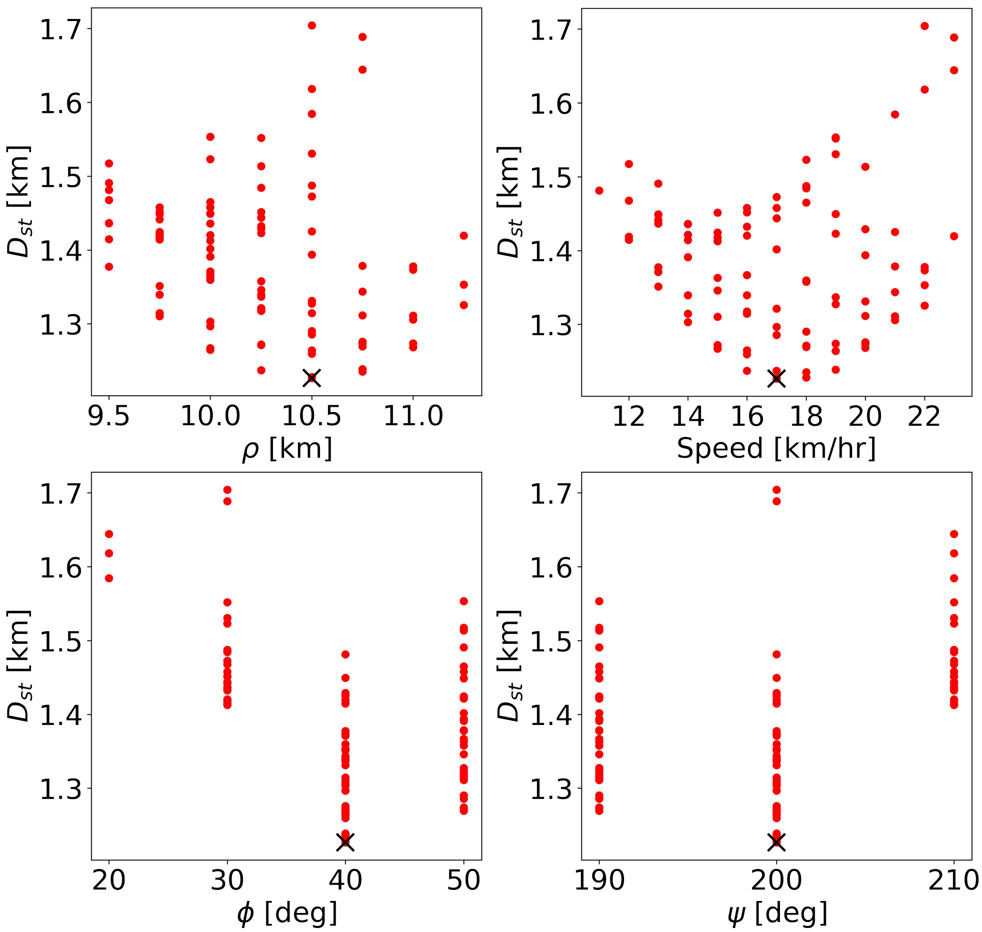

Figure 5. Distribution of space-time distance (D_{st}) for candidates of parameters with the same maximum number of votes. The candidates are combinations of parameters with the maximum votes in Figure 4. The red dots show mean D_{st} values whose maximum number of votes is 20. The black cross shows the minimum value of the mean D_{st}.

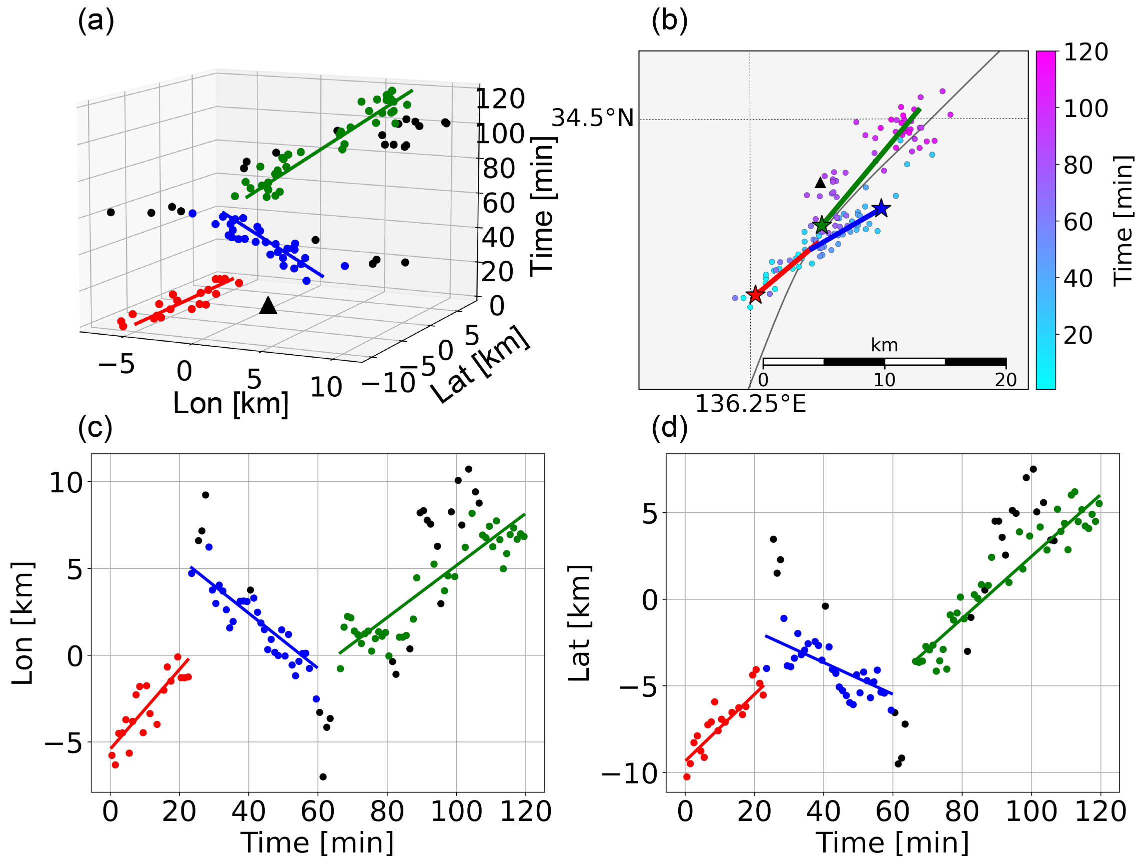

Figure 6. An example of tremor migrations extracted in one time window with the length of 2 h. (**a**) Tremor migrations in the (2+1)-D space-time. The red, blue, and green lines show tremor migrations with durations of 22 min, 36 min, and 53 min, respectively. The red, blue, and green dots show tremor events composing each tremor migration. The black dots are tremor events that do not belong to tremor migrations. The black triangle shows the origin set at the location of the array (136.31°E, 34.45°N). (**b**) Map view of tremor migrations. Each line shows tremor migrations and the colored stars are starting points of the three tremor migrations. The dots and their colors represent tremor locations and their timings. (**c**) Space-time plot of tremors between the longitude and the time. (**d**) Space-time plot of tremors between the latitude and the time.

3 Results

3.1 Tremor migrations extracted during a tremor episode

During the two years from July 2012 to July 2014, we succeeded in extracting 1,010 tremor migrations with durations ranging from 10 min to 24 h (Figure 7). Tremor migrations were categorized into four patterns based on their migration directions. We defined the along-strike direction as 45° clockwise from the north and the along-dip direction as perpendicular to the strike. The tremor migrations are represented by the lines with different colors: the red lines express tremor migrations with directions of 0–90° clockwise from the north (northeast direction); the blue lines represent those with directions of 180–270° (southwest direction); the yellow lines represent those with directions of 90–180° (up-dip direction), and the green lines represent those with directions of 270–360° (down-dip direction). Tremor migrations appear to behave differently depending on area. The details are presented in Section 3.2.

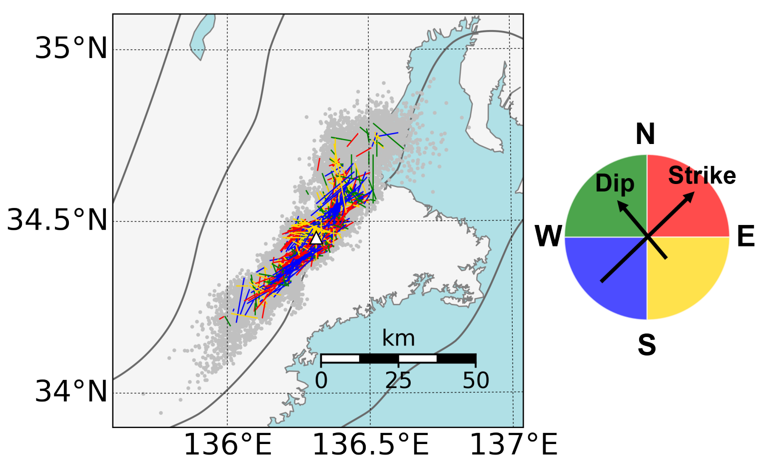

Figure 7. Distribution of tremor migrations from July 2012 to July 2014. The gray dots show tremor locations, and the white triangle shows the location of the seismic array. The lines show directions of tremor migrations, where red lines are directions of 0–90° clockwise from the north (northeast direction), blue lines are directions of 180–270° (southwest direction), yellow lines are directions of 90–180° (up-dip direction), and green lines are directions of 270–360° (down-dip direction), respectively. The color diagram is shown on the right.

Figure 8 shows examples of tremor migrations that are extracted during a tremor episode from August 11th to 16th, 2012. In this tremor episode, Sagae et al. (2021) found a pattern of the main front by visual inspection: tremors started from the down-dip side of the tremor zone, first propagated in the up-dip direction, and then migrated northeastward and southwestward. The present study extracted 171 tremor migrations during the same tremor episode. Figures 8a and 8b show 120 tremor migrations with durations ranging from 10 min to 1 h. We detected not only RTRs and tremor streaks reported in Sagae et al. (2021) but also many complex tremor migrations that were not easily identified by visual inspection. Figures 8c and 8d show 38 tremor migrations with durations ranging from 1 h to 6 h, and Figures 8e and 8f represent 13 tremor migrations with durations ranging from 6 h to 24 h. These 51 tremor migrations show up-dip migrations and bilateral migrations along the strike. In particular, up-dip migrations in the initial stage of the tremor episode (August 11th in Figure 8) show not only the along-dip component but also the along-strike component (northeast direction). Tremor migrations in the other episodes propagate in the similar path (Figure S8). Figure 9 zooms up the tremor episode occurring on August 13th, 2012 to see fine structures of spatiotemporal distribution of tremor migrations. By comparing tremor migrations with different durations (00:00–14:00 in Figures 9b, 9d, and 9f), we recognized multiple tremor migrations with short durations within those with long durations. We further noticed that migration speeds slowed down as durations increased. The relationship between migration speed and duration is discussed in Section 4.3. Focusing on tremor migrations with durations ranging from 6 h and 24 h, we found that multiple straight lines appear to be parallel (Figure 9f). This result shows that the tremor migrations have spatial spread beyond the uncertainties of the tremor locations. In the present study, we can judge whether or not tremor migrations spread two-dimensionally because the space-time Hough transform can extract tremor migrations considering the uncertainties of tremor locations. This is an advantage of the space-time Hough transform. Results of other tremor episodes are shown in the Supporting Information (Figures S2–S12).

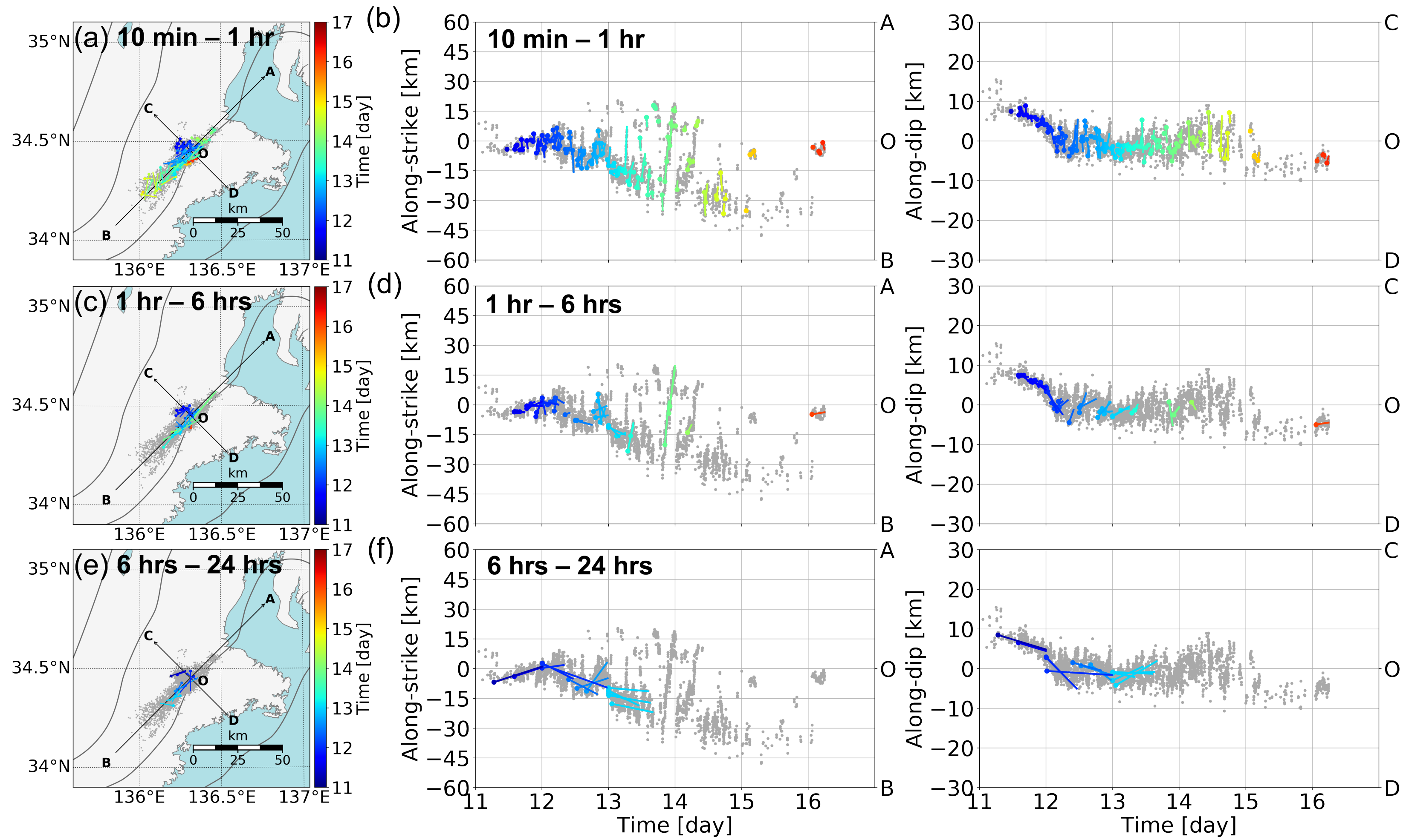

Figure 8. Tremor migrations during a tremor episode from August 11th to 16th, 2012. (**a**) Map view of the tremor migrations with durations ranging from 10 min to 1 h. The gray dots show tremor locations. Colored lines and dots show tremor migrations and their starting points, and the colors show the starting time of tremor migrations. (**b**) Spatiotemporal plots of the tremor migrations with the same durations as that of (**a**). The left panel shows spatiotemporal evolutions of tremor migrations along the strike (A–B) and the right

panel shows spatiotemporal evolutions of those along the dip (C–D). (**c**), (**d**) Same as (**a**) and (**b**), but for tremor migrations with durations ranging from 1 h to 6 h. (**e**), (**f**) Same as (**a**) and (**b**), but for tremor migrations with durations ranging from 6 h to 24 h.

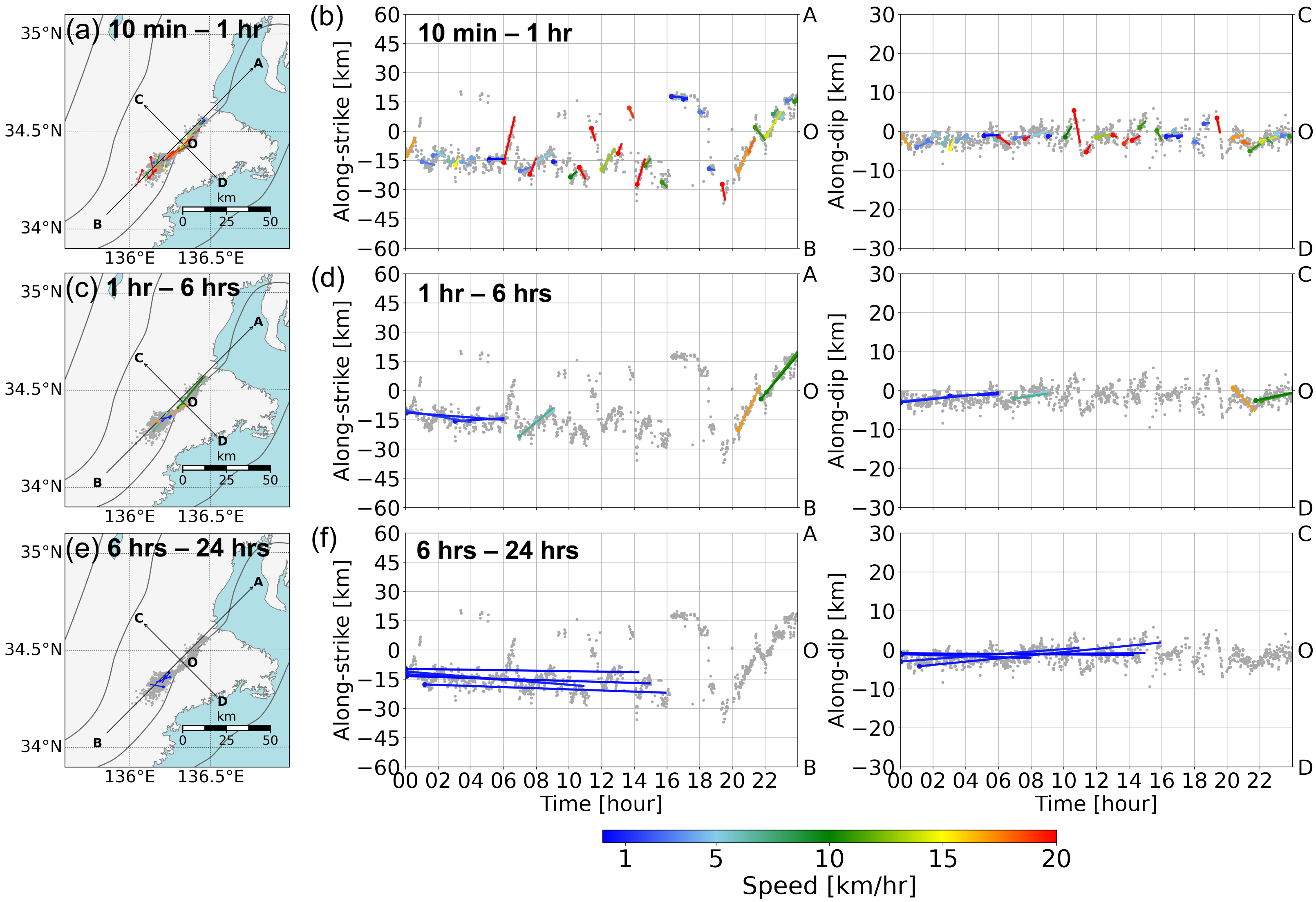

386 **Figure 9.** Same as Figure 8, but for tremor migrations zooming on August 13th, 2012. The colors show migration speeds.

3.2 Spatial distribution of tremor migrations

Figure 10a shows the frequency distribution of tremor events included in the tremor migrations. The number of tremor events was counted inside cells that are arranged at intervals of 0.025° along longitude and latitude. Comparing the spatial distribution of all tremor events (Figure 1b) and the frequency in Figure 10a, we found four areas (R1–R4) where the frequency of tremor events was relatively high beneath the Kii Peninsula. Figure 10b shows the spatial distribution of the predominant directions of tremor migrations. For each cell, we calculated predominant directions of tremor migrations as a ratio of the number of tremor migrations with directions of 0–90° and 180–270° over the total number of tremor migrations with directions of 0–360°. Our result shows that along-strike migrations (violet) are more predominant on the up-dip side of the tremor zone. This characteristic is similar to that reported by Obara et al. (2012). Moreover, we found that along-dip migrations (orange) were predominant in R1 and R3, and along-strike migrations were principal in R2 and R4 (Figure 10b). The areas R2 and R4 correspond to the areas where RTRs were reported by visual checking in Sagae et al. (2021). The characteristics of R1–R4 are discussed in more detail in Section 4.1.

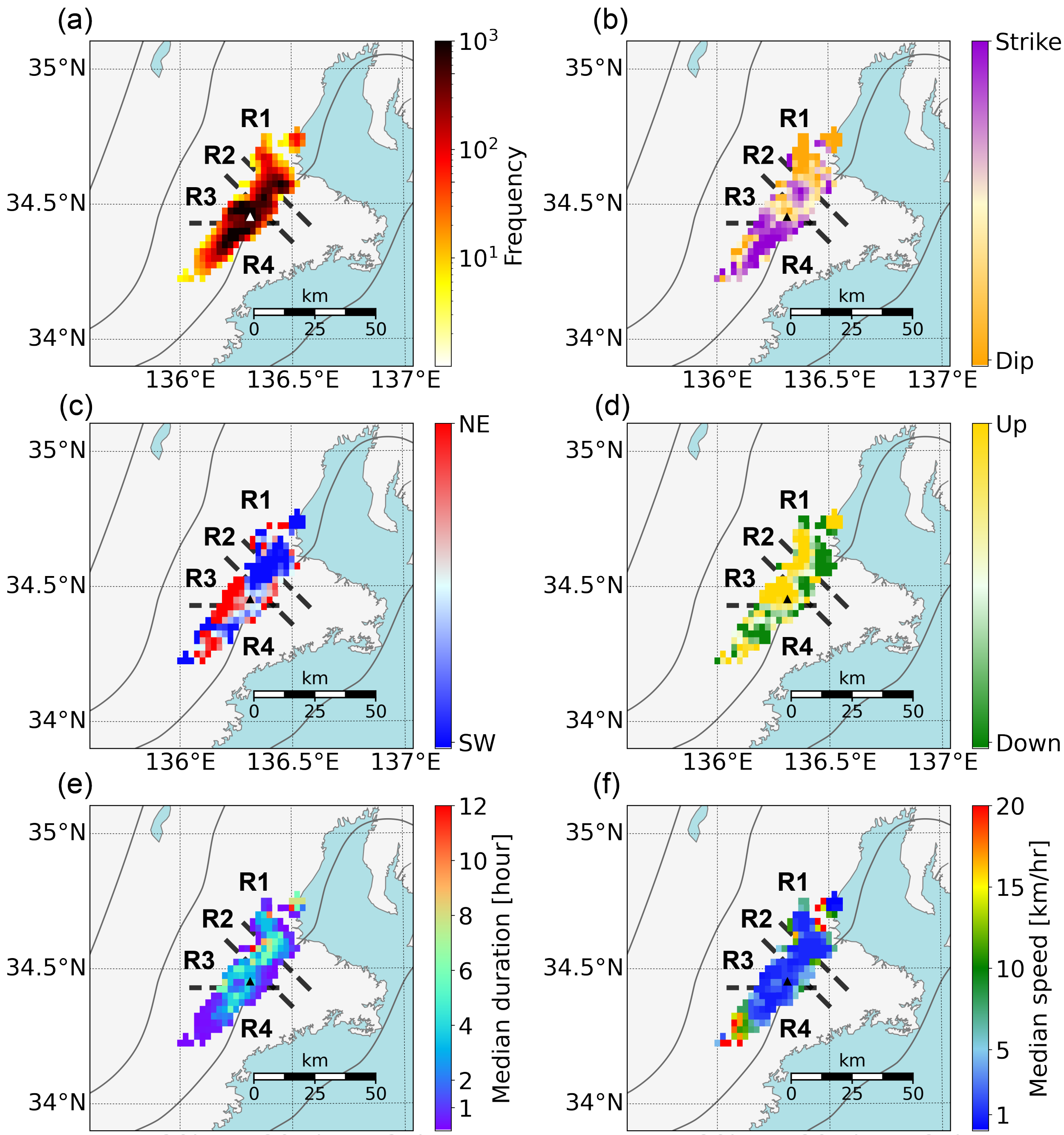

Figure 10. (**a**) Frequency distribution of tremor events included in tremor migrations. The white triangle shows the location of the array. The color bar shows the frequency of tremor events. The dashed lines are additional lines to distinguish the areas R1–R4, where the frequency of tremor events is high. (**b**) Spatial distribution of predominant directions of tremor migrations. The black triangle shows the location of the array. The violet color shows that tremor migrations along the strike are predominant (0–90° and 180–270° clockwise from the north), and the orange color

shows that tremor migrations along the dip are predominant (90–180° and 270–360°). (**c**) Spatial distribution of predominant directions of tremor migrations along the strike. The red and blue colors show the predominant directions of the northeast (0–90°) and southwest (180–270°), respectively. (**d**) Spatial distribution of predominant directions of tremor migrations along the dip. The yellow and green colors show predominant directions of the up-dip (90–180°) and down-dip (270–360°), respectively. (**e**) Spatial distribution of median duration of tremor migrations. (**f**) Spatial distribution of median speed of tremor migrations.

Figures 10c and 10d show the predominant directions of tremor migrations along the strike and dip, respectively. The predominant direction along the strike was defined as the ratio of the number of tremor migrations with directions of 0–90° over the total number of along-strike migrations with directions of 0–90° and 180–270°. The predominant direction along the dip was the ratio of the number of tremor migrations with directions of 90–180° over the total number of along-dip migrations with directions of 90–180° and 270–360°. Regarding the along-strike direction (Figure 10c), we observed significant changes in the predominant directions at the boundary between R2 and R3. Northeastward tremor migrations (red) were predominant in the southwest area, while southwestward tremor migrations (blue) were principal in the northeast area. For the along-dip direction (Figure 10d), up-dip migrations (yellow) were predominant on the down-dip side of the tremor zone and down-dip migrations (green) were principal on the up-dip side. This characteristic of along-dip migrations is a new finding of the present study.

To characterize the spatial distribution of the duration and speed of tremor migrations, we calculated the median values for each cell. The results are presented in Figures 10e and 10f. Areas where the median duration is relatively long (6 h or more) correspond well to those where the median speed is relatively slow (1 km/hr or less). The main front is characterized by a duration ranging from several hours to days and a speed of approximately 10 km/day. The values of the long median duration and slow median speed were consistent with the characteristics of the main front. Our results show the locations where the main front with long durations often occurs. When we investigated tremor migrations with high speeds (10 km/hr or more), their spatial characteristics were different from the patterns of the main front shown in Figure 10. Figure 11a shows the predominant directions of along-strike tremor migrations with speeds of 10 km/hr or more. Areas where southwestward tremor migrations are predominant in Figure 10c (blue) change their patterns to those where northeastward tremor migrations are principal (red in Figure 11a). Figure 11b shows spatial distribution of the median speed for tremor migrations with speeds of 10 km/hr or more. Tremor migrations with high speeds were found even in areas where the median duration was relatively long and the median speed was slow. These results show that high-speed tremor migrations occur inside the main front and that the inside of the main front is rich in spatiotemporal variations in tremor migrations. Thus, our results reveal fine structures of tremor migrations not only in time (Figures 8 and 9) but also in space (Figures 10 and 11).

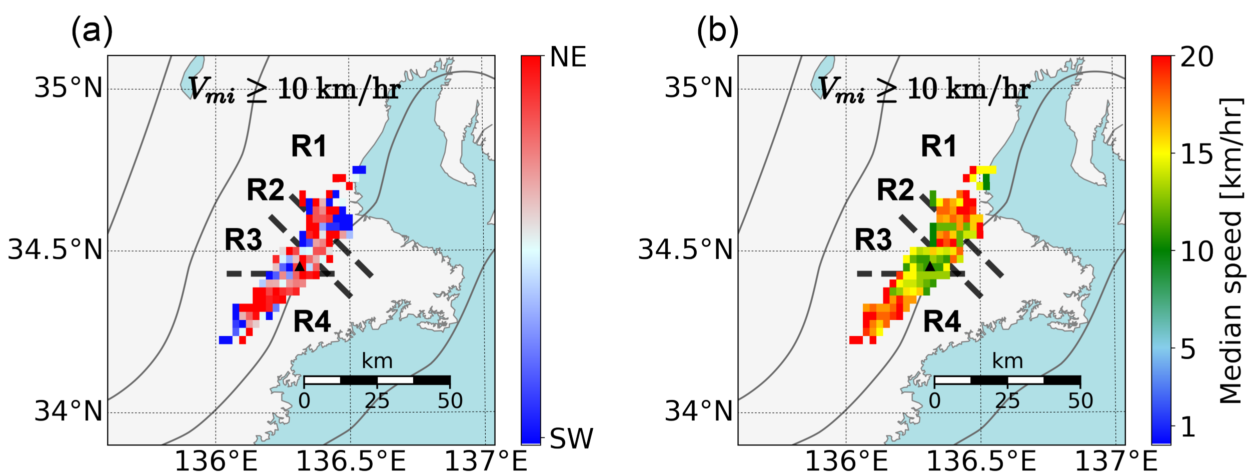

Figure 11. (**a**) Spatial distribution of predominant directions of tremor migrations with high speeds along the strike. The dashed lines and the black triangle are the same as those in Figure 10. Tremor migrations with speeds of 10 km/hr or more are used to estimate the migration patterns. Colors are the same as those in Figure 10c. (**b)** Spatial distribution of median speed of tremor migrations with speeds of 10 km/hr or more. Colors are the same as those in Figure 10f.

4 Discussions

4.1 Comparison of the spatial distribution of tremor migrations with previous studies

We describe the characteristics of the four areas (R1–R4) in further detail. In area R1, tremor migrations had a component propagating southwestward (Figure 10c), although along-dip migrations were predominant (Figure 10b). Up-dip migrations were predominant on the down-dip side of the tremor zone (Figure 10d). This result corresponds to the observations that tremors start from the down-dip side of the tremor zone and propagate in the up-dip direction (Sagae et al., 2021).

For area R2, previous studies established that tremor episodes tended to stop in R2 (e.g., Nakamoto et al., 2021; Sagae et al., 2021), and that there were tremor patches with high radiated energies in R2 (Nakamoto et al., 2021; Yabe & Ide, 2014). The present study shows that along-strike migrations are predominant (Figure 10b) and tremor migrations tend to propagate southwestward (Figure 10c). Although tremor migrations with high speeds of 10 km/hr or more were predominant in along-strike directions beneath most of the Kii Peninsula, along-dip migrations were principal in R2 (Figure S13). This result suggests that area R2 is a characteristic field (e.g., tremor patches arranged subparallel to the dip; fluid conduits along the dip) to generate tremor streaks along the dip, as observed in a previous study (Figure S14 in Sagae et al., 2021). The implications of tremor streaks are outside the scope of the present study.

In area R3, along-dip migrations were predominant (Figure 10b) and tremor migrations propagated not only in the up-dip direction but also northeastward (Figures 10c and 10d). When tremor migrations reach the upper limit of the tremor zone, they are less likely to propagate from R3 to R1 beyond R2. This characteristic is observed as changes in the predominant direction of the along-strike migration around the boundary between R2 and R3 (Figure 10c). Previous studies have also observed these characteristics (e.g., Ando et al., 2012; Sagae et al., 2021).

In area R4, tremor migrations were predominant in the along-strike direction (Figure 10b). In addition, tremor migrations on the up-dip side of the tremor zone propagated in both the northeast and the southwest directions (white color in Figure 10c). These results reflect the observations that RTRs repeatedly occur in R4 (Sagae et al., 2021). Interestingly, most of the tremor migrations propagated in the down-dip direction (Figure 10d), and up-dip migrations propagating directly from R3 to R4 rarely occurred. This characteristic is obtained from the results that the down-dip migration and the along-strike migration propagating northeastward are principal around the boundary between R3 and R4 (Figures 10c and 10d).

Previous studies have investigated the characteristics of tremor migrations beneath the Kii Peninsula (Obara et al., 2012; Wang et al., 2018). Wang et al. (2018) classified tremor locations beneath the Kii Peninsula into 17 segments using a 2-D Hidden Markov model and examined tremor activities among the segments. They calculated transition probabilities which explained the migration patterns among the segments. Furthermore, areas with high transition probabilities of tremor activities among the segments were classified into four subsystems along the strike (K1–K4, Figure 6 in Wang et al., 2018). Subsystems K3 and K4 in their results included the four areas with the high frequency of tremor events (R1–R4) in our results. Some characteristics of tremor migrations in R1–R4 are recognized in tremor activities among the segments reported by Wang et al. (2018). For example, up-dip migrations propagating northeastward were found in R3 (propagation from segment 10 to 11, Figure 6 in Wang et al., 2018). There were almost no up-dip migrations propagating directly from R3 to R4 (propagation from segment 10 to 9, Figure 6 in Wang et al., 2018). Our results provide new insights. For example, up-dip migrations were predominant on the deep part of the tremor zone and down-dip migrations were principal on the shallow part (Figure 10d). In R1, up-dip migrations were predominant on the deep part of the tremor zone and tremor migrations tended to propagate southwestward (to R2). These differences in the characteristics of tremor migrations were attributed to the fact that Wang et al. (2018) could not investigate tremor migrations inside each segment.

4.2 Relationship between tremor migrations and heterogeneous distribution of fault strength on the plate interface

Previous studies have suggested that the spatial distribution of tremor energies reflects the heterogeneity in fault strength on the plate boundary (e.g., Kano et al., 2018a; Yabe & Ide, 2014). They also suggested that tremor patches with high radiated energies are related to the growth of along-strike migrations (Nakamoto et al., 2021; Yabe & Ide, 2014). Before the tremor patch with high energy was ruptured, tremors migrated from the tremor patch with low energy on the deep part of the tremor zone to that with high energy on the shallow part. When the tremor patch with high energy was broken, tremors migrated along the strike after the occurrence of burst activity (e.g., Shelly, 2010). The behavior of the tremor migrations was influenced by whether or not the tremor patch with high energy was broken. In the Kii Peninsula, the location of the high-energy tremor patch (Nakamoto et al., 2021; Yabe & Ide, 2014) corresponds to R2 in the present study. Up-dip migrations propagating into R2 were observed in R1 and R3 (Figures

10c and 10d). Moreover, in R2, along-strike migrations were predominant (Figure 10b) and tremor episodes tended to stop (Sagae et al., 2021). Our results suggest that the existence of a tremor patch with high energy controls the pattern of tremor migration before and after the tremor patch is broken.

RTRs have been observed to occur repeatedly in the same areas beneath the Kii Peninsula (Sagae et al., 2021). To discuss the relationship between the spatial distribution of RTRs and that of tremor patches, we systematically detected RTRs as follows: First, we searched for cells that contained starting points of tremor migrations with speeds of 10 km/hr or more. We then detected RTRs when the migration directions were opposite to the predominant direction inside the cells obtained in Figure 10c (the predominant direction of along-strike migration). Figures 12a and 12b show the spatial distribution of the RTRs during a tremor episode from August 11th to 16th, 2012, and a tremor episode from July 3rd to 14th, 2014, respectively. The white arrow shows the pattern of the main front, and the spatiotemporal evolutions of tremor migrations during those tremor episodes are shown in Figure 8 and Figure S12. The background colors show the median energy rates of the tremors (Yabe & Ide, 2014). The median energy rates were calculated in cells arranged at an interval of 0.05° along longitude and latitude, when the cells contained 100 or more tremor events that were located within 10 km.

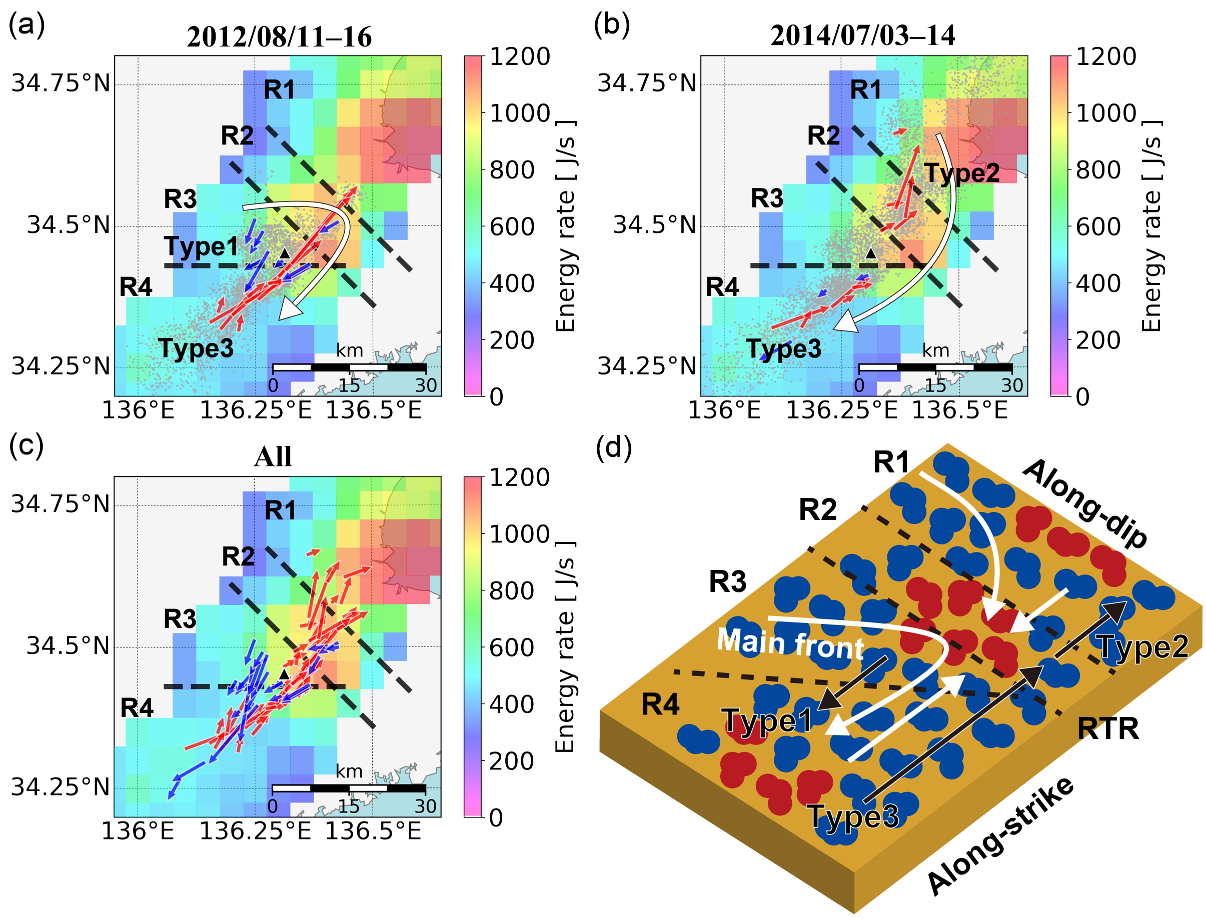

Figure 12. (**a**) Spatial distribution of RTRs during a tremor episode from August 11th to 16th, 2012. The red arrows show RTRs propagating northeastward, and the blue arrows show those propagating southwestward. The white arrow shows the pattern of the main front and the gray dots show tremor locations. The dashed lines and the black triangle are the same as those in Figure 10. The background colors show median energy rates (Yabe & Ide, 2014). (**b**) Same as (**a**), but for RTRs during a tremor episode from July 3rd to 14th, 2014. (**c**) Same as (**a**), but for all RTRs detected in the present study. (**d**) Schematic diagram of the distribution of tremor patches and tremor migrations beneath the Kii Peninsula. The red and blue dots show strong tremor patches with high energies and weak ones with low energies, respectively. The white arrows show the patterns of the main front. The black arrows (Type1–Type3) show the patterns of RTRs.

In Figures 12a and 12b, the three types of RTRs are presented. The first is the southwestward RTR that occurs near the southwest side of R2 (blue arrows shown by Type1 in

Figure 12a) when the main front propagates from the southwest side of R2 to the northeast. The second is the northeastward RTR that occurs near the northeast side of R2 (red arrows shown by Type2 in Figure 12b) when the main front propagates from the northeast side of R2 to the southwest. The third is the northeastward RTR that occurs near the southwest side of R4 (red arrows shown by Type3 in Figures 12a and 12b) when the main front propagates southwestward in R4. The third sometimes propagated from R4 to R2 (red arrows in Figure 12a). The three types of RTRs were found during other tremor episodes (Figure S14). Figure 12c shows all the RTRs detected in the present study. The spatial distribution of the RTRs appears to be a superposition of the three types of RTRs for the most part. Thus, our results suggest the existence of areas in which RTRs occur repeatedly. In addition, the median energy rates appear to be relatively high near areas where the three types of RTRs are found (R2 and the southwest side of R4). The occurrence of the three types of RTRs seems to depend on the directions from which the main front reaches the tremor patches. We show a schematic diagram of the spatial distribution of tremor migrations (Figure 12d) by summarizing the characteristics of areas R1–R4 discussed in Section 4.1 and those of RTRs in this section. Ando et al. (2012) explained the pattern of RTR based on a stress diffusion model. They interpreted RTR as a phenomenon in which weak patches with low energies that were reloaded or healed behind a front of stress diffusion were broken again when the front reached strong patches with high energies and the strong patches were ruptured. This interpretation of the RTR explains the distribution of tremor patches and the patterns of the RTRs in the present study (Figure 12). Thus, we consider that the patterns of the RTRs are controlled by the distribution of tremor patches with various frictional properties. Our results imply that the fine structures of tremor migrations and the distribution of tremor energies are key to investigating the frictional properties of the plate interface.

4.3 Relation between migration speed and duration

Diffusive tremor migrations, which are tremor migrations with their speeds decreasing with increasing durations (Obara et al. 2012), were often observed in the front of tremor activities during tremor episodes (e.g., Ando et al., 2012; Ide, 2010). We examined the relationship between migration speeds and durations based on our data set. Figure 13a shows histograms of the migration speeds versus duration. For the durations ranging from 10 min to 1 h (red), 1 h to 3 h (blue), 3 h to 6 h (green), and 6 h to 24 h (yellow), the most frequent values of migration speeds are 3 km/hr, 1.5 km/hr, 0.75 km/hr, and 0.5 km/hr, respectively. As Obara et al. (2012) reported, we also found that tremor migrations slowed down as the durations increased. We quantitatively investigated the relationship between migration speed and duration. Figure 13b shows the relationship between the migration speed (V_{mi}) and the duration (T). We found that the relation $V_{mi} \propto T^{-0.5}$ holds for tremor migrations. When we consider a diffusion process, the relation $V_{mi} = \frac{L}{T} = \sqrt{\frac{D}{T}}$ is derived based on the relation $L^2 = DT$, where L is the propagation distance, and D is the diffusion coefficient. Thus, our results quantitatively suggest that the growth of the tremor migrations is controlled by the diffusion process. Stress diffusion and pore-pressure diffusion are candidates for explaining the diffusion process (e.g., Ando et al., 2012; Cruz-Atienza et al., 2018; Farge et al., 2021). Understanding the physical mechanisms behind slow earthquakes will be the focus of our future work.

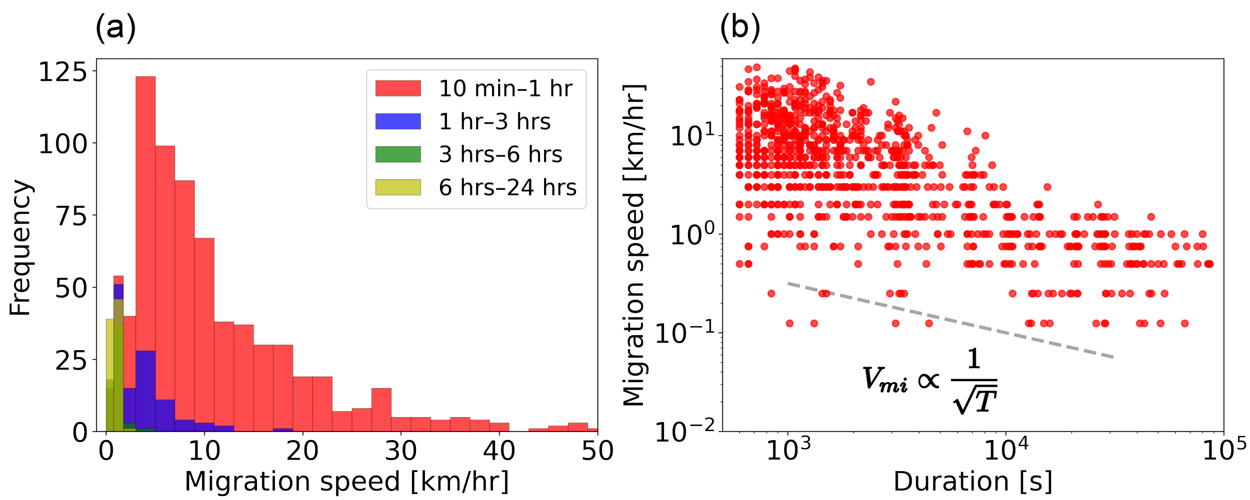

Figure 13. (**a**) The histograms of migration speeds in their respective durations. Red, blue, green, and yellow are the histogram of migration speeds for tremor migrations with durations ranging from 10 min to 1 h, 1 h to 3 h, 3 h to 6 h, and 6 h to 24 h, respectively. (**b**) The relationship between migration speed (V_{mi}) and duration (T). The gray dashed line shows the relation $V_{mi} \propto T^{-0.5}$.

5 Conclusions

The present study newly developed the space-time Hough transform to objectively extract tremor migrations. The advantage of this method is that multiple tremor migrations can be extracted regardless of the lengths of time windows and projected axes because a technique of "vote" enables us to distinguish the four parameters representing the tremor migration. The space-time Hough transform was applied to the data of tectonic tremors beneath the Kii Peninsula, Southwest Japan. Consequently, we succeeded in extracting 1,010 tremor migrations with durations ranging from 10 min to 24 h between July 2012 and July 2014.

Investigating the spatial distribution of tremor migrations, we found four areas (R1–R4) with the large number of tremor events composing tremor migrations. The followings are the characteristics of the tremor migrations in these areas: In areas R1 and R3, tremor migrations were predominant in the along-dip direction. In areas R2 and R4, tremor migrations were predominant in the along-strike direction. These patterns of tremor migrations represent the behavior of the main front because their spatial distribution of the median duration (6 h) and the median speed (1 km/hr) are consistent with the main front characteristics. We systematically detected RTRs based on the spatial characteristics of the main front, and the three types of RTRs with different patterns were found near R2 and R4. The patterns of tremor migrations (main front and RTR) are related to the distribution of tremor energies, suggesting that the distribution of tremor migrations reflects the fault strength on the plate interface. In addition, we investigated the relationship between migration speed and duration. Tremor migrations slowed down as the durations increased, and the relation $V_{mi} \propto T^{-0.5}$ held. This relationship suggests that a diffusion process controls the growth of tremor migrations.

The space-time Hough transform can objectively extract tremor migrations from any data in the tremor catalog worldwide if we set the parameters based on their tremor uncertainties and temporal resolution. The tremor migrations extracted using our method include information on their locations, timing, durations, migration directions, and migration speeds. Therefore, if we comprehensively extract tremor migrations by using the space-time Hough transform, their spatiotemporal characteristics will help understand the rupture process of slow earthquakes worldwide.

Acknowledgements

We thank Dr. Suguru Yabe for providing us with a catalog of tectonic tremors, including information on their energy rates (Yabe & Ide, 2014). We would like to thank Editage (www.editage.com) for English language editing.

Conflict of Interest

The authors declare that they have no known financial or non-financial completing interests.

Data Availability Statement

The catalog of tremor migrations in the present study is available from Data Set S1 in the Supporting Information. The tremor catalog of Yabe & Ide (2014) can be downloaded from 'Slow Earthquake Database' (Kano et al. 2018b; http://www-solid.eps.s.u-tokyo.ac.jp/~sloweq/), which is supported by the Japan Society for the Promotion of Science (JSPS) KAKENHI Grant Number JP16H06472 and JP21H05200.

References

Ando, R., Takeda, N., & Yamashita, T. (2012), Propagation dynamics of seismic and aseismic slip governed by fault heterogeneity and Newtonian rheology, *J. Geophys. Res.*, 117, B11308, doi:10.1029/2012JB009532.

Bletery, Q., A. M. Thomas, J. C. Hawthorne, R. M. Skarbek, A. W. Rempel, & R. D. Krogstad (2017), Characteristics of secondary slip fronts associated with slow earthquakes in Cascadia, *Earth and Planetary Science Letters, 463,* 212–220, https://doi.org/10.1016/j.epsl.2017.01.046.

Cruz-Atienza, V.M., Villafuerte, C., & Bhat, H.S. (2018), Rapid tremor migration and pore-pressure waves in subduction zones. *Nat Commun* **9,** 2900, https://doi.org/10.1038/s41467-018-05150-3

Farge, G., Jaupart, C., & Shapiro, N. M. (2021). Episodicity and migration of low frequency earthquakes modeled with fast fluid pressure transients in the permeable subduction interface. *Journal of Geophysical Research: Solid Earth*, 126, e2021JB021894. https://doi.org/10.1029/2021JB021894

Ghosh, A., Vidale, J. E., Sweet, J. R., Creager, K. C., Wech, A. G., Houston, H., & Brodsky, E. E. (2010), Rapid, continuous streaking of tremor in Cascadia, *Geochem. Geophys. Geosyst.*, 11, Q12010, doi:10.1029/2010GC003305.

Ghosh, A., Vidale, J. E., & Creager, K. C. (2012), Tremor asperities in the transition zone control evolution of slow earthquakes, *J. Geophys. Res.*, 117, B10301, doi:10.1029/2012JB009249.

Hirose, F., Nakajima, J., & Hasegawa, A. (2008), Three-dimensional seismic velocity structure and configuration of the Philippine Sea slab in southwestern Japan estimated by double-difference tomography, *J. Geophys. Res.*, 113, B09315, doi:10.1029/2007JB005274.

Hirose, H., & Obara, K. (2010), Recurrence behavior of short-term slow slip and correlated nonvolcanic tremor episodes in western Shikoku, southwest Japan, *J. Geophys. Res.*, 115, B00A21, doi:10.1029/2008JB006050.

Hough, P. V. C. (1962), Method and means for recognizing complex patterns, *U.S. Patent, no.3069654.*

Houston, H., Delbridge, B., Wech, A., & Creager, K. (2011), Rapid tremor reversals in Cascadia generated by a weakened plate interface. *Nature Geosci* **4**, 404–409, https://doi.org/10.1038/ngeo1157

Ide, S. (2010), Striations, duration, migration and tidal response in deep tremor. *Nature* **466,** 356–359, https://doi.org/10.1038/nature09251

Imanishi, K., Takeda, N., Kuwahara, Y., & Koizumi, N. (2011), Enhanced detection capability of non-volcanic tremor using a 3-level vertical seismic array network, VA-net, in southwest Japan, *Geophys. Res. Lett.*, 38, L20305, doi:10.1029/2011GL049071.

Ito, Y., Hino, R., Kido, M., Fujimoto, H., Osada, Y., Inazu, D., Ohta Y., Iinuma, T., Ohzono, M., Miura, S., Mishina, M., Suzuki, K., Tsuji, T., & Ashi, J. (2013). Episodic slow slip events in the Japan subduction zone before the 2011 Tohoku-Oki earthquake. *Tectonophysics*, **600**(Suppl C), 14–26. https://doi.org/10.1016/j.tecto.2012.08.022

Kano, M., Kato, A., Ando, R., & Obara, K. (2018a), Strength of tremor patches along deep transition zone of a megathrust. *Sci Rep* **8,** 3655, https://doi.org/10.1038/s41598-018-22048-8

Kano, M., N. Aso, T. Matsuzawa, S. Ide, S. Annoura, R. Arai, S. Baba, M. Bostock, K. Chao, K.

Heki, S. Itaba, Y. Ito, N. Kamaya, T. Maeda, J. Maury, M. Nakamura, T. Nishimura, K. Obana, K. Ohta, N. Poiata, B. Rousset, H. Sugioka, R. Takagi, T. Takahashi, A. Takeo, Y. Tu, N. Uchida, Y. Yamashita, and K. Obara (2018b), Development of a Slow Earthquake Database, *Seismological Research Letters*, 89 (4), 1566–1575, doi:10.1785/0220180021.

Kato, A., Obara, K., Igarashi, T., Tsuruoka, H., Nakagawa, S., & Hirata, N. (2012). Propagation of slow slip leading up to the 2011 Mw 9.0 Tohoku-Oki Earthquake. *Science*, **335**(6069), 705–708. https://doi.org/10.1126/science.1215141

Morii, M. (2019), Detection of astronomical moving objects using Hough transformation, Poster Presentation, Open House of The Institute of Statistical Mathematics on Jun 5, 2019 (written in Japanese), http://hdl.handle.net/10787/00033907

Nakamoto, K., Hiramatsu, Y., Uchide, T, & Imanishi, K. (2021), Cascading rupture of patches of high seismic energy release controls the growth process of episodic tremor and slip events. *Earth Planets Space* **73**, 59, https://doi.org/10.1186/s40623-021-01384-6

Obara, K. (2002), Nonvolcanic deep tremor associated with subduction in Southwest Japan, *Science, 296* (5573), 1679–1681, doi:10.1126/science.1070378.

Obara, K. (2010), Phenomenology of deep slow earthquake family in southwest Japan: Spatiotemporal characteristics and segmentation, *J. Geophys. Res.*, 115, B00A25, doi:10.1029/2008JB006048.

Obara, K., & Kato, A. (2016), Connecting slow earthquakes to huge earthquakes, *Science*, 353 (6296), 253–257, doi:10.1126/science.aaf1512.

Obara, K., Matsuzawa, T., Tanaka, S., & Maeda, T. (2012), Depth-dependent mode of tremor migration beneath Kii Peninsula, Nankai subduction zone, *Geophys. Res. Lett.*, 39, L10308, doi:10.1029/2012GL051420.

Ouillon, G., Ducorbier, C., & Sornette, D. (2008), Automatic reconstruction of fault networks from seismicity catalogs: Three-dimensional optimal anisotropic dynamic clustering, *J. Geophys. Res.*, 113, B01306, doi:10.1029/2007JB005032.

Radiguet, M., Perfettini, H., Cotte, N., Gualandi, A, Valette B., Kostoglodov V., Lhomme T., Walpersdorf A., Cabral Cano E., & Campillo, M. (2016), Triggering of the 2014 M_w7.3 Papanoa earthquake by a slow slip event in Guerrero, Mexico. *Nature Geosci* **9,** 829–833, https://doi.org/10.1038/ngeo2817

Rogers, G., & Dragert, H. (2003), Episodic tremor and slip on the cascadia subduction zone: The chatter of silent slip, *Science*, 300 (5627), 1942–1943, doi:10.1126/science.1084783.

Sagae, K., Nakahara, H., Nishimura, T., & Imanishi, K. (2021), High resolution location of deep low-frequency tremors beneath the Kii Peninsula, Nankai subduction zone, Japan, using data from a dense seismic array, *Geophysical Journal International*, 225 (2), 775–788, doi:10.1093/gji/ggab004.

Schwartz, S. Y., & Rokosky, J. M. (2007), Slow slip events and seismic tremor at circum-Pacific subduction zones, *Rev. Geophys.*, 45, RG3004, doi:10.1029/2006RG000208.

Shelly, D. (2010), Migrating tremors illuminate complex deformation beneath the seismogenic San Andreas fault. *Nature* **463,** 648–652, https://doi.org/10.1038/nature08755.

Shelly, D., Beroza, G., Ide, S., & Nakamula, S. (2006), Low-frequency earthquakes in Shikoku, Japan, and their relationship to episodic tremor and slip. *Nature* 442, 188–191, https://doi.org/10.1038/nature04931

Shelly, D. R., Beroza, G. C., & Ide, S. (2007), Complex evolution of transient slip derived from precise tremor locations in western Shikoku, Japan, *Geochem. Geophys. Geosyst*., 8, Q10014, doi:10.1029/2007GC001640.

Socquet, A., Valdes, J. P., Jara, J., Cotton, F., Walpersdorf, A., Cotte, N., Specht, S., Ortega-Culaciati, F., Carrizo, D., & Norabuena, E. (2017), An 8 month slow slip event triggers progressive nucleation of the 2014 Chile megathrust, *Geophys. Res. Lett.*, 44, 4046– 4053, doi:10.1002/2017GL073023.

Takemura, S., Noda, A., Kubota, T., Asano, Y., Matsuzawa, T., & Shiomi, K. (2019). Migrations and Clusters of Shallow Very Low Frequency Earthquakes in the Regions Surrounding Shear Stress Accumulation Peaks Along the Nankai Trough. *Geophysical Research Letters*, 46, 11830– 11840. https://doi.org/10.1029/2019GL084666

Wang, T., Zhuang, J., Buckby, J., Obara, K., & Tsuruoka, H. (2018). Identifying the recurrence patterns of nonvolcanic tremors using a 2-D hidden Markov model with extra zeros. *Journal of Geophysical Research: Solid Earth*, 123, 6802– 6825. https://doi.org/10.1029/2017JB015360

Yabe, S., & Ide, S. (2014), Spatial distribution of seismic energy rate of tectonic tremors in subduction zones, *J. Geophys. Res. Solid Earth*, 119, 8171– 8185, doi:10.1002/2014JB011383.

Fine structure of tremor migrations beneath the Kii Peninsula, Southwest Japan, extracted with a space-time Hough transform

Kodai Sagae[1,2]*, Hisashi Nakahara[1], Takeshi Nishimura[1], and Kazutoshi Imanishi[3]

[1]Department of Geophysics, Graduate School of Science, Tohoku University, 6-3, Aramaki Aza-Aoba, Aoba-ku, Sendai, Miyagi, 980-8578, Japan.

[2]Now at Geological Survey of Japan, National Institute of Advanced Industrial Science and Technology (AIST), Tsukuba Central 7, 1-1-1 Higashi, Tsukuba, Ibaraki, 305-8567, Japan.

[3]Geological Survey of Japan, National Institute of Advanced Industrial Science and Technology (AIST), Tsukuba Central 7, 1-1-1 Higashi, Tsukuba, Ibaraki, 305-8567, Japan.

Corresponding author: Kodai Sagae (k.sagae@aist.go.jp)

Key Points:

- We developed a new method using a space-time Hough transform to objectively extract tremor migrations.
- Tremor migrations show fine structures in which multiple short-duration tremor migrations occur during long-duration tremor migration.
- The relation between migration speed (V_{mi}) and duration (T) follows $V_{mi} \propto T^{-0.5}$.

Abstract

Tectonic tremors occurring on subducting plate boundaries are known to migrate at various timescales and migration speeds. Spatiotemporal patterns of tremor migration are key to investigating the rupture growth of slow earthquakes. However, spatiotemporal patterns are not sufficiently simple to visually define tremor migrations. This study developed a space-time Hough transform to objectively extract tremor migrations. The space-time Hough transform enables the extraction of multiple tremor migrations with various durations, migration directions, and migration speeds. We applied this method to a catalog of tremors for the period from 2012 to 2014, which was determined from the data analysis of a dense seismic array deployed in the Kii Peninsula, Southwest Japan. We successfully extracted 1,010 tremor migrations with durations ranging from 10 min to 24 h. Along-strike migrations propagating southwestward were predominant in the northeastern part of the Kii Peninsula, whereas those propagating northeastward were principal in the southwestern part. Regarding the along-dip direction, tremor migrations propagating in the up-dip directions were predominant in the deep part, and those propagating in the down-dip directions were principal in the shallow part. The patterns of along-strike migrations were related to the distribution of tremor energies, suggesting that tremor migrations may be controlled by heterogeneous structures of frictional properties on the plate interface. We further found that the migration speed is proportional to the inverse of the square root of the duration. This relation implies that a diffusion process controls the growth of fault ruptures behind tremor migrations.

Plain Language Summary

Tectonic tremors, which are continuous seismic signals with a predominant frequency of 2–8 Hz, have been discovered in subduction zones worldwide. The tremor activity continues for several hours to days, and source locations migrate at speeds ranging from 10 km/day to 1,000 km/day. Tremor migrations provide us with key to understanding the associated fault ruptures. However, their durations, migration directions, and migration speeds have variations that are too large to be characterized visually. Therefore, it is necessary to objectively extract the characteristics of tremor migrations. We developed a space-time Hough transform to extract tremor migrations and applied it to data from a tremor catalog in the Kii Peninsula, Southwest

Japan. We extracted 1,010 tremor migrations with durations ranging from 10 min to 24 h. The tremor migrations consist of long-duration migrations at slow speeds and short-duration migrations at high speeds. The migration speeds decreased as the durations increased, suggesting that there was a diffusive process behind tremor migrations. We identified four areas where tremor migration was active. Migration patterns are different in each area and are related to the distribution of tremor energies. The results suggest that the migration patterns may reflect the frictional properties of the plate interface.

Keywords: Tectonic tremor, Tremor migration, space-time Hough transform, Kii Peninsula, Rapid tremor reversal (RTR), slow earthquakes

1 Introduction

Slow earthquakes are phenomena in which fault ruptures grow more slowly than regular earthquakes and have been observed in subduction zones worldwide (e.g., Obara & Kato, 2016; Schwarz & Rokosky, 2007). Events with various durations detected using geodetic and seismic data are categorized as slow earthquakes: low-frequency earthquake (LFE), tectonic tremor, very low-frequency earthquake (VLFE), and slow slip event (SSE) (Obara & Kato, 2016). These events occur in the deep or shallow extensions of megathrust-locked zones. Some previous studies have detected slow earthquakes in advance of megathrust earthquakes (e.g., Ito et al., 2013; Kato et al., 2012; Radiguet et al., 2016; Socquet et al., 2017). Therefore, it is important to understand the physical processes of slow earthquakes and their connection to megathrust earthquakes.

Slow earthquakes have a significant characteristic that the source locations migrate (e.g., Hirose & Obara, 2010; Shelly et al., 2007; Takemura et al., 2019). Tremor migrations are known to exhibit the following characteristics depending on the timescale. Tremor migration with a duration ranging from several hours to days is one of the major characteristics, and this tremor migration is referred to as the main front in the present study. The main front propagates along the strike of the subducting plate at a speed of approximately 10 km/day (e.g., Houston et al., 2011; Obara, 2010). On a timescale of several hours, tremor migration at a speed of approximately 100 km/day propagates in the reverse direction of the main front, which is called rapid tremor reversal (RTR) (Houston et al., 2011). A tremor streak is a tremor migration that propagates parallel to the subducting direction at a speed of approximately 1,000 km/day on a timescale of several hours (e.g., Ghosh et al., 2010; Shelly et al., 2007). Fault ruptures of SSEs are suggested to occur behind these tremor migrations because slow earthquakes occur simultaneously (e.g., Hirose & Obara, 2010). Spatiotemporally coupled slow earthquakes are referred to as episodic tremor and slip (ETS) (Rogers & Dragert, 2003). Therefore, by assuming an ETS, it may be possible to investigate SSEs from tremor migrations (Bletery et al., 2017). Tremor migration is key to understanding the growth of fault ruptures of slow earthquakes.

Tremor migrations have been discussed as the spatiotemporal evolutions of source locations projected on the axis along the strike of a subducting plate (e.g., Houston et al., 2011; Obara, 2010). However, when we discuss the patterns of tremor migrations in detail, it is not sufficient to investigate the spatiotemporal evolutions of tremor migrations only along the strike axis. We must consider the spatiotemporal changes on an axis perpendicular to the along-strike axis as well. Moreover, because tremor migrations show complex spatiotemporal structures (e.g., Houston et al., 2011; Sagae et al., 2021), we need to develop a method to objectively extract tremor migrations and investigate their fine structures. Previous studies have developed methods for automatically extracting tremor migrations. Obara et al. (2012) extracted tremor migrations beneath the Kii Peninsula in Southwest Japan by using a two-step process. First, a linear trend was extracted from a spatiotemporal plot of tremor locations projected on the along-strike axis. Second, a tremor migration was extracted by applying the principal component analysis to the data for tremor locations and occurrence times. Bletery et al. (2017) extracted tremor migrations in Cascadia by using a different two-step process from Obara et al. (2012). In the first step, a clustering process was performed to identify clusters of tremor events and their durations. In the next step, they extracted a tremor migration in the cluster by applying linear regression to spatiotemporal plots of tremor locations projected on multiple axes.

These previous studies commonly estimated tremor migrations using linear regression on the projected axis. Thus, their methods are constrained in that there is only one migration in one time window or one cluster. To investigate the fine structures of tremor migrations, a method to extract multiple tremor migrations, regardless of the lengths of the time windows and projected axes, is necessary. Therefore, in the present study, we developed a space-time Hough transform to objectively extract tremor migrations and applied the method to data of tectonic tremors beneath the Kii Peninsula, Southwest Japan. We investigated the spatial characteristics of tremor migrations and discussed the factors controlling the growth of tremor migrations.

2 Data and Method

2.1 Data of tremor catalog

We used a catalog of tremors determined using a dense seismic array on the Kii Peninsula, Southwest Japan (Sagae et al., 2021). The catalog contained 25,155 tremor events that occurred between July 2012 and July 2014 (Figure 1). Tremor locations were determined by backprojection onto the interface of the Philippine Sea Plate (Hirose et al., 2008), and the number of detections was 2.2 times more than that obtained by the envelope correlation method (Obara, 2002) using network stations (Imanishi et al., 2011). The temporal resolution of the catalog was 1 min, and the uncertainty of the horizontal location was approximately 2.0 km on average. The tremor locations showed a belt-like distribution along the strike at depths of 30–35 km (Figure 1a). The present study defined the region where the tremor events occur as the tremor zone. We clearly observed the locations where the number of tremor events was high or low (Figure 1b). During the two years, 12 tremor episodes with durations longer than 12 h were detected, in which various tremor migrations (e.g., RTR, tremor streak) were observed.

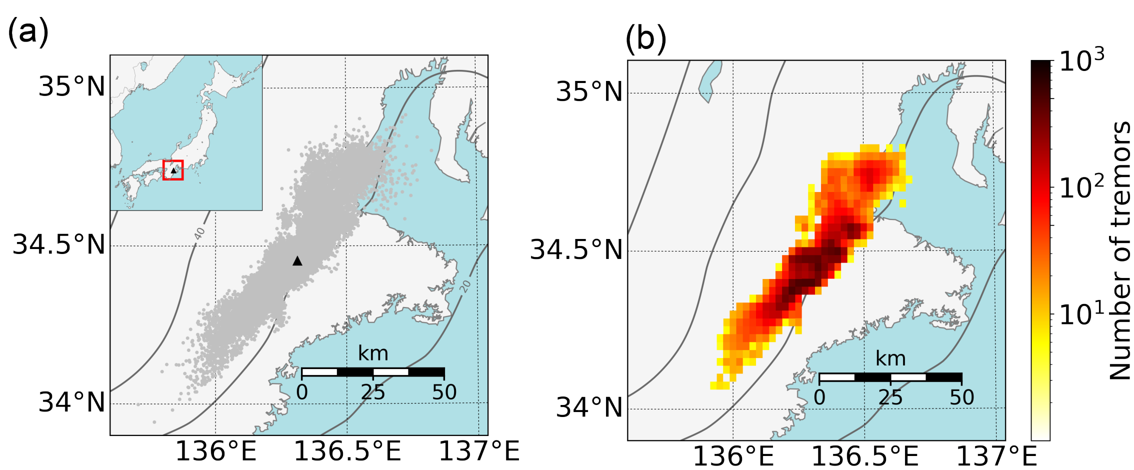

Figure 1. (**a**) Distribution of tremor locations beneath the Kii Peninsula, Southwest Japan from July 2012 to July 2014. The gray dots show tremor locations, and the black triangle shows the location of the seismic array. The solid curves show depth contours of the Philippine Sea Plate

(Hirose et al., 2008). (**b**) The number of tremor events. Colors show the cumulative number of tremor events inside cells separated by intervals of 0.025° along longitude and latitude.

2.2 Space-time Hough transform

We focused on the Hough transform (Hough, 1962) for extracting multiple tremor migrations in one time window. The Hough transform is an image-processing technique that can extract straight lines from a 2-D image. In the 2-D Hough transform, any straight line is represented by $\rho = x \cos\theta + y \sin\theta$, where x and y are the locations of an event point, ρ is the distance from the origin to the straight line, and θ is the direction of perpendicular to the straight line. Some combinations of (ρ, θ) express straight lines with different slopes that pass through an event point (x, y). These combinations of (ρ, θ) constitute a sine curve in the space of (ρ, θ). The best straight line is extracted by searching for the combination of (ρ, θ) where the sine curve calculated for each event point intersects the most. A technique of counting the number of intersections is called "vote". Even if there are multiple straight lines in a 2-D image, the method can distinguish these lines as different combinations of (ρ, θ). Therefore, the 2-D Hough transform enables us to extract multiple straight lines from the image by the technique of "vote". The Hough transform in 3-D space can be used to extract planes. In seismology, the 3-D Hough transform has the potential to extract a fault plane by applying the method to the data of seismic source locations (longitude, latitude, and depth). However, a previous study has established some limitations of the Hough transform (Ouillon et al., 2008). First, the method cannot determine the spatial extent of the straight line or plane because those represented by the combination of parameters have an infinite length or size. Second, the Hough transform cannot deal with the spatial spread of a straight line or plane (e.g., fault thickness) because the equations that express them do not consider the uncertainty of the source location. Given our situation, we consider the plate boundary as the fault plane by assuming that tremors occur on the plate interface because previous studies have reported that LFEs and tremors occur near the plate boundary (e.g., Ghosh et al., 2012; Shelly et al., 2006). Tremor migration (temporal evolution of tremor locations on the plane) is represented by a straight line in a (2+1)-D space-time (2-D in the plane and 1-D in time) by assuming a constant migration speed in a duration. However, the conventional Hough transform cannot extract a straight line because additional information on the direction vector within the plane is necessary. Therefore, we must introduce a new Hough transform to extract a straight line in the (2+1)-D space-time, considering the uncertainties of the tremor locations.

A previous study in astronomy extracted a straight line in the (2+1)-D space-time using the Hough transform to investigate the movements of celestial bodies in observed images (Morii, 2019). Motivated by a previous study, we newly developed a space-time Hough transform to extract tremor migrations as straight lines in the (2+1)-D space-time. A new point of our method is that we can consider the uncertainties of tremor locations in the extraction of tremor migration by giving spatial spread to the straight line (by considering a cylinder). We consider (x, y, t) as a coordinate of a tremor event, where x is the longitude (the east is positive), y is the latitude (the north is positive), and t is the detection time. An arbitrary position of the straight line in the (2+1)-D space-time is represented using tyt-Euler angle (Figure 2). The tyt-Euler angle shows rotations of the coordinate system by θ, ϕ, and ψ, where θ is the zenith angle, ϕ is the azimuth, and ψ is the rotation angle. The details of the Euler angle are provided in the Supporting Information (Text S1). The equation of the straight line in (2+1)-D space-time is represented as follows:

$$\begin{pmatrix} x \\ y \\ t \end{pmatrix} = (\rho + r\cos\lambda)\,\vec{\alpha} + (r\sin\lambda)\,\vec{\beta} + m\,\vec{\gamma}\,, \tag{1}$$

where

$$\vec{\alpha} = \begin{pmatrix} -\sin\phi\sin\psi + \cos\theta\cos\phi\cos\psi \\ \cos\phi\sin\psi + \cos\theta\sin\phi\cos\psi \\ -\sin\theta\cos\psi \end{pmatrix}$$

$$\vec{\beta} = \begin{pmatrix} -\sin\phi\cos\psi - \cos\theta\cos\phi\sin\psi \\ \cos\phi\cos\psi - \cos\theta\sin\phi\sin\psi \\ \sin\theta\sin\psi \end{pmatrix} \tag{2}$$

$$\vec{\gamma} = \begin{pmatrix} \sin\theta\cos\phi \\ \sin\theta\sin\phi \\ \cos\theta \end{pmatrix},$$

ρ is the distance from the origin to the straight line (cylindrical axis), λ is the parameter that expresses the angle around the cylindrical axis measured counterclockwise from the vector $\vec{\alpha}$, and m is the parameter that determines the position on the straight line. r is the radius of the cylinder, with values ranging from zero to r_{max}, where r_{max} corresponds to the location uncertainty. $\vec{\gamma}$ is the unit direction vector of the straight line, $\vec{\alpha}$ is the unit vector in the same direction as the foot of the perpendicular line ($\rho\vec{\alpha}$), and $\vec{\beta}$ is the unit vector perpendicular to both $\vec{\alpha}$ and $\vec{\gamma}$. The vectors of $\vec{\alpha}$ and $\vec{\beta}$ are within the plane shown by the large blue circle in Figure 2a. Thus, any position of the cylinder in (2+1)-D space-time can be represented by four parameters (ρ, θ, ϕ, ψ). In particular, we can represent the migration speed as $\tan\theta$ and the migration direction as ϕ. When a tremor event is included inside the cylinder, the parameter m is eliminated from Equation 1:

$$\begin{cases} X = \rho\sin\psi + r\sin(\lambda+\psi) = -x\sin\phi + y\cos\phi \\ Y = \rho\cos\psi + r\cos(\lambda+\psi) = x\cos\theta\cos\phi + y\cos\theta\sin\phi - t\sin\theta \end{cases} . \tag{3}$$

The parameter λ is eliminated using Equation 3:

$$(X - \rho\sin\psi)^2 + (Y - \rho\cos\psi)^2 \leq r_{max}^2 . \tag{4}$$

In the space-time Hough transform, we prepare bins of parameters (ρ, θ, ϕ, ψ) that correspond to straight lines. We perform a “vote” to the corresponding “bin” when a tremor event satisfies Equation 4. The bin with the maximum number of votes represents the straight line that best explains the event data. When there are multiple straight lines that show large number of votes in the same time window, these lines can be extracted separately by the Hough transform because votes for different lines are cast on different “bins”. This advantage enables us to relax the constraint of one migration in one time window imposed in previous studies. The square root of the left-hand side of Equation 4 expresses the space-time distance (D_{st}) between the tremor event and the cylindrical axis:

$$D_{st} = \sqrt{\delta x^2 + \delta y^2 + C^2 \delta t^2}\,, \tag{5}$$

where δx and δy are spatial errors with respect to the cylindrical axis, δt is the temporal error, and C is the parameter that connects space and time with a unit of speed. When we set the radius of the cylinder (r_{max}) based on the uncertainty of the tremor location, the space-time Hough transform can extract tremor migrations by considering the tremor uncertainties. In this case, parameter C should be set such that r_{max}/C is equal to the temporal resolution of the tremor catalog. If C is set smaller than the above value, the time series of tremor events projected onto the straight line may change from the original values because the temporal error is allowed up to r_{max}/C (the temporal error may exceed the temporal resolution of the catalog).

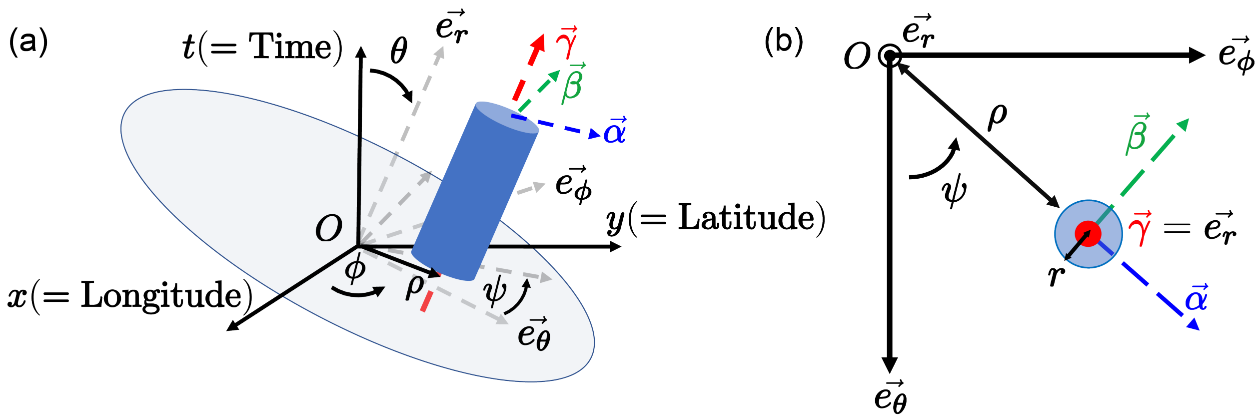

Figure 2. (**a**) Schematic diagram of the space-time Hough transform. x is the longitude (the east is positive), y is the latitude (the north is positive), and t is the detection time. ρ is the distance from the origin to the straight line (cylindrical axis), θ is the zenith angle, ϕ is the azimuth, and ψ is the rotation angle. The large blue circle shows a plane perpendicular to the unit direction vector of the straight line ($\vec{\gamma}$). (**b**) Schematic diagram of the coordinate around the vector $\vec{\gamma}$. The vectors of $\overrightarrow{e_\theta}$, $\overrightarrow{e_\phi}$, and $\overrightarrow{e_r}$ are standard unit vectors, which are consistent with those in the polar coordinate system. r is the radius of the cylinder.

2.3 Data processing

Before applying the space-time Hough transform to the tremor catalog data, we set the values of parameters r_{max} and C. In the present study, r_{max} was set to 2.5 km based on the mean uncertainty of the horizontal location in the tremor catalog (Sagae et al., 2021). C was set to 150 km/hr (= 2.5 km/min) because the temporal resolution of the catalog was 1 min. The tremor locations (longitude, latitude) were converted to a plane rectangular coordinate system (x, y) in kilometers, with the origin set at the center of the seismic array (136.31°E, 34.45°N) by using the code of EPSG:6674. We prepared bins of parameters (ρ, θ, ϕ, ψ) to extract tremor migrations using the space-time Hough transform. ρ was set in a range of 0–120 km with an interval of 0.25 km, ϕ and ψ were set in a range of 0–350° with an interval of 10 °, and θ ($\tan\theta$) was set in a range of 2–60 km/hr with an interval of 1 km/hr in addition to (0.125, 0.25, 0.5, 0.75, 1.0, 1.25, and 1.5) km/hr.

We prepared time windows with lengths (T_w) of 1, 2, 3, 4, 6, 8, 12, and 24 h to extract tremor migrations for various durations. In each time window, we applied a clustering process to a time series to determine the temporal extent of tremor migrations. Our clustering process for time series is different from that of Bletery et al. (2017), who identified a cluster of tremor events with a length of time window by clustering. Firstly, we define a first tremor event in the time window and make a “cluster”. The detection time for the first tremor event is t_1. Secondly, we define the i-th tremor event that occurred after the first tremor event as the i-th target event with a detection time of t_i. We calculate the time interval $t_i - t_{i-1}$ between the target event and the previous event that occurred immediately before. Finally, if the time interval is shorter than $5\times T_w$ minutes, the target event is classified into a “cluster” to which the previous event belongs. For example, when $t_2 - t_1$ is shorter than $5\times T_w$, the second target event is classified into the cluster to which the first tremor event belongs. If the time interval is longer than $5\times T_w$ minutes, the target event is classified into a new “cluster”. We determined the time interval ($5\times T_w$) for the clustering by trial and error, while visually checking tremor migrations extracted in the time window of T_w =1 h. The time interval is considered to be related to the detection capability of the tremor catalog. As the tremor distribution becomes spatiotemporally sparse in the low-quality catalog, tremor migrations are not visible on a short timescale. In this case, the time interval should be increased.

After clustering, we applied the space-time Hough transform to the clusters of tremor events in the time window of each length (T_w) as follows:

(A) We select a time window that contains ten or more tremor events while moving the window from the beginning of the catalog without overlapping.

(B) We perform a "vote" to a corresponding "bin" when a tremor event within a cluster estimated by clustering satisfies Equation 4. We extract a tremor migration whose "bin" (ρ, θ, ϕ, ψ) shows the maximum number of votes. In the present study, the number of votes must be eight or more. When multiple "bins" show the same maximum number of votes, we extract the tremor migration that minimizes the mean values of space-time distances (D_{st}, Equation 5) averaged over voted tremor events.

(C) Tremor events belonging to the tremor migration are removed from the cluster. If the cluster still contains ten or more tremor events, we return to (B) and further extract tremor migrations in the cluster. When the maximum "bin" contains eight or more votes, we perform a "re-vote", which is a "vote" including the removed tremor events. This is because there may be tremor events belonging to multiple tremor migrations among the removed ones. If there are less than ten tremor events in the cluster or the maximum number of votes is less than eight, we deal with other clusters in the time window. When the searches of all clusters in the time window are completed, we return to (A) and select the other time windows that satisfy the condition of (A).

A detailed flowchart of the above process is shown in Figure 3. We define the duration of the tremor migration as $t_{max} - t_{min}$, where t_{min} is the detection time of the first tremor event included in the tremor migration and t_{max} is the detection time of the last tremor event. After tremor migrations are extracted in all time windows, overlapping ones with the same parameters (e.g., date and time, duration, ρ, and ϕ) extracted in multiple time windows are removed.

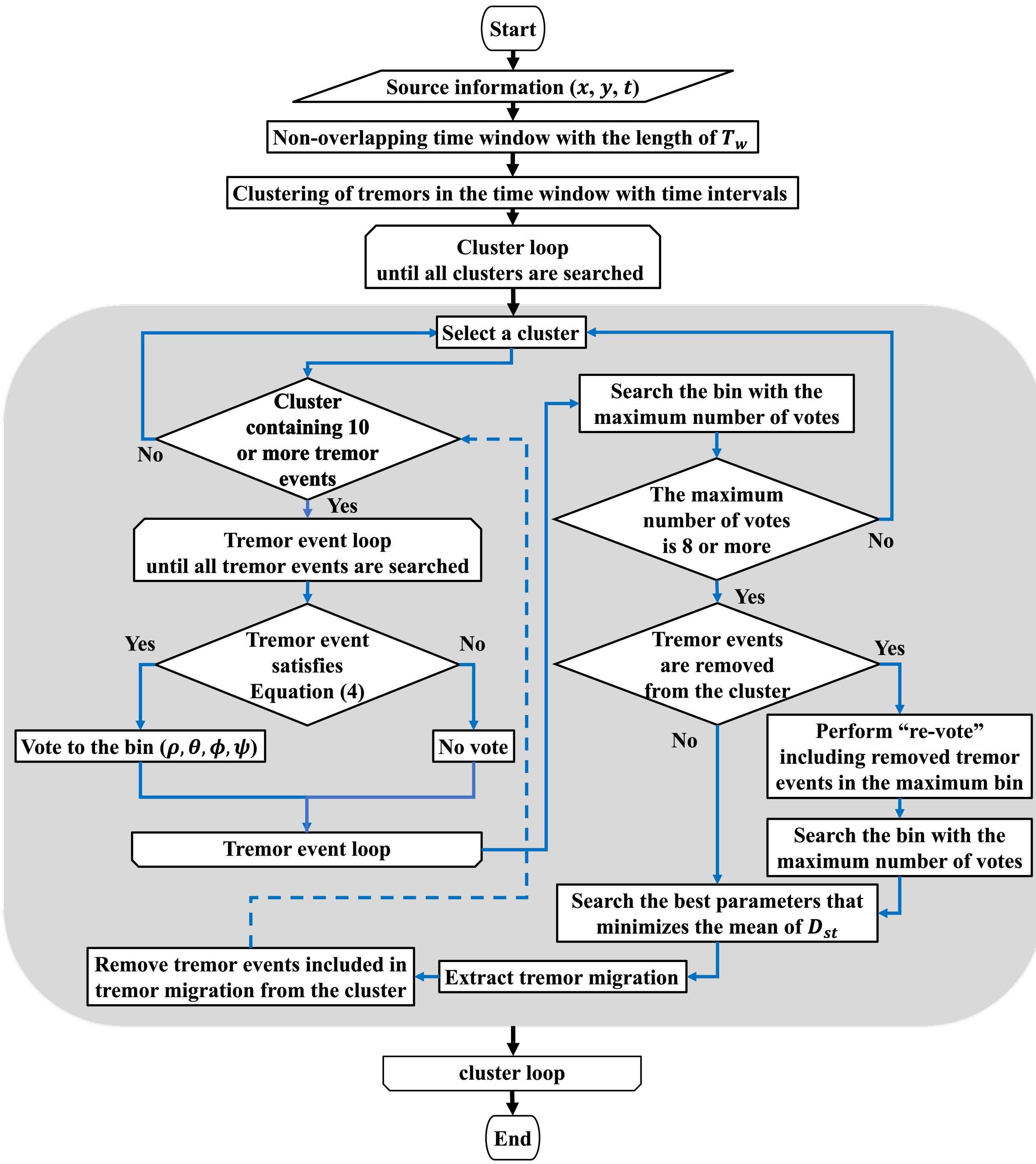

Figure 3. Flowchart of the space-time Hough transform.

Figure 4 shows an example of votes for a tremor migration with a duration of 22 min. Each panel shows the number of votes for the two parameters by fixing the remaining two parameters to the best values. In this tremor migration, the maximum number of votes is 20, as shown by the white stars in Figure 4. From the maximum values, the space-time Hough transform objectively determines candidates of the best parameters for tremor migrations by the technique of "vote". When there are multiple candidates with the same maximum number of votes, we use the space-time distance (D_{st}, Equation 5) to identify the best parameters. Figure 5 shows the distribution of the space-time distance (D_{st}) for the candidate parameters in Figure 4. The red dots are the mean values of D_{st} for the candidates, and the black cross is the minimum value. The minimum value of the mean D_{st} enables determination of the best parameters among the candidates (ρ, θ, ϕ, ψ) with the maximum number of votes. Figure 6 shows an example of tremor migrations extracted in a time window with a length of 2 h. We succeeded in extracting three different tremor migrations with the durations of 22 min, 36 min, and 53 min during the 2 h. The tremor migration with the duration of 22 min (red line) is the example shown in Figures 4 and 5. Our method can objectively extract the complex patterns of tremor migrations in a zigzag style. This result means that the space-time Hough transform newly developed in the present study enables us to extract multiple tremor migrations with various durations regardless of the length of the time window.

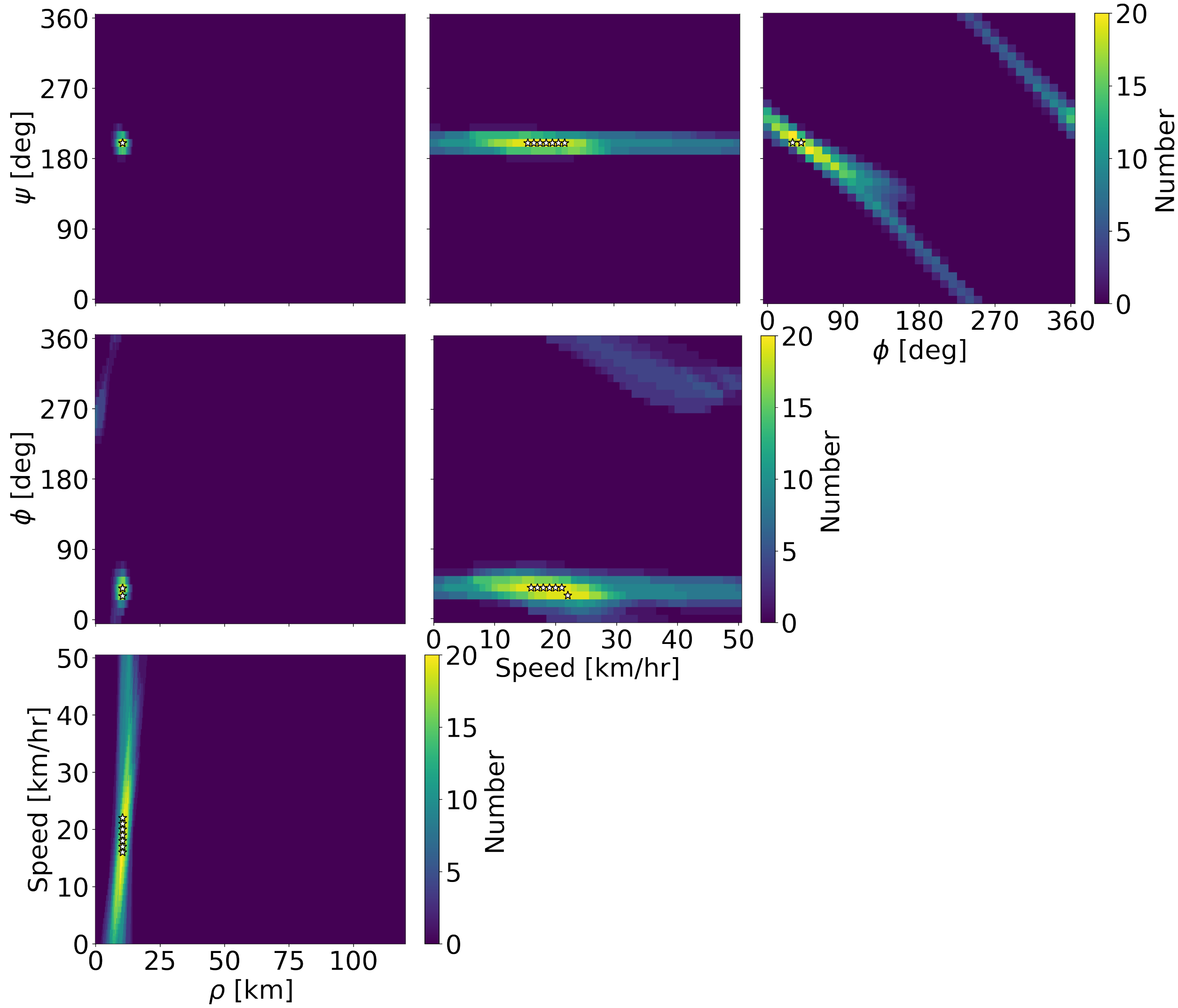

Figure 4. The number of votes for tremor migration with the duration of 22 min. Color bar shows the number of votes. Each panel shows the number of votes for two parameters by fixing the remaining two parameters to the best ones. The maximum number of votes is 20. The white stars show candidates of the best parameters with the same maximum votes. The best parameters of the tremor migration are $\rho = 10.5$ km, migration speed $(= \tan\theta) = 17$ km/hr, $\phi = 40°$, and $\psi = 200°$ as shown in Figure 5.

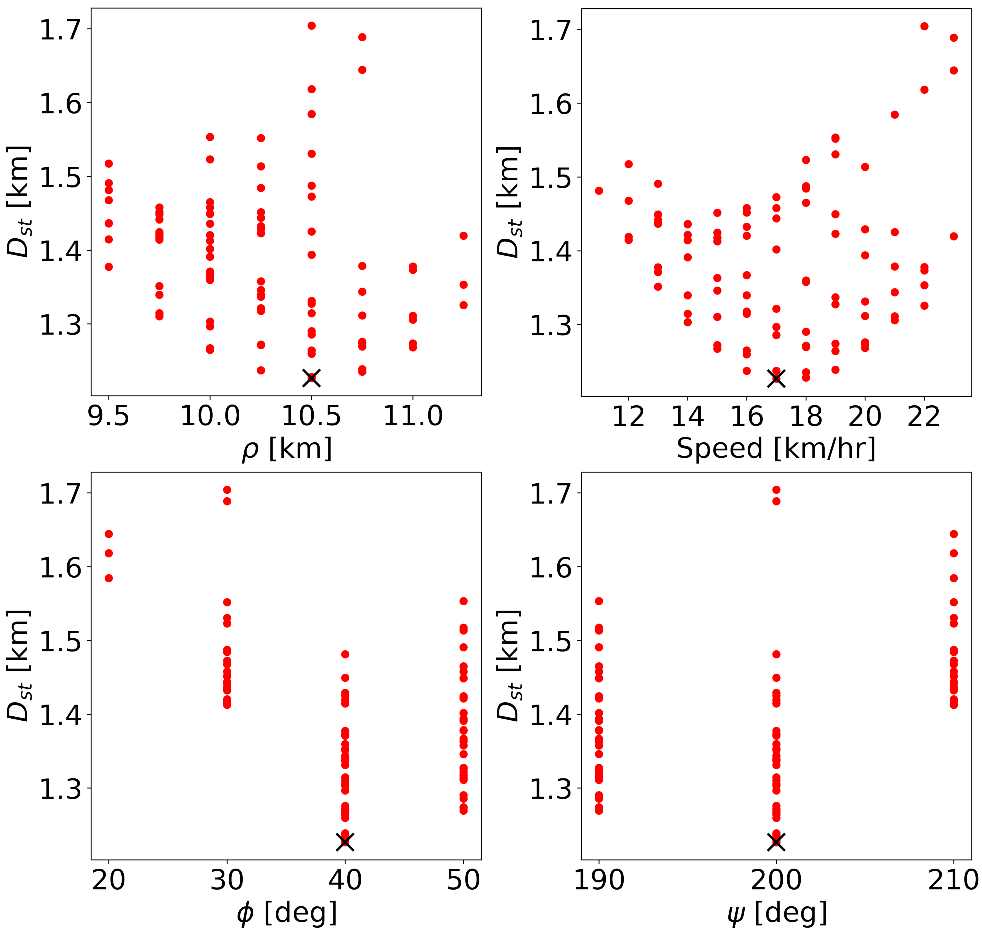

Figure 5. Distribution of space-time distance (D_{st}) for candidates of parameters with the same maximum number of votes. The candidates are combinations of parameters with the maximum votes in Figure 4. The red dots show mean D_{st} values whose maximum number of votes is 20. The black cross shows the minimum value of the mean D_{st}.

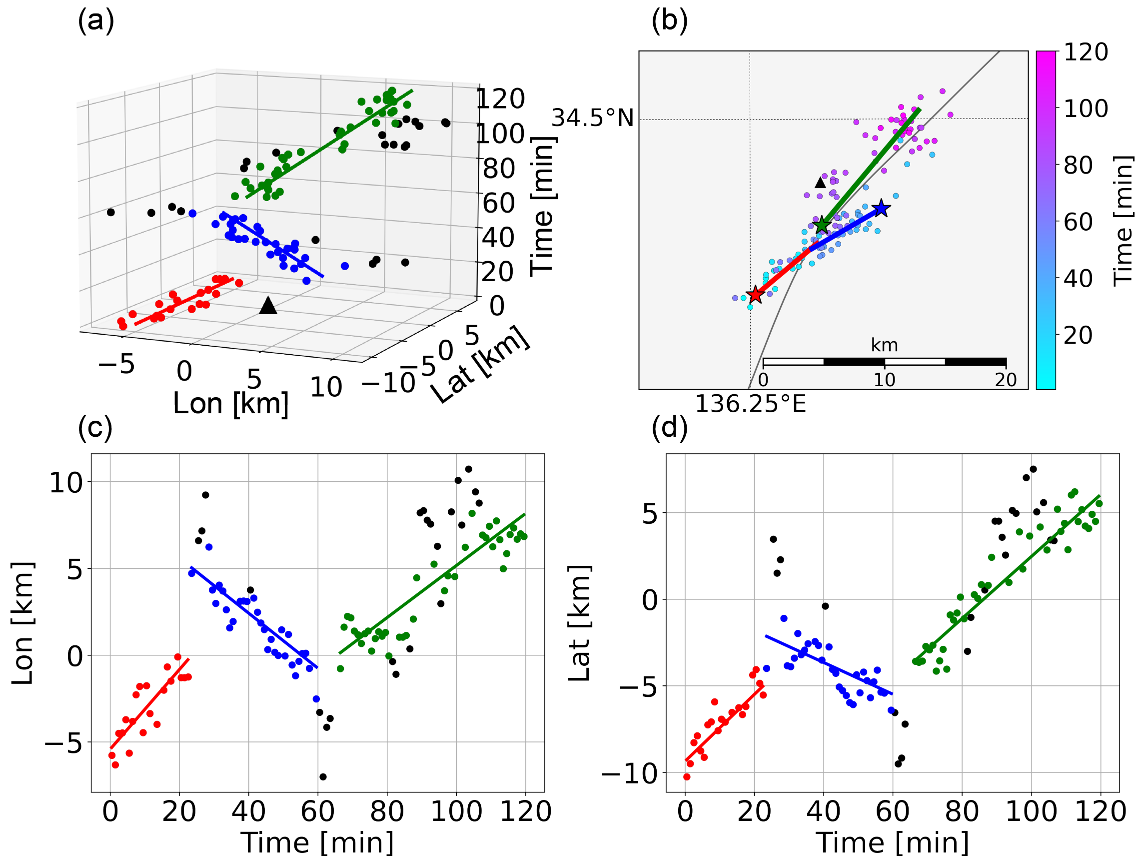

Figure 6. An example of tremor migrations extracted in one time window with the length of 2 h. (**a**) Tremor migrations in the (2+1)-D space-time. The red, blue, and green lines show tremor migrations with durations of 22 min, 36 min, and 53 min, respectively. The red, blue, and green dots show tremor events composing each tremor migration. The black dots are tremor events that do not belong to tremor migrations. The black triangle shows the origin set at the location of the array (136.31°E, 34.45°N). (**b**) Map view of tremor migrations. Each line shows tremor migrations and the colored stars are starting points of the three tremor migrations. The dots and their colors represent tremor locations and their timings. (**c**) Space-time plot of tremors between the longitude and the time. (**d**) Space-time plot of tremors between the latitude and the time.

3 Results

3.1 Tremor migrations extracted during a tremor episode

During the two years from July 2012 to July 2014, we succeeded in extracting 1,010 tremor migrations with durations ranging from 10 min to 24 h (Figure 7). Tremor migrations were categorized into four patterns based on their migration directions. We defined the along-strike direction as 45° clockwise from the north and the along-dip direction as perpendicular to the strike. The tremor migrations are represented by the lines with different colors: the red lines express tremor migrations with directions of 0–90° clockwise from the north (northeast direction); the blue lines represent those with directions of 180–270° (southwest direction); the yellow lines represent those with directions of 90–180° (up-dip direction), and the green lines represent those with directions of 270–360° (down-dip direction). Tremor migrations appear to behave differently depending on area. The details are presented in Section 3.2.

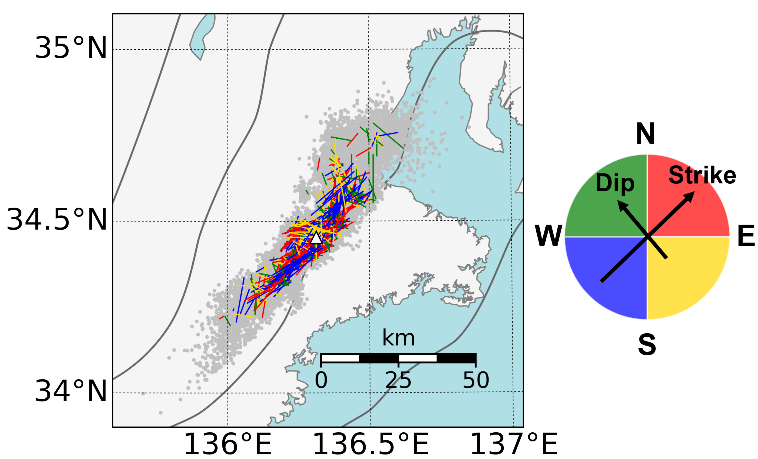

Figure 7. Distribution of tremor migrations from July 2012 to July 2014. The gray dots show tremor locations, and the white triangle shows the location of the seismic array. The lines show directions of tremor migrations, where red lines are directions of 0–90° clockwise from the north (northeast direction), blue lines are directions of 180–270° (southwest direction), yellow lines are directions of 90–180° (up-dip direction), and green lines are directions of 270–360° (down-dip direction), respectively. The color diagram is shown on the right.

Figure 8 shows examples of tremor migrations that are extracted during a tremor episode from August 11th to 16th, 2012. In this tremor episode, Sagae et al. (2021) found a pattern of the main front by visual inspection: tremors started from the down-dip side of the tremor zone, first propagated in the up-dip direction, and then migrated northeastward and southwestward. The present study extracted 171 tremor migrations during the same tremor episode. Figures 8a and 8b show 120 tremor migrations with durations ranging from 10 min to 1 h. We detected not only RTRs and tremor streaks reported in Sagae et al. (2021) but also many complex tremor migrations that were not easily identified by visual inspection. Figures 8c and 8d show 38 tremor migrations with durations ranging from 1 h to 6 h, and Figures 8e and 8f represent 13 tremor migrations with durations ranging from 6 h to 24 h. These 51 tremor migrations show up-dip migrations and bilateral migrations along the strike. In particular, up-dip migrations in the initial stage of the tremor episode (August 11th in Figure 8) show not only the along-dip component but also the along-strike component (northeast direction). Tremor migrations in the other episodes propagate in the similar path (Figure S8). Figure 9 zooms up the tremor episode occurring on August 13th, 2012 to see fine structures of spatiotemporal distribution of tremor migrations. By comparing tremor migrations with different durations (00:00–14:00 in Figures 9b, 9d, and 9f), we recognized multiple tremor migrations with short durations within those with long durations. We further noticed that migration speeds slowed down as durations increased. The relationship between migration speed and duration is discussed in Section 4.3. Focusing on tremor migrations with durations ranging from 6 h and 24 h, we found that multiple straight lines appear to be parallel (Figure 9f). This result shows that the tremor migrations have spatial spread beyond the uncertainties of the tremor locations. In the present study, we can judge whether or not tremor migrations spread two-dimensionally because the space-time Hough transform can extract tremor migrations considering the uncertainties of tremor locations. This is an advantage of the space-time Hough transform. Results of other tremor episodes are shown in the Supporting Information (Figures S2–S12).

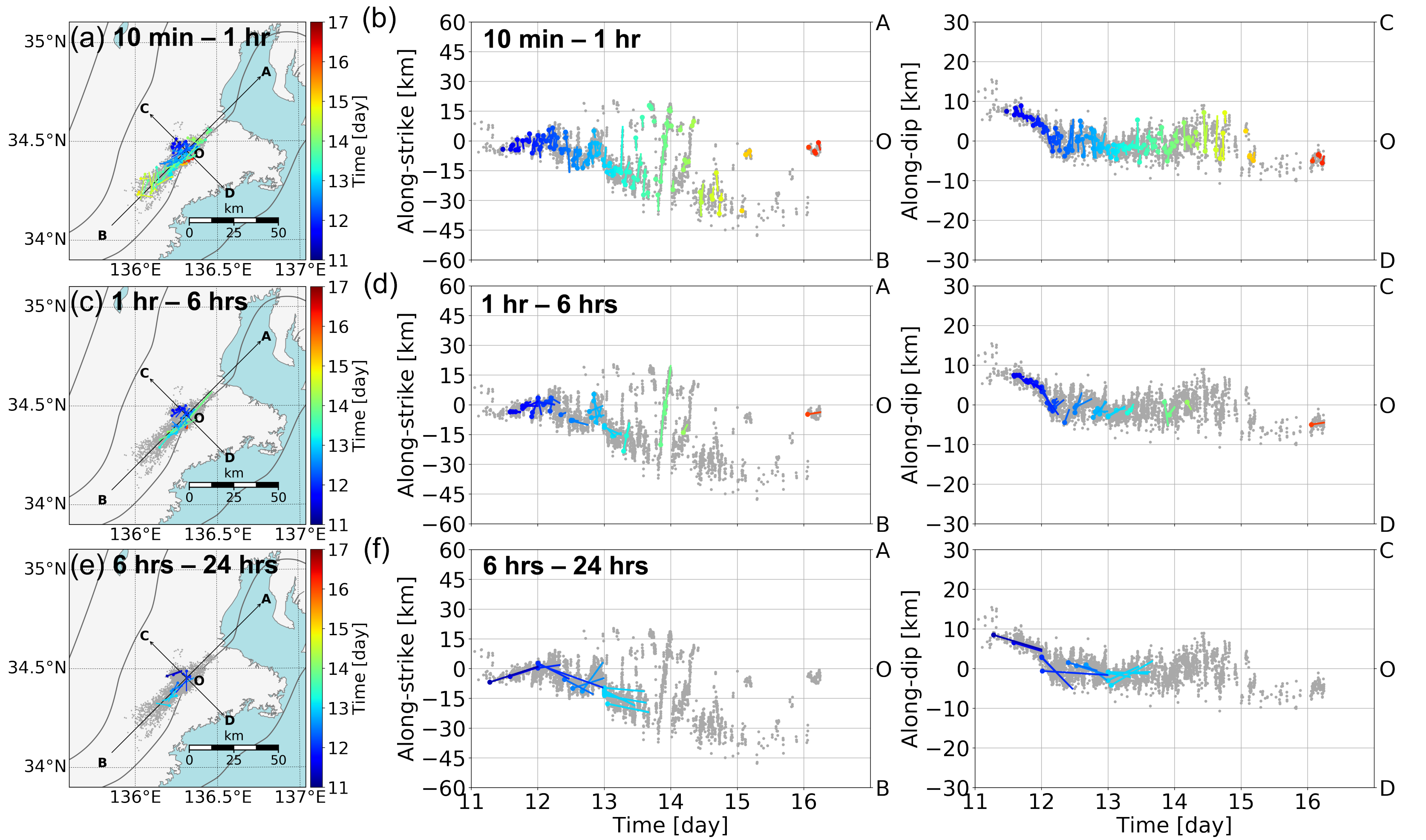

Figure 8. Tremor migrations during a tremor episode from August 11th to 16th, 2012. (**a**) Map view of the tremor migrations with durations ranging from 10 min to 1 h. The gray dots show tremor locations. Colored lines and dots show tremor migrations and their starting points, and the colors show the starting time of tremor migrations. (**b**) Spatiotemporal plots of the tremor migrations with the same durations as that of (**a**). The left panel shows spatiotemporal evolutions of tremor migrations along the strike (A–B) and the right

panel shows spatiotemporal evolutions of those along the dip (C–D). (**c**), (**d**) Same as (**a**) and (**b**), but for tremor migrations with durations ranging from 1 h to 6 h. (**e**), (**f**) Same as (**a**) and (**b**), but for tremor migrations with durations ranging from 6 h to 24 h.

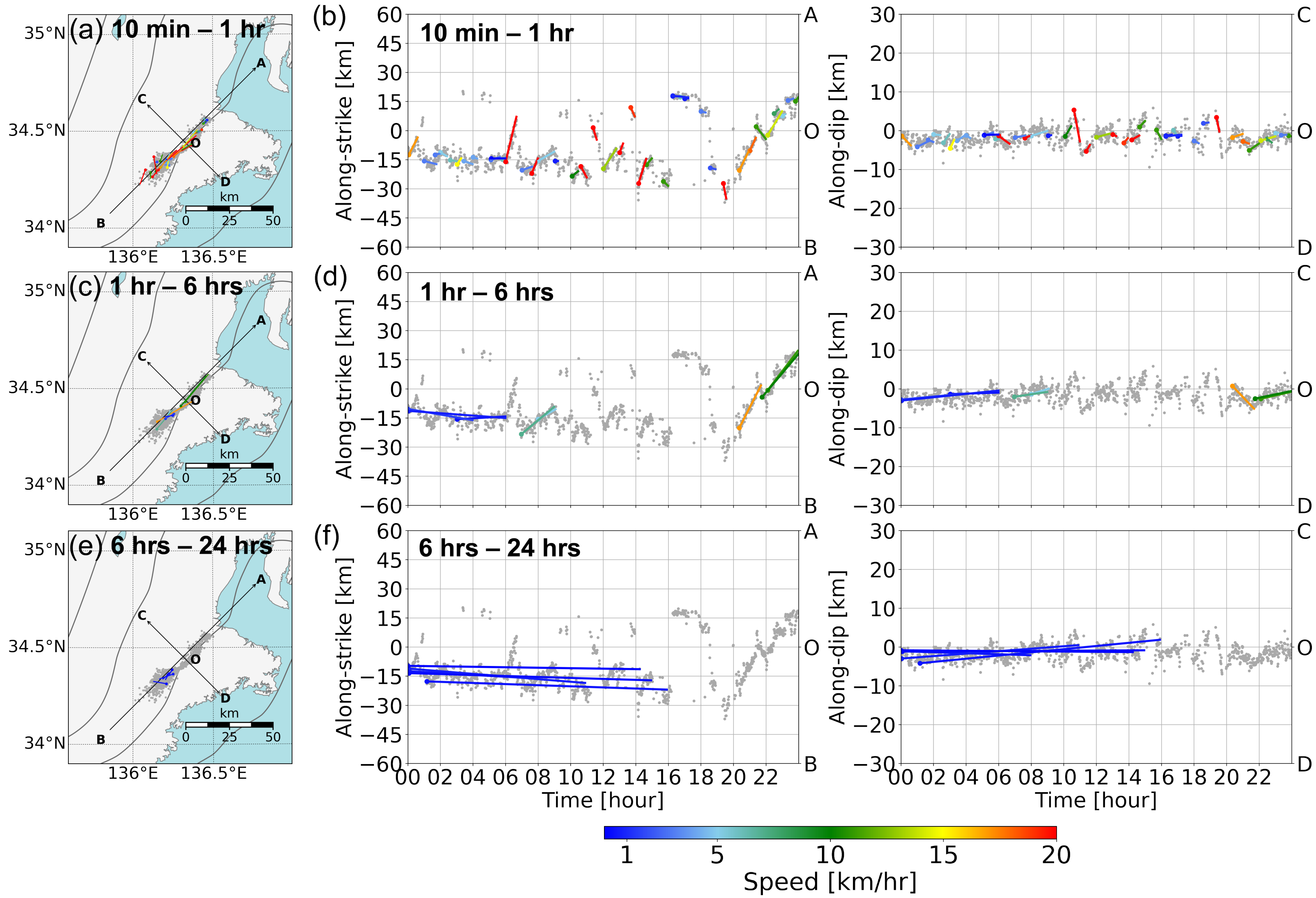

386 **Figure 9.** Same as Figure 8, but for tremor migrations zooming on August 13th, 2012. The colors show migration speeds.

3.2 Spatial distribution of tremor migrations

Figure 10a shows the frequency distribution of tremor events included in the tremor migrations. The number of tremor events was counted inside cells that are arranged at intervals of 0.025° along longitude and latitude. Comparing the spatial distribution of all tremor events (Figure 1b) and the frequency in Figure 10a, we found four areas (R1–R4) where the frequency of tremor events was relatively high beneath the Kii Peninsula. Figure 10b shows the spatial distribution of the predominant directions of tremor migrations. For each cell, we calculated predominant directions of tremor migrations as a ratio of the number of tremor migrations with directions of 0–90° and 180–270° over the total number of tremor migrations with directions of 0–360°. Our result shows that along-strike migrations (violet) are more predominant on the up-dip side of the tremor zone. This characteristic is similar to that reported by Obara et al. (2012). Moreover, we found that along-dip migrations (orange) were predominant in R1 and R3, and along-strike migrations were principal in R2 and R4 (Figure 10b). The areas R2 and R4 correspond to the areas where RTRs were reported by visual checking in Sagae et al. (2021). The characteristics of R1–R4 are discussed in more detail in Section 4.1.

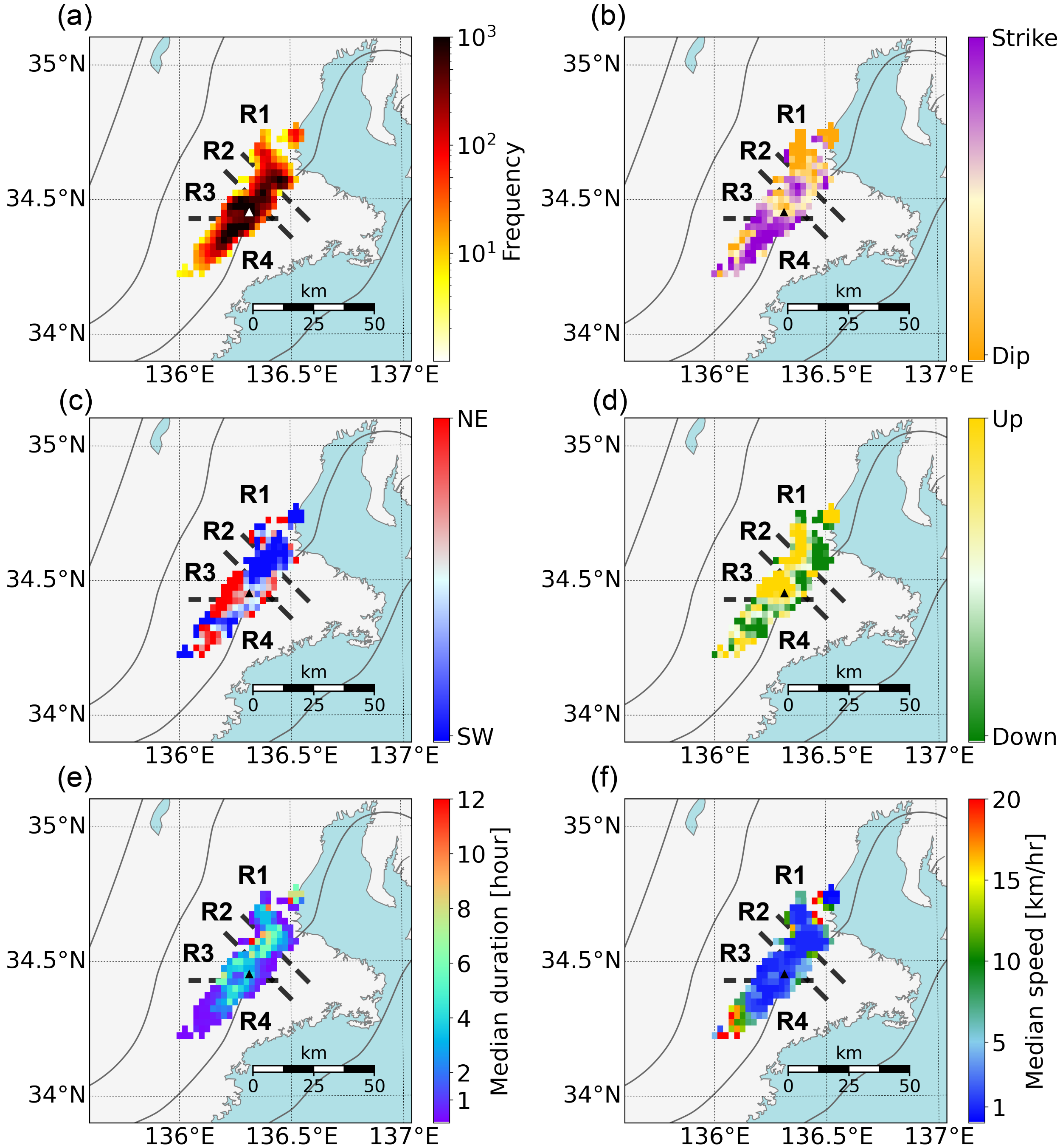

404 **Figure 10.** (**a**) Frequency distribution of tremor events included in tremor migrations. The white
405 triangle shows the location of the array. The color bar shows the frequency of tremor events. The
406 dashed lines are additional lines to distinguish the areas R1–R4, where the frequency of tremor
407 events is high. (**b**) Spatial distribution of predominant directions of tremor migrations. The black
408 triangle shows the location of the array. The violet color shows that tremor migrations along the
409 strike are predominant (0–90° and 180–270° clockwise from the north), and the orange color

shows that tremor migrations along the dip are predominant (90–180° and 270–360°). (**c**) Spatial distribution of predominant directions of tremor migrations along the strike. The red and blue colors show the predominant directions of the northeast (0–90°) and southwest (180–270°), respectively. (**d**) Spatial distribution of predominant directions of tremor migrations along the dip. The yellow and green colors show predominant directions of the up-dip (90–180°) and down-dip (270–360°), respectively. (**e**) Spatial distribution of median duration of tremor migrations. (**f**) Spatial distribution of median speed of tremor migrations.

Figures 10c and 10d show the predominant directions of tremor migrations along the strike and dip, respectively. The predominant direction along the strike was defined as the ratio of the number of tremor migrations with directions of 0–90° over the total number of along-strike migrations with directions of 0–90° and 180–270°. The predominant direction along the dip was the ratio of the number of tremor migrations with directions of 90–180° over the total number of along-dip migrations with directions of 90–180° and 270–360°. Regarding the along-strike direction (Figure 10c), we observed significant changes in the predominant directions at the boundary between R2 and R3. Northeastward tremor migrations (red) were predominant in the southwest area, while southwestward tremor migrations (blue) were principal in the northeast area. For the along-dip direction (Figure 10d), up-dip migrations (yellow) were predominant on the down-dip side of the tremor zone and down-dip migrations (green) were principal on the up-dip side. This characteristic of along-dip migrations is a new finding of the present study.

To characterize the spatial distribution of the duration and speed of tremor migrations, we calculated the median values for each cell. The results are presented in Figures 10e and 10f. Areas where the median duration is relatively long (6 h or more) correspond well to those where the median speed is relatively slow (1 km/hr or less). The main front is characterized by a duration ranging from several hours to days and a speed of approximately 10 km/day. The values of the long median duration and slow median speed were consistent with the characteristics of the main front. Our results show the locations where the main front with long durations often occurs. When we investigated tremor migrations with high speeds (10 km/hr or more), their spatial characteristics were different from the patterns of the main front shown in Figure 10. Figure 11a shows the predominant directions of along-strike tremor migrations with speeds of 10 km/hr or more. Areas where southwestward tremor migrations are predominant in Figure 10c (blue) change their patterns to those where northeastward tremor migrations are principal (red in Figure 11a). Figure 11b shows spatial distribution of the median speed for tremor migrations with speeds of 10 km/hr or more. Tremor migrations with high speeds were found even in areas where the median duration was relatively long and the median speed was slow. These results show that high-speed tremor migrations occur inside the main front and that the inside of the main front is rich in spatiotemporal variations in tremor migrations. Thus, our results reveal fine structures of tremor migrations not only in time (Figures 8 and 9) but also in space (Figures 10 and 11).

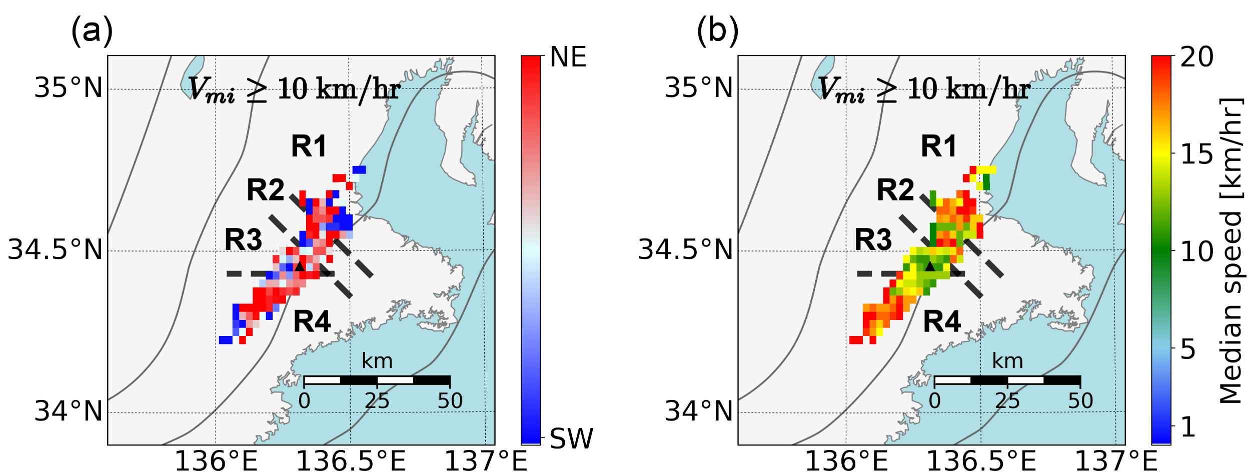

Figure 11. (**a**) Spatial distribution of predominant directions of tremor migrations with high speeds along the strike. The dashed lines and the black triangle are the same as those in Figure 10. Tremor migrations with speeds of 10 km/hr or more are used to estimate the migration patterns. Colors are the same as those in Figure 10c. (**b)** Spatial distribution of median speed of tremor migrations with speeds of 10 km/hr or more. Colors are the same as those in Figure 10f.

4 Discussions

4.1 Comparison of the spatial distribution of tremor migrations with previous studies

We describe the characteristics of the four areas (R1–R4) in further detail. In area R1, tremor migrations had a component propagating southwestward (Figure 10c), although along-dip migrations were predominant (Figure 10b). Up-dip migrations were predominant on the down-dip side of the tremor zone (Figure 10d). This result corresponds to the observations that tremors start from the down-dip side of the tremor zone and propagate in the up-dip direction (Sagae et al., 2021).

For area R2, previous studies established that tremor episodes tended to stop in R2 (e.g., Nakamoto et al., 2021; Sagae et al., 2021), and that there were tremor patches with high radiated energies in R2 (Nakamoto et al., 2021; Yabe & Ide, 2014). The present study shows that along-strike migrations are predominant (Figure 10b) and tremor migrations tend to propagate southwestward (Figure 10c). Although tremor migrations with high speeds of 10 km/hr or more were predominant in along-strike directions beneath most of the Kii Peninsula, along-dip migrations were principal in R2 (Figure S13). This result suggests that area R2 is a characteristic field (e.g., tremor patches arranged subparallel to the dip; fluid conduits along the dip) to generate tremor streaks along the dip, as observed in a previous study (Figure S14 in Sagae et al., 2021). The implications of tremor streaks are outside the scope of the present study.

In area R3, along-dip migrations were predominant (Figure 10b) and tremor migrations propagated not only in the up-dip direction but also northeastward (Figures 10c and 10d). When tremor migrations reach the upper limit of the tremor zone, they are less likely to propagate from R3 to R1 beyond R2. This characteristic is observed as changes in the predominant direction of the along-strike migration around the boundary between R2 and R3 (Figure 10c). Previous studies have also observed these characteristics (e.g., Ando et al., 2012; Sagae et al., 2021).

In area R4, tremor migrations were predominant in the along-strike direction (Figure 10b). In addition, tremor migrations on the up-dip side of the tremor zone propagated in both the northeast and the southwest directions (white color in Figure 10c). These results reflect the observations that RTRs repeatedly occur in R4 (Sagae et al., 2021). Interestingly, most of the tremor migrations propagated in the down-dip direction (Figure 10d), and up-dip migrations propagating directly from R3 to R4 rarely occurred. This characteristic is obtained from the results that the down-dip migration and the along-strike migration propagating northeastward are principal around the boundary between R3 and R4 (Figures 10c and 10d).

Previous studies have investigated the characteristics of tremor migrations beneath the Kii Peninsula (Obara et al., 2012; Wang et al., 2018). Wang et al. (2018) classified tremor locations beneath the Kii Peninsula into 17 segments using a 2-D Hidden Markov model and examined tremor activities among the segments. They calculated transition probabilities which explained the migration patterns among the segments. Furthermore, areas with high transition probabilities of tremor activities among the segments were classified into four subsystems along the strike (K1–K4, Figure 6 in Wang et al., 2018). Subsystems K3 and K4 in their results included the four areas with the high frequency of tremor events (R1–R4) in our results. Some characteristics of tremor migrations in R1–R4 are recognized in tremor activities among the segments reported by Wang et al. (2018). For example, up-dip migrations propagating northeastward were found in R3 (propagation from segment 10 to 11, Figure 6 in Wang et al., 2018). There were almost no up-dip migrations propagating directly from R3 to R4 (propagation from segment 10 to 9, Figure 6 in Wang et al., 2018). Our results provide new insights. For example, up-dip migrations were predominant on the deep part of the tremor zone and down-dip migrations were principal on the shallow part (Figure 10d). In R1, up-dip migrations were predominant on the deep part of the tremor zone and tremor migrations tended to propagate southwestward (to R2). These differences in the characteristics of tremor migrations were attributed to the fact that Wang et al. (2018) could not investigate tremor migrations inside each segment.

4.2 Relationship between tremor migrations and heterogeneous distribution of fault strength on the plate interface

Previous studies have suggested that the spatial distribution of tremor energies reflects the heterogeneity in fault strength on the plate boundary (e.g., Kano et al., 2018a; Yabe & Ide, 2014). They also suggested that tremor patches with high radiated energies are related to the growth of along-strike migrations (Nakamoto et al., 2021; Yabe & Ide, 2014). Before the tremor patch with high energy was ruptured, tremors migrated from the tremor patch with low energy on the deep part of the tremor zone to that with high energy on the shallow part. When the tremor patch with high energy was broken, tremors migrated along the strike after the occurrence of burst activity (e.g., Shelly, 2010). The behavior of the tremor migrations was influenced by whether or not the tremor patch with high energy was broken. In the Kii Peninsula, the location of the high-energy tremor patch (Nakamoto et al., 2021; Yabe & Ide, 2014) corresponds to R2 in the present study. Up-dip migrations propagating into R2 were observed in R1 and R3 (Figures

10c and 10d). Moreover, in R2, along-strike migrations were predominant (Figure 10b) and tremor episodes tended to stop (Sagae et al., 2021). Our results suggest that the existence of a tremor patch with high energy controls the pattern of tremor migration before and after the tremor patch is broken.

RTRs have been observed to occur repeatedly in the same areas beneath the Kii Peninsula (Sagae et al., 2021). To discuss the relationship between the spatial distribution of RTRs and that of tremor patches, we systematically detected RTRs as follows: First, we searched for cells that contained starting points of tremor migrations with speeds of 10 km/hr or more. We then detected RTRs when the migration directions were opposite to the predominant direction inside the cells obtained in Figure 10c (the predominant direction of along-strike migration). Figures 12a and 12b show the spatial distribution of the RTRs during a tremor episode from August 11th to 16th, 2012, and a tremor episode from July 3rd to 14th, 2014, respectively. The white arrow shows the pattern of the main front, and the spatiotemporal evolutions of tremor migrations during those tremor episodes are shown in Figure 8 and Figure S12. The background colors show the median energy rates of the tremors (Yabe & Ide, 2014). The median energy rates were calculated in cells arranged at an interval of 0.05° along longitude and latitude, when the cells contained 100 or more tremor events that were located within 10 km.

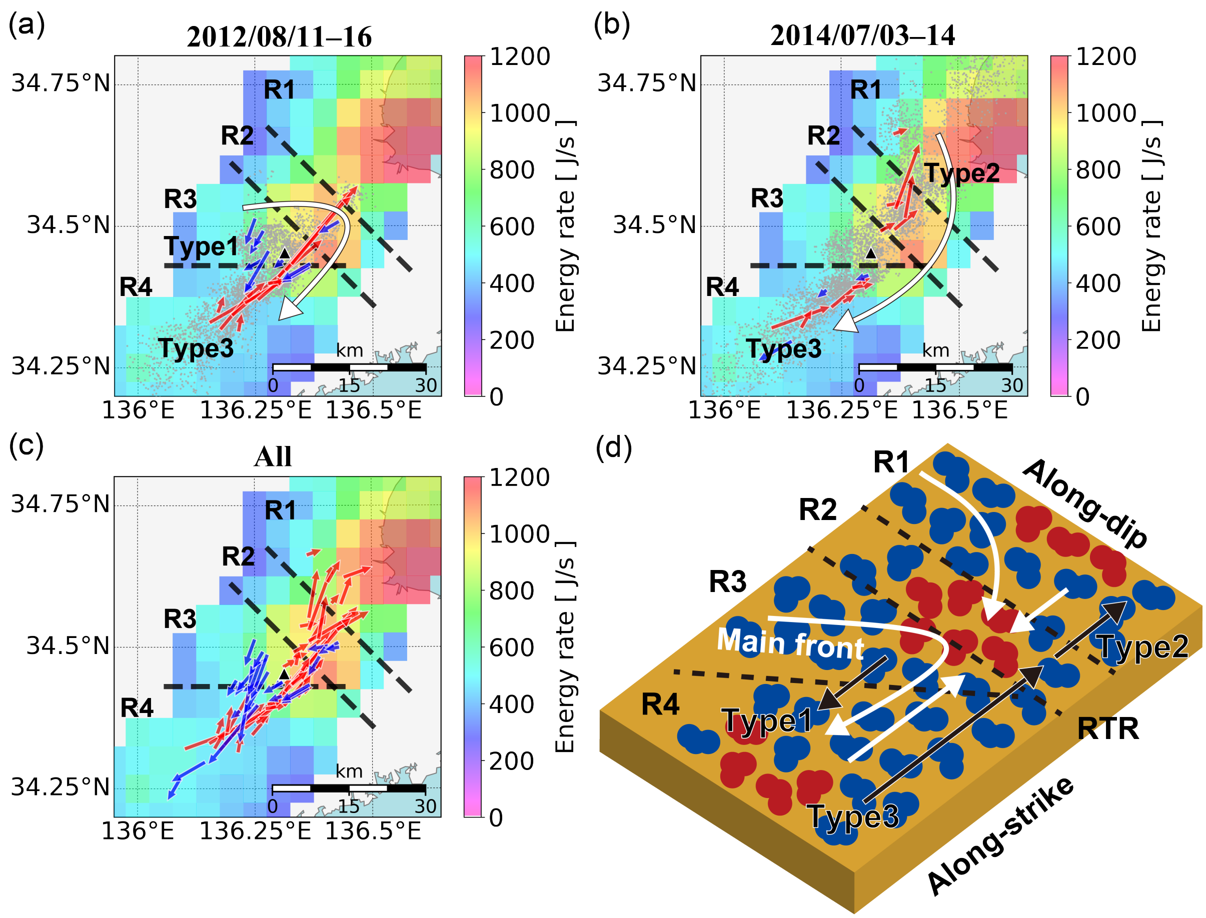

Figure 12. (**a**) Spatial distribution of RTRs during a tremor episode from August 11th to 16th, 2012. The red arrows show RTRs propagating northeastward, and the blue arrows show those propagating southwestward. The white arrow shows the pattern of the main front and the gray dots show tremor locations. The dashed lines and the black triangle are the same as those in Figure 10. The background colors show median energy rates (Yabe & Ide, 2014). (**b**) Same as (**a**), but for RTRs during a tremor episode from July 3rd to 14th, 2014. (**c**) Same as (**a**), but for all RTRs detected in the present study. (**d**) Schematic diagram of the distribution of tremor patches and tremor migrations beneath the Kii Peninsula. The red and blue dots show strong tremor patches with high energies and weak ones with low energies, respectively. The white arrows show the patterns of the main front. The black arrows (Type1–Type3) show the patterns of RTRs.

In Figures 12a and 12b, the three types of RTRs are presented. The first is the southwestward RTR that occurs near the southwest side of R2 (blue arrows shown by Type1 in

Figure 12a) when the main front propagates from the southwest side of R2 to the northeast. The second is the northeastward RTR that occurs near the northeast side of R2 (red arrows shown by Type2 in Figure 12b) when the main front propagates from the northeast side of R2 to the southwest. The third is the northeastward RTR that occurs near the southwest side of R4 (red arrows shown by Type3 in Figures 12a and 12b) when the main front propagates southwestward in R4. The third sometimes propagated from R4 to R2 (red arrows in Figure 12a). The three types of RTRs were found during other tremor episodes (Figure S14). Figure 12c shows all the RTRs detected in the present study. The spatial distribution of the RTRs appears to be a superposition of the three types of RTRs for the most part. Thus, our results suggest the existence of areas in which RTRs occur repeatedly. In addition, the median energy rates appear to be relatively high near areas where the three types of RTRs are found (R2 and the southwest side of R4). The occurrence of the three types of RTRs seems to depend on the directions from which the main front reaches the tremor patches. We show a schematic diagram of the spatial distribution of tremor migrations (Figure 12d) by summarizing the characteristics of areas R1–R4 discussed in Section 4.1 and those of RTRs in this section. Ando et al. (2012) explained the pattern of RTR based on a stress diffusion model. They interpreted RTR as a phenomenon in which weak patches with low energies that were reloaded or healed behind a front of stress diffusion were broken again when the front reached strong patches with high energies and the strong patches were ruptured. This interpretation of the RTR explains the distribution of tremor patches and the patterns of the RTRs in the present study (Figure 12). Thus, we consider that the patterns of the RTRs are controlled by the distribution of tremor patches with various frictional properties. Our results imply that the fine structures of tremor migrations and the distribution of tremor energies are key to investigating the frictional properties of the plate interface.

4.3 Relation between migration speed and duration

Diffusive tremor migrations, which are tremor migrations with their speeds decreasing with increasing durations (Obara et al. 2012), were often observed in the front of tremor activities during tremor episodes (e.g., Ando et al., 2012; Ide, 2010). We examined the relationship between migration speeds and durations based on our data set. Figure 13a shows histograms of the migration speeds versus duration. For the durations ranging from 10 min to 1 h (red), 1 h to 3 h (blue), 3 h to 6 h (green), and 6 h to 24 h (yellow), the most frequent values of migration speeds are 3 km/hr, 1.5 km/hr, 0.75 km/hr, and 0.5 km/hr, respectively. As Obara et al. (2012) reported, we also found that tremor migrations slowed down as the durations increased. We quantitatively investigated the relationship between migration speed and duration. Figure 13b shows the relationship between the migration speed (V_{mi}) and the duration (T). We found that the relation $V_{mi} \propto T^{-0.5}$ holds for tremor migrations. When we consider a diffusion process, the relation $V_{mi} = \frac{L}{T} = \sqrt{\frac{D}{T}}$ is derived based on the relation $L^2 = DT$, where L is the propagation distance, and D is the diffusion coefficient. Thus, our results quantitatively suggest that the growth of the tremor migrations is controlled by the diffusion process. Stress diffusion and pore-pressure diffusion are candidates for explaining the diffusion process (e.g., Ando et al., 2012; Cruz-Atienza et al., 2018; Farge et al., 2021). Understanding the physical mechanisms behind slow earthquakes will be the focus of our future work.

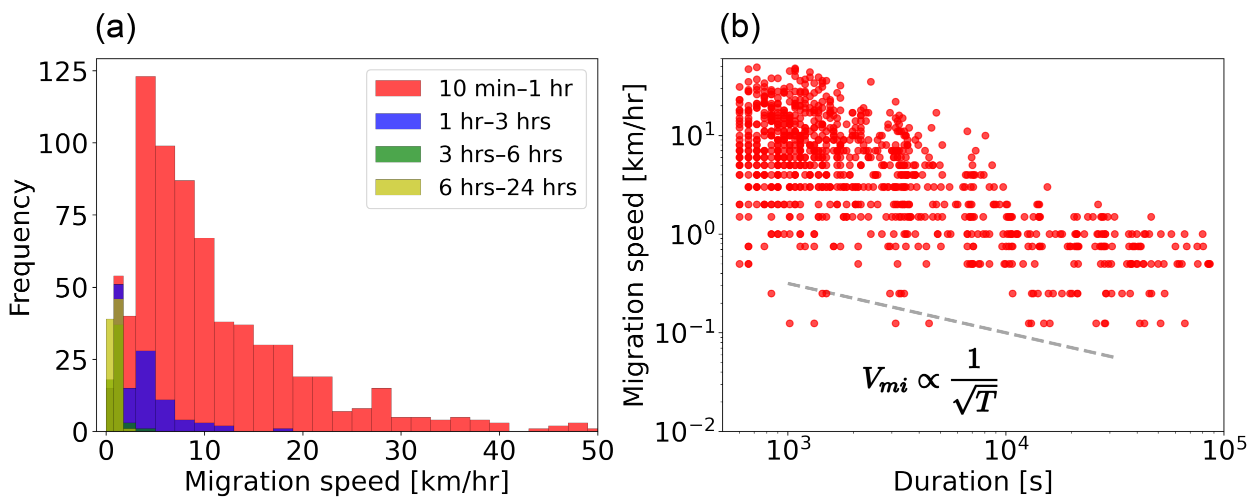

Figure 13. (**a**) The histograms of migration speeds in their respective durations. Red, blue, green, and yellow are the histogram of migration speeds for tremor migrations with durations ranging from 10 min to 1 h, 1 h to 3 h, 3 h to 6 h, and 6 h to 24 h, respectively. (**b**) The relationship between migration speed (V_{mi}) and duration (T). The gray dashed line shows the relation $V_{mi} \propto T^{-0.5}$.

5 Conclusions

The present study newly developed the space-time Hough transform to objectively extract tremor migrations. The advantage of this method is that multiple tremor migrations can be extracted regardless of the lengths of time windows and projected axes because a technique of "vote" enables us to distinguish the four parameters representing the tremor migration. The space-time Hough transform was applied to the data of tectonic tremors beneath the Kii Peninsula, Southwest Japan. Consequently, we succeeded in extracting 1,010 tremor migrations with durations ranging from 10 min to 24 h between July 2012 and July 2014.

Investigating the spatial distribution of tremor migrations, we found four areas (R1–R4) with the large number of tremor events composing tremor migrations. The followings are the characteristics of the tremor migrations in these areas: In areas R1 and R3, tremor migrations were predominant in the along-dip direction. In areas R2 and R4, tremor migrations were predominant in the along-strike direction. These patterns of tremor migrations represent the behavior of the main front because their spatial distribution of the median duration (6 h) and the median speed (1 km/hr) are consistent with the main front characteristics. We systematically detected RTRs based on the spatial characteristics of the main front, and the three types of RTRs with different patterns were found near R2 and R4. The patterns of tremor migrations (main front and RTR) are related to the distribution of tremor energies, suggesting that the distribution of tremor migrations reflects the fault strength on the plate interface. In addition, we investigated the relationship between migration speed and duration. Tremor migrations slowed down as the durations increased, and the relation $V_{mi} \propto T^{-0.5}$ held. This relationship suggests that a diffusion process controls the growth of tremor migrations.

The space-time Hough transform can objectively extract tremor migrations from any data in the tremor catalog worldwide if we set the parameters based on their tremor uncertainties and temporal resolution. The tremor migrations extracted using our method include information on their locations, timing, durations, migration directions, and migration speeds. Therefore, if we comprehensively extract tremor migrations by using the space-time Hough transform, their spatiotemporal characteristics will help understand the rupture process of slow earthquakes worldwide.

Acknowledgements

We thank Dr. Suguru Yabe for providing us with a catalog of tectonic tremors, including information on their energy rates (Yabe & Ide, 2014). We would like to thank Editage (www.editage.com) for English language editing.

Conflict of Interest

The authors declare that they have no known financial or non-financial completing interests.

Data Availability Statement

The catalog of tremor migrations in the present study is available from Data Set S1 in the Supporting Information. The tremor catalog of Yabe & Ide (2014) can be downloaded from 'Slow Earthquake Database' (Kano et al. 2018b; http://www-solid.eps.s.u-tokyo.ac.jp/~sloweq/), which is supported by the Japan Society for the Promotion of Science (JSPS) KAKENHI Grant Number JP16H06472 and JP21H05200.

References

Ando, R., Takeda, N., & Yamashita, T. (2012), Propagation dynamics of seismic and aseismic slip governed by fault heterogeneity and Newtonian rheology, *J. Geophys. Res.*, 117, B11308, doi:10.1029/2012JB009532.

Bletery, Q., A. M. Thomas, J. C. Hawthorne, R. M. Skarbek, A. W. Rempel, & R. D. Krogstad (2017), Characteristics of secondary slip fronts associated with slow earthquakes in Cascadia, *Earth and Planetary Science Letters, 463,* 212–220, https://doi.org/10.1016/j.epsl.2017.01.046.

Cruz-Atienza, V.M., Villafuerte, C., & Bhat, H.S. (2018), Rapid tremor migration and pore-pressure waves in subduction zones. *Nat Commun* **9,** 2900, https://doi.org/10.1038/s41467-018-05150-3

Farge, G., Jaupart, C., & Shapiro, N. M. (2021). Episodicity and migration of low frequency earthquakes modeled with fast fluid pressure transients in the permeable subduction interface. *Journal of Geophysical Research: Solid Earth*, 126, e2021JB021894. https://doi.org/10.1029/2021JB021894

Ghosh, A., Vidale, J. E., Sweet, J. R., Creager, K. C., Wech, A. G., Houston, H., & Brodsky, E. E. (2010), Rapid, continuous streaking of tremor in Cascadia, *Geochem. Geophys. Geosyst.*, 11, Q12010, doi:10.1029/2010GC003305.

Ghosh, A., Vidale, J. E., & Creager, K. C. (2012), Tremor asperities in the transition zone control evolution of slow earthquakes, *J. Geophys. Res.*, 117, B10301, doi:10.1029/2012JB009249.

Hirose, F., Nakajima, J., & Hasegawa, A. (2008), Three-dimensional seismic velocity structure and configuration of the Philippine Sea slab in southwestern Japan estimated by double-difference tomography, *J. Geophys. Res.*, 113, B09315, doi:10.1029/2007JB005274.

Hirose, H., & Obara, K. (2010), Recurrence behavior of short-term slow slip and correlated nonvolcanic tremor episodes in western Shikoku, southwest Japan, *J. Geophys. Res.*, 115, B00A21, doi:10.1029/2008JB006050.

Hough, P. V. C. (1962), Method and means for recognizing complex patterns, *U.S. Patent, no.3069654.*

Houston, H., Delbridge, B., Wech, A., & Creager, K. (2011), Rapid tremor reversals in Cascadia generated by a weakened plate interface. *Nature Geosci* **4**, 404–409, https://doi.org/10.1038/ngeo1157

Ide, S. (2010), Striations, duration, migration and tidal response in deep tremor. *Nature* **466,** 356–359, https://doi.org/10.1038/nature09251

Imanishi, K., Takeda, N., Kuwahara, Y., & Koizumi, N. (2011), Enhanced detection capability of non-volcanic tremor using a 3-level vertical seismic array network, VA-net, in southwest Japan, *Geophys. Res. Lett.*, 38, L20305, doi:10.1029/2011GL049071.

Ito, Y., Hino, R., Kido, M., Fujimoto, H., Osada, Y., Inazu, D., Ohta Y., Iinuma, T., Ohzono, M., Miura, S., Mishina, M., Suzuki, K., Tsuji, T., & Ashi, J. (2013). Episodic slow slip events in the Japan subduction zone before the 2011 Tohoku-Oki earthquake. *Tectonophysics*, **600**(Suppl C), 14–26. https://doi.org/10.1016/j.tecto.2012.08.022

Kano, M., Kato, A., Ando, R., & Obara, K. (2018a), Strength of tremor patches along deep transition zone of a megathrust. *Sci Rep* **8,** 3655, https://doi.org/10.1038/s41598-018-22048-8

Kano, M., N. Aso, T. Matsuzawa, S. Ide, S. Annoura, R. Arai, S. Baba, M. Bostock, K. Chao, K.

Heki, S. Itaba, Y. Ito, N. Kamaya, T. Maeda, J. Maury, M. Nakamura, T. Nishimura, K. Obana, K. Ohta, N. Poiata, B. Rousset, H. Sugioka, R. Takagi, T. Takahashi, A. Takeo, Y. Tu, N. Uchida, Y. Yamashita, and K. Obara (2018b), Development of a Slow Earthquake Database, *Seismological Research Letters*, 89 (4), 1566–1575, doi:10.1785/0220180021.

Kato, A., Obara, K., Igarashi, T., Tsuruoka, H., Nakagawa, S., & Hirata, N. (2012). Propagation of slow slip leading up to the 2011 Mw 9.0 Tohoku-Oki Earthquake. *Science*, **335**(6069), 705–708. https://doi.org/10.1126/science.1215141

Morii, M. (2019), Detection of astronomical moving objects using Hough transformation, Poster Presentation, Open House of The Institute of Statistical Mathematics on Jun 5, 2019 (written in Japanese), http://hdl.handle.net/10787/00033907

Nakamoto, K., Hiramatsu, Y., Uchide, T, & Imanishi, K. (2021), Cascading rupture of patches of high seismic energy release controls the growth process of episodic tremor and slip events. *Earth Planets Space* **73**, 59, https://doi.org/10.1186/s40623-021-01384-6

Obara, K. (2002), Nonvolcanic deep tremor associated with subduction in Southwest Japan, *Science, 296* (5573), 1679–1681, doi:10.1126/science.1070378.

Obara, K. (2010), Phenomenology of deep slow earthquake family in southwest Japan: Spatiotemporal characteristics and segmentation, *J. Geophys. Res.*, 115, B00A25, doi:10.1029/2008JB006048.

Obara, K., & Kato, A. (2016), Connecting slow earthquakes to huge earthquakes, *Science*, 353 (6296), 253–257, doi:10.1126/science.aaf1512.

Obara, K., Matsuzawa, T., Tanaka, S., & Maeda, T. (2012), Depth-dependent mode of tremor migration beneath Kii Peninsula, Nankai subduction zone, *Geophys. Res. Lett.*, 39, L10308, doi:10.1029/2012GL051420.

Ouillon, G., Ducorbier, C., & Sornette, D. (2008), Automatic reconstruction of fault networks from seismicity catalogs: Three-dimensional optimal anisotropic dynamic clustering, *J. Geophys. Res.*, 113, B01306, doi:10.1029/2007JB005032.

Radiguet, M., Perfettini, H., Cotte, N., Gualandi, A, Valette B., Kostoglodov V., Lhomme T., Walpersdorf A., Cabral Cano E., & Campillo, M. (2016), Triggering of the 2014 M_w7.3 Papanoa earthquake by a slow slip event in Guerrero, Mexico. *Nature Geosci* **9,** 829–833, https://doi.org/10.1038/ngeo2817

Rogers, G., & Dragert, H. (2003), Episodic tremor and slip on the cascadia subduction zone: The chatter of silent slip, *Science*, 300 (5627), 1942–1943, doi:10.1126/science.1084783.

Sagae, K., Nakahara, H., Nishimura, T., & Imanishi, K. (2021), High resolution location of deep low-frequency tremors beneath the Kii Peninsula, Nankai subduction zone, Japan, using data from a dense seismic array, *Geophysical Journal International*, 225 (2), 775–788, doi:10.1093/gji/ggab004.

Schwartz, S. Y., & Rokosky, J. M. (2007), Slow slip events and seismic tremor at circum-Pacific subduction zones, *Rev. Geophys.*, 45, RG3004, doi:10.1029/2006RG000208.

Shelly, D. (2010), Migrating tremors illuminate complex deformation beneath the seismogenic San Andreas fault. *Nature* **463,** 648–652, https://doi.org/10.1038/nature08755.

Shelly, D., Beroza, G., Ide, S., & Nakamula, S. (2006), Low-frequency earthquakes in Shikoku, Japan, and their relationship to episodic tremor and slip. *Nature* 442, 188–191, https://doi.org/10.1038/nature04931

Shelly, D. R., Beroza, G. C., & Ide, S. (2007), Complex evolution of transient slip derived from precise tremor locations in western Shikoku, Japan, *Geochem. Geophys. Geosyst*., 8, Q10014, doi:10.1029/2007GC001640.

Socquet, A., Valdes, J. P., Jara, J., Cotton, F., Walpersdorf, A., Cotte, N., Specht, S., Ortega-Culaciati, F., Carrizo, D., & Norabuena, E. (2017), An 8 month slow slip event triggers progressive nucleation of the 2014 Chile megathrust, *Geophys. Res. Lett.*, 44, 4046– 4053, doi:10.1002/2017GL073023.

Takemura, S., Noda, A., Kubota, T., Asano, Y., Matsuzawa, T., & Shiomi, K. (2019). Migrations and Clusters of Shallow Very Low Frequency Earthquakes in the Regions Surrounding Shear Stress Accumulation Peaks Along the Nankai Trough. *Geophysical Research Letters*, 46, 11830– 11840. https://doi.org/10.1029/2019GL084666

Wang, T., Zhuang, J., Buckby, J., Obara, K., & Tsuruoka, H. (2018). Identifying the recurrence patterns of nonvolcanic tremors using a 2-D hidden Markov model with extra zeros. *Journal of Geophysical Research: Solid Earth*, 123, 6802– 6825. https://doi.org/10.1029/2017JB015360

Yabe, S., & Ide, S. (2014), Spatial distribution of seismic energy rate of tectonic tremors in subduction zones, *J. Geophys. Res. Solid Earth*, 119, 8171– 8185, doi:10.1002/2014JB011383.

[Journal of Geophysical Research: Solid Earth]

Supporting Information for

Fine structure of tremor migrations beneath the Kii Peninsula, Southwest Japan, extracted with a space-time Hough transform

Kodai Sagae[1,2]*, Hisashi Nakahara[1], Takeshi Nishimura[1], and Kazutoshi Imanishi[3]

[1]Department of Geophysics, Graduate School of Science, Tohoku University, 6-3, Aramaki Aza-Aoba, Aoba-ku, Sendai, Miyagi, 980-8578, Japan.

[2]Now at Geological Survey of Japan, National Institute of Advanced Industrial Science and Technology (AIST), Tsukuba Central 7, 1-1-1 Higashi, Tsukuba, Ibaraki, 305-8567, Japan.

[3]Geological Survey of Japan, National Institute of Advanced Industrial Science and Technology (AIST), Tsukuba Central 7, 1-1-1 Higashi, Tsukuba, Ibaraki, 305-8567, Japan.

Contents of this file

Text S1
Figures S1 to S14

Additional Supporting Information (Files uploaded separately)

Captions for Data Set S1

Introduction

This supplement contains the followings. The derivation of a space-time Hough transform (Equation 1) in the main text is detailed in Text S1. Figures S2–S12 show tremor migrations extracted in all tremor episodes from July 2012 to July 2014. Figure S13 shows spatial patterns of tremor migrations with high speeds (10 km/hr or more). Figure S14 shows spatial distribution of RTRs during tremor episodes. Data Set S1 is the catalog of tremor migrations extracted in the present study.

Text S1. Derivation of space-time Hough transform

This section explains the derivation of Equation 1 in the main text. We consider (x, y, t) as a coordinate of a tremor event, where x is the longitude (the east is positive), y is the latitude (the north is positive), and t is the detection time. We want to express a tremor migration as a straight line in a (2+1)-D space-time (2-D in space and 1-D in time). In addition, information on uncertainties of tremor locations is taken into account by giving spatial spread to the straight line (by considering a cylinder). We use tyt-Euler angle to represent an arbitrary position of the cylinder in the (2+1)-D space-time. The tyt-Euler angle is rotations of coordinate system in the following order (Figures S1a–1c), rotating the system (x, y, t) around the t-axis by ϕ, rotating the system $(x^{(1)}, y^{(1)}, t)$ around the rotated y-axis ($y^{(1)}$-axis) by θ, and then rotating the system $(x^{(2)}, y^{(1)}, t^{(1)})$ around the rotated t-axis ($t^{(1)}$-axis) by ψ. Here, θ is the zenith angle, ϕ is the azimuth, and ψ is the rotation angle. We consider standard unit vectors in ordinal coordinate system as $\overrightarrow{e_x}$, $\overrightarrow{e_y}$ and $\overrightarrow{e_t}$. As shown in Figure S1a, standard unit vectors in the rotated coordinate system ($x^{(1)}, y^{(1)},$ and t) around the t-axis by ϕ are represented as:

$$\begin{aligned} \overrightarrow{e_x^{(1)}} &= \cos\phi\,\overrightarrow{e_x} + \sin\phi\,\overrightarrow{e_y} \\ \overrightarrow{e_y^{(1)}} &= -\sin\phi\,\overrightarrow{e_x} + \cos\phi\,\overrightarrow{e_y} \\ &\overrightarrow{e_t}\,, \end{aligned} \tag{S1}$$

where $\overrightarrow{e_x^{(1)}}$, and $\overrightarrow{e_y^{(1)}}$ are standard unit vectors after the rotation by ϕ. Next, as shown in Figure S1b, standard unit vectors in the rotated coordinate system ($x^{(2)}, y^{(1)},$ and $t^{(1)}$) around the rotated y-axis ($y^{(1)}$-axis) by θ are represented as:

$$\begin{aligned} \overrightarrow{e_x^{(2)}} &= \cos\theta\,\overrightarrow{e_x^{(1)}} - \sin\theta\,\overrightarrow{e_t} \\ &\overrightarrow{e_y^{(1)}} \\ \overrightarrow{e_t^{(1)}} &= \sin\theta\,\overrightarrow{e_x^{(1)}} + \cos\theta\,\overrightarrow{e_t}\,, \end{aligned} \tag{S2}$$

where $\overrightarrow{e_x^{(2)}}$ and $\overrightarrow{e_t^{(1)}}$ are standard unit vectors after the rotation by θ. Notably, the vectors of $\overrightarrow{e_x^{(2)}}$, $\overrightarrow{e_y^{(1)}}$, and $\overrightarrow{e_t^{(1)}}$ are consistent with standard unit vectors in the polar coordinate system ($\overrightarrow{e_\theta}, \overrightarrow{e_\phi}, \overrightarrow{e_r}$), where $\overrightarrow{e_\theta} = (\cos\theta\cos\phi\,, \cos\theta\sin\phi\,, -\sin\theta)^T$, $\overrightarrow{e_\phi} = (-\sin\phi\,, \cos\phi, 0)^T$, and $\overrightarrow{e_r} = (\sin\theta\cos\phi, \sin\theta\sin\phi\,, \cos\theta)^T$. Finally, as shown in Figure S1c, standard unit vectors in the rotated coordinate system ($x^{(3)}, y^{(2)}$, and $t^{(1)}$) around the rotated t-axis ($t^{(1)}$-axis) by ψ are represented as:

$$\begin{gathered}\overrightarrow{e_x^{(3)}} = \cos\psi\,\overrightarrow{e_x^{(2)}} + \sin\psi\,\overrightarrow{e_y^{(1)}} \\ \overrightarrow{e_y^{(2)}} = -\sin\psi\,\overrightarrow{e_x^{(2)}} + \cos\psi\,\overrightarrow{e_y^{(1)}} \\ \overrightarrow{e_t^{(1)}},\end{gathered} \tag{S3}$$

where $\overrightarrow{e_x^{(3)}}$ and $\overrightarrow{e_y^{(2)}}$ are standard unit vectors after the rotation by ψ. Summarizing Equations from S1 to S3,

$$\begin{gathered}\overrightarrow{e_x^{(3)}} = \begin{pmatrix}-\sin\phi\sin\psi + \cos\theta\cos\phi\cos\psi \\ \cos\phi\sin\psi + \cos\theta\sin\phi\cos\psi \\ -\sin\theta\cos\psi\end{pmatrix} \\ \overrightarrow{e_y^{(2)}} = \begin{pmatrix}-\sin\phi\cos\psi - \cos\theta\cos\phi\sin\psi \\ \cos\phi\cos\psi - \cos\theta\sin\phi\sin\psi \\ \sin\theta\sin\psi\end{pmatrix} \\ \overrightarrow{e_t^{(1)}} = \begin{pmatrix}\sin\theta\cos\phi \\ \sin\theta\sin\phi \\ \cos\theta\end{pmatrix}.\end{gathered} \tag{S4}$$

The rotation matrix of the tyt-Euler angle is represented as:

$$R(\theta,\phi,\psi) = (\overrightarrow{e_x^{(3)}}\,\overrightarrow{e_y^{(2)}}\,\overrightarrow{e_t^{(1)}}) = (\vec{\alpha}\,\vec{\beta}\,\vec{\gamma}) = \\ \begin{pmatrix}-\sin\phi\sin\psi + \cos\theta\cos\phi\cos\psi & -\sin\phi\cos\psi - \cos\theta\cos\phi\sin\psi & \sin\theta\cos\phi \\ \cos\phi\sin\psi + \cos\theta\sin\phi\cos\psi & \cos\phi\cos\psi - \cos\theta\sin\phi\sin\psi & \sin\theta\sin\phi \\ -\sin\theta\cos\psi & \sin\theta\sin\psi & \cos\theta\end{pmatrix}, \tag{S5}$$

where $R(\theta, \phi, \psi)$ is the rotation matrix of the tyt-Euler angle, $\vec{\alpha}$, $\vec{\beta}$, and $\vec{\gamma}$ are unit vectors of Equation 2 in the main text. If θ is equal to zero, the rotations of coordinate system by ϕ and ψ are operations around the same axis (t-axis). There is no problem in the present study because migration speed (=tan θ) is always larger than zero and the range of θ is $0° < \theta < 90°$.

We consider a cylinder whose cylindrical axis is located at (ρ, 0, 0) and its radius is r, where ρ is the distance from an origin to the cylindrical axis. The equation of the cylinder is represented as:

$$\begin{pmatrix} x \\ y \\ t \end{pmatrix} = \begin{pmatrix} \rho + r\cos\lambda \\ r\sin\lambda \\ m \end{pmatrix}, \tag{S6}$$

where λ and m are parameters related to the angle around the t-axis measured counterclockwise from the x-axis and the direction of the straight line (direction of cylindrical axis), respectively. An arbitrary position of the cylinder in the (2+1)-D space-time is represented by rotating Equation S6 using Equation S5:

$$\begin{pmatrix} x \\ y \\ t \end{pmatrix} = R(\theta, \phi, \psi) \begin{pmatrix} \rho + r\cos\lambda \\ r\sin\lambda \\ m \end{pmatrix} = (\rho + r\cos\lambda)\,\vec{\alpha} + (r\sin\lambda)\,\vec{\beta} + m\,\vec{\gamma}\,. \tag{S7}$$

Equation 1 in the main text is derived by calculating Equation S7.

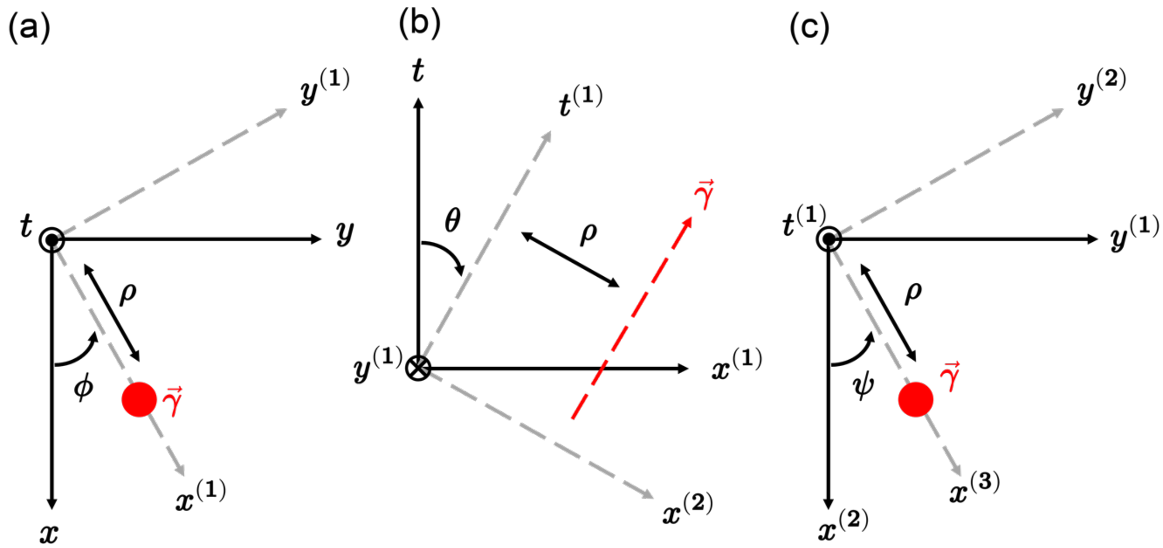

Figure S1. Schematic diagrams of tyt-Euler angle. (**a**) Rotation of coordinate system (x, y, t) around the t-axis by ϕ. (**b**) Rotation of the system ($x^{(1)}$, $y^{(1)}$, t) around the rotated y-axis ($y^{(1)}$-axis) by θ. (**c**) Rotation of the system ($x^{(2)}$, $y^{(1)}$, $t^{(1)}$) around the rotated t-axis ($t^{(1)}$-axis) by ψ. The red dots and arrow show locations of the unit direction vector (cylindrical axis) in rotation processes of the coordinate system.

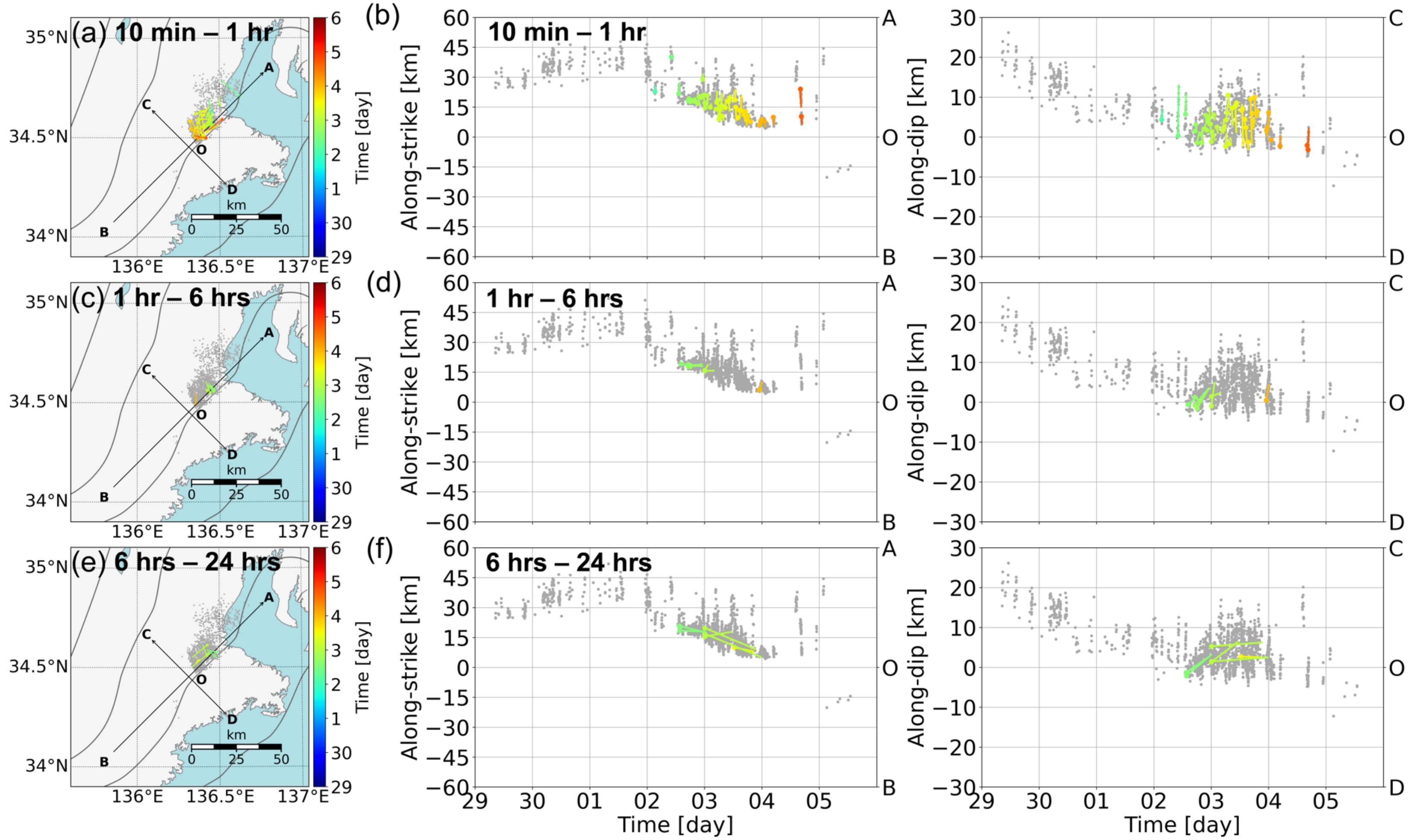

Figure S2. Tremor migrations during a tremor episode from September 29th to October 5th, 2012. (**a**) Map view of the tremor migrations with durations ranging from 10 min to 1 h. The gray dots show locations of tremors. Colored lines and dots show tremor migrations and their starting points, and the colors show the starting time of tremor migrations. (**b**) Spatiotemporal plots of the tremor migrations with the same durations as that of (**a**). The left panel shows spatiotemporal evolutions of tremor migrations along the strike (A–B) and the right panel shows spatiotemporal evolutions of ones along the dip (C–D). (**c**), (**d**) Same as (**a**) and (**b**), but for tremor migrations with durations ranging from 1 h to 6 h. (**e**), (**f**) Same as (**a**) and (**b**), but for tremor migrations with durations ranging from 6 h to 24 h.

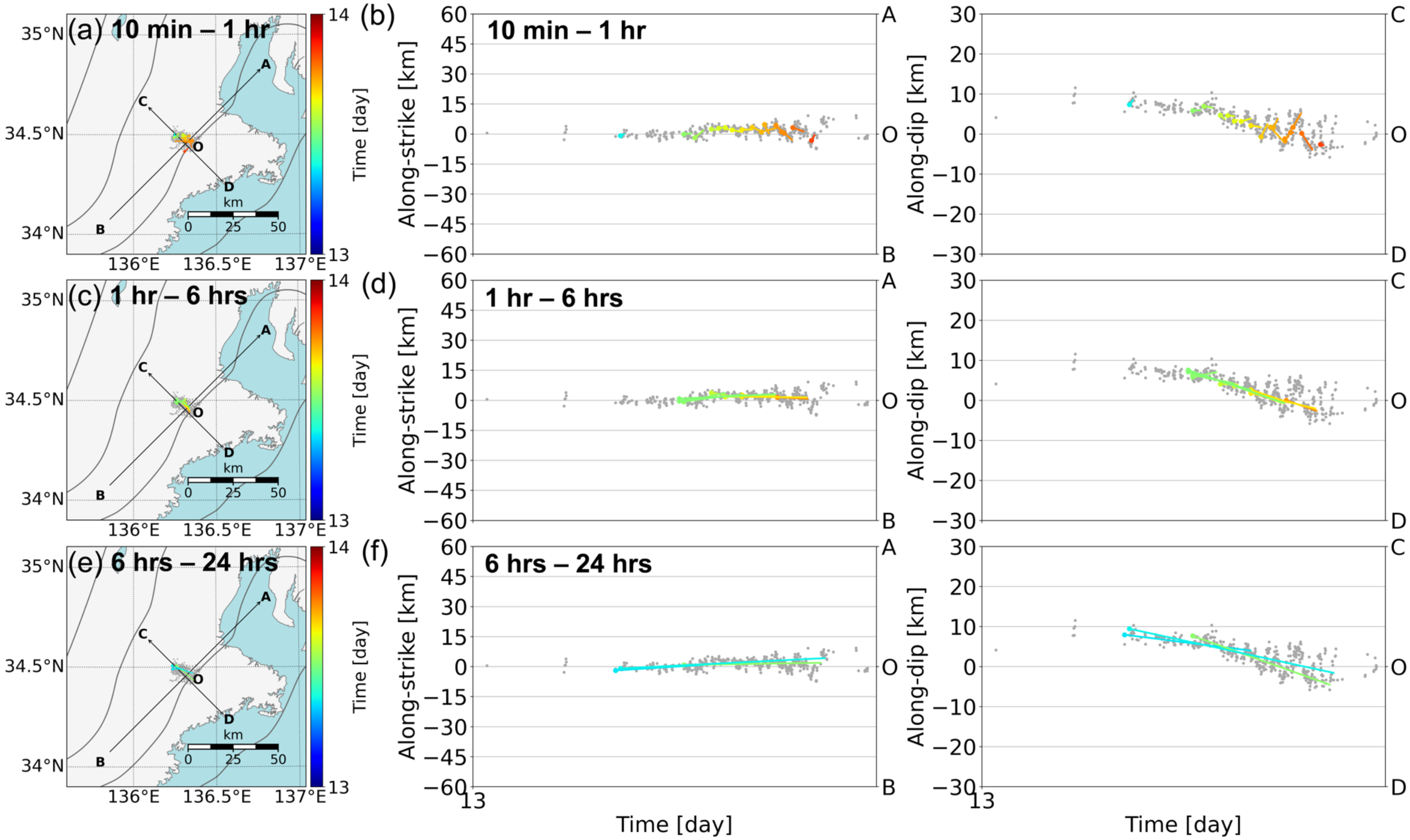

Figure S3. Same as Figure S2, but for tremor episode on December 13th, 2012.

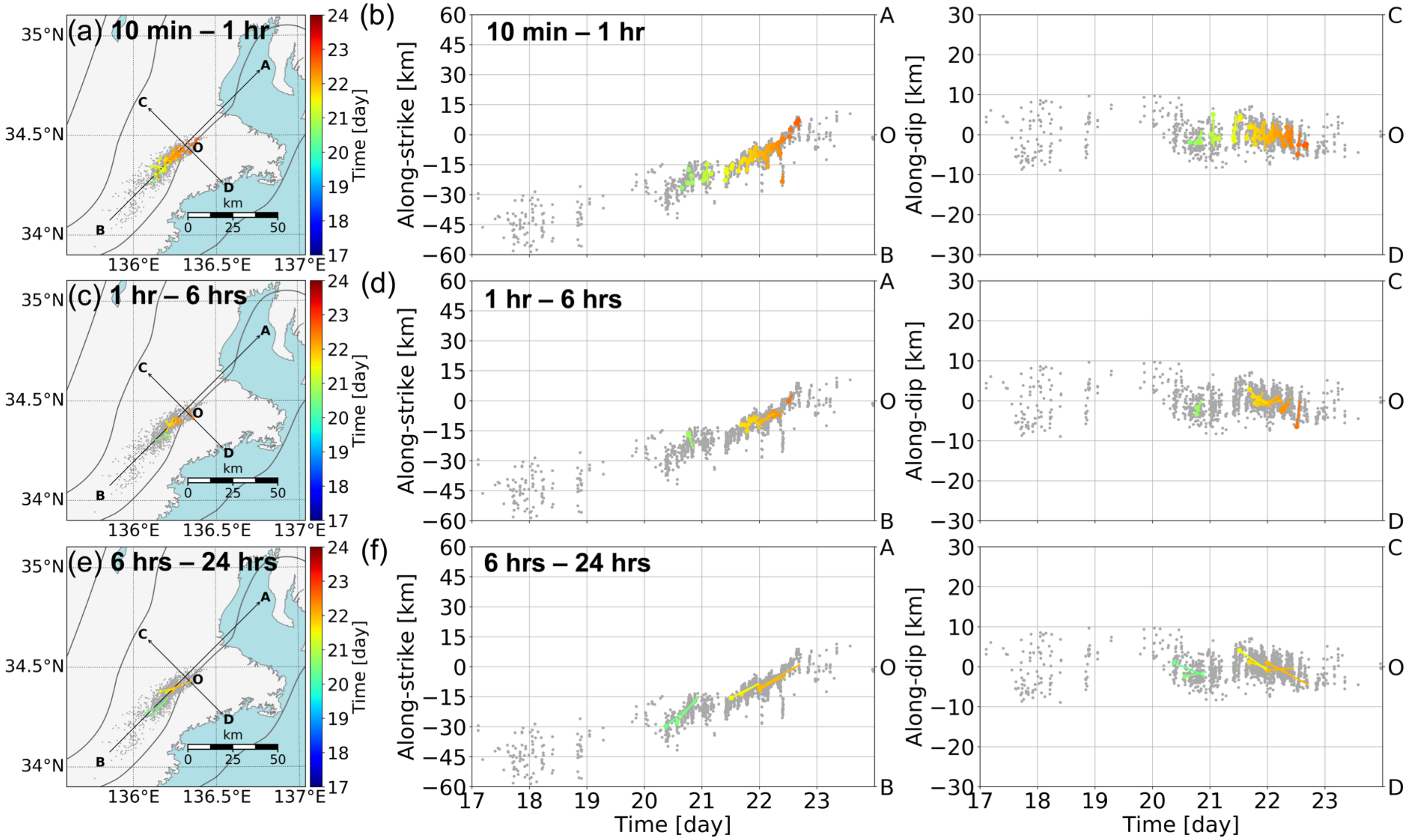

Figure S4. Same as Figure S2, but for tremor episode from December 17th to 23rd, 2012.

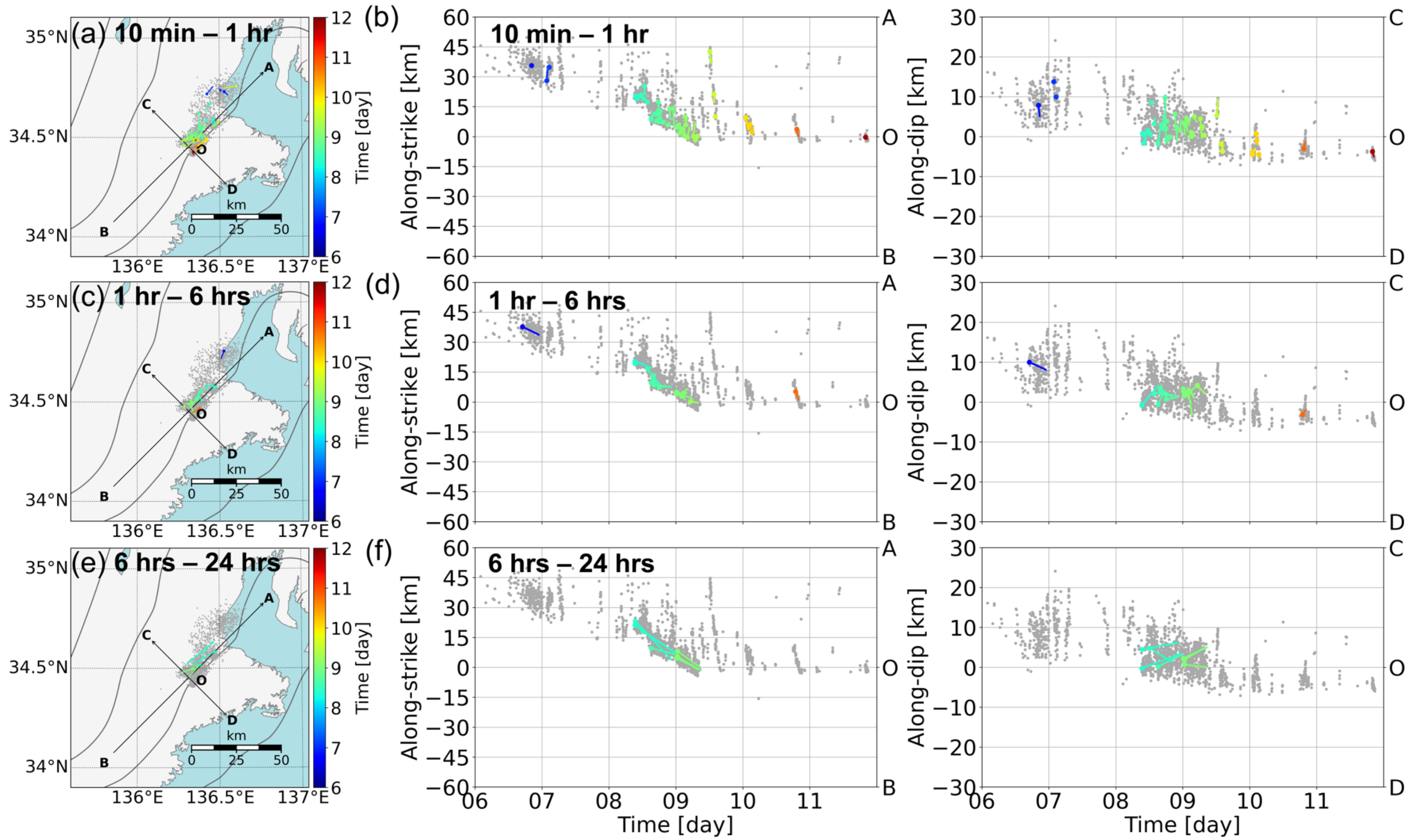

Figure S5. Same as Figure S2, but for tremor episode from April 6th to 11th, 2013.

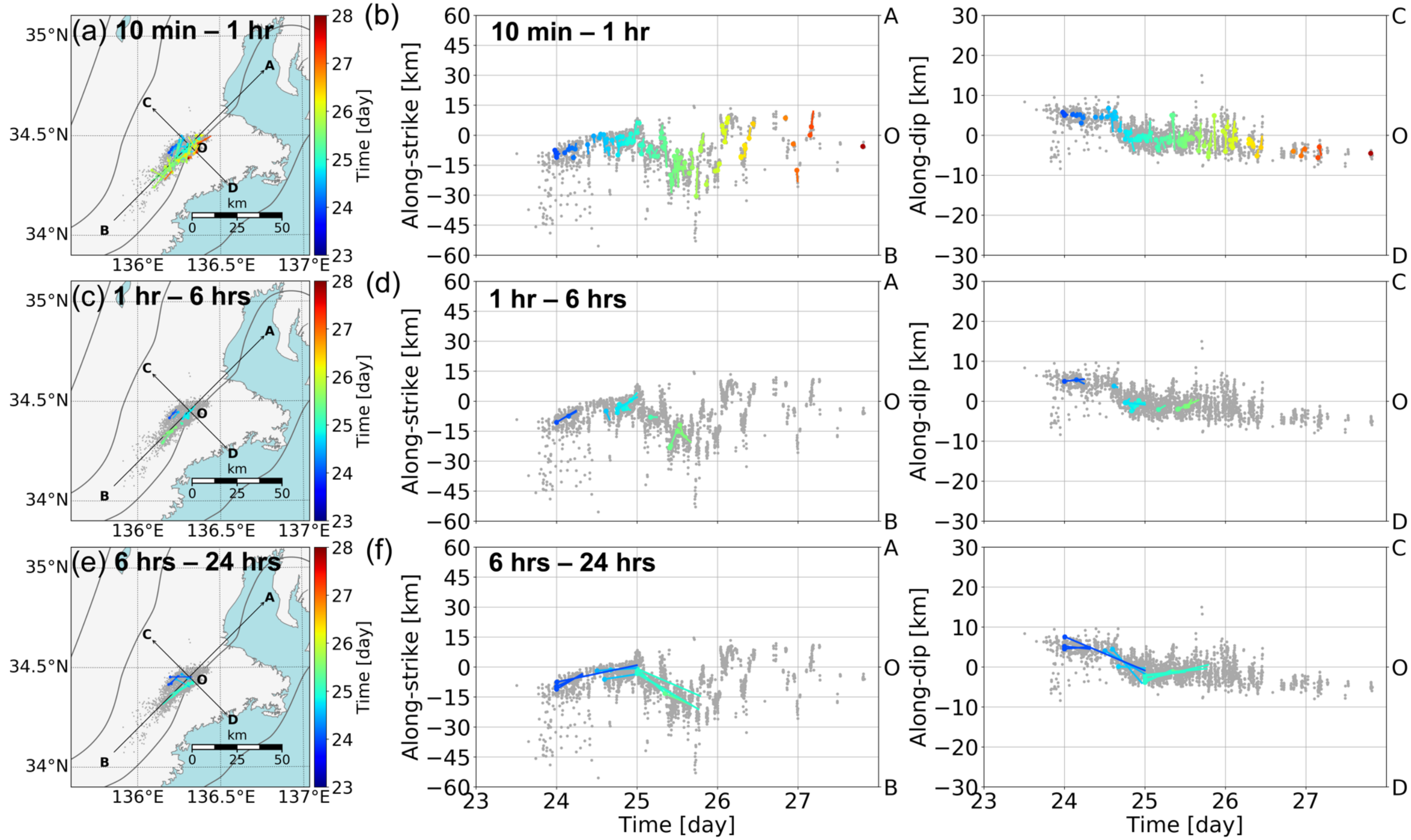

Figure S6. Same as Figure S2, but for tremor episode from July 23rd to 27th, 2013.

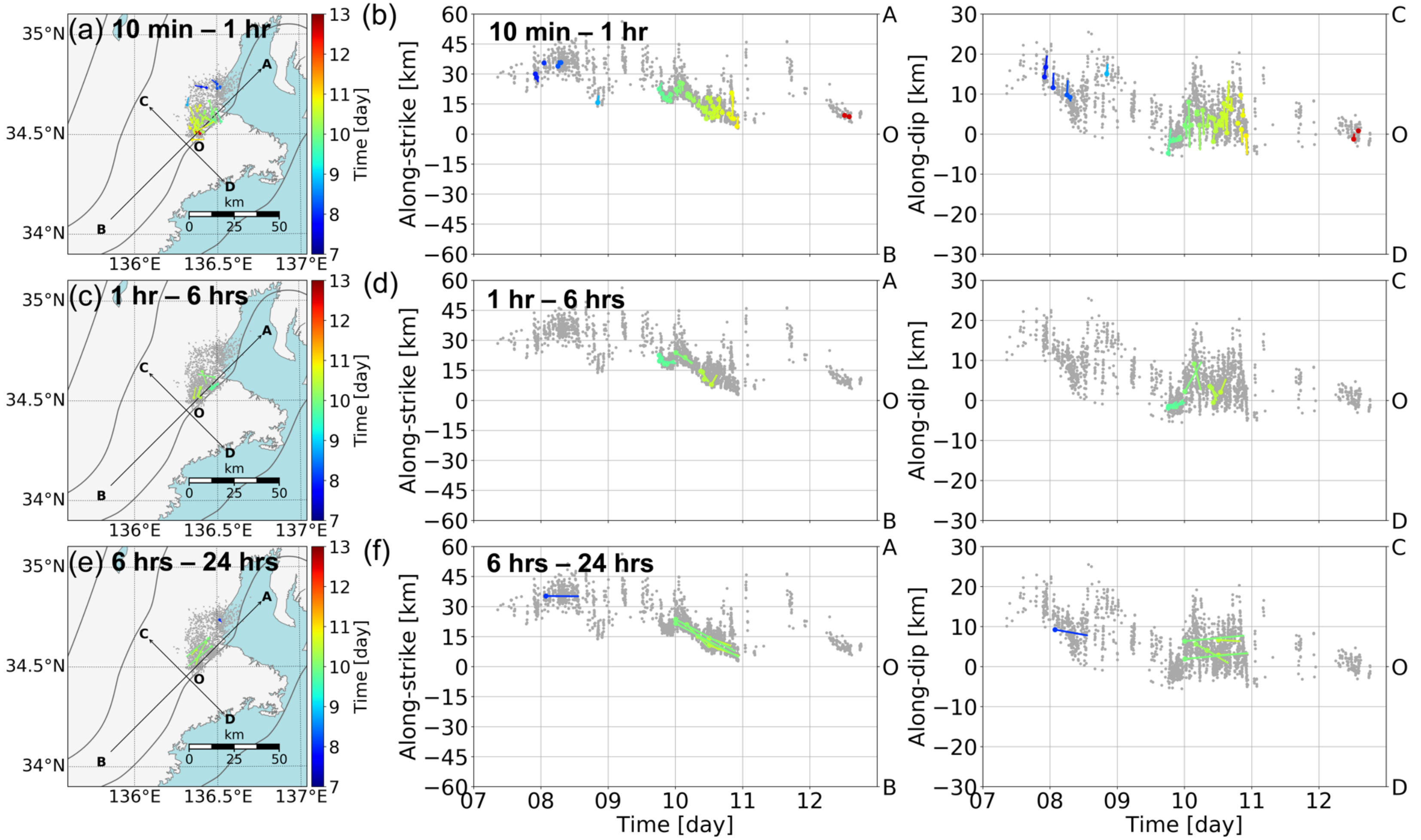

Figure S7. Same as Figure S2, but for tremor episode from September 7th to 12th, 2013.

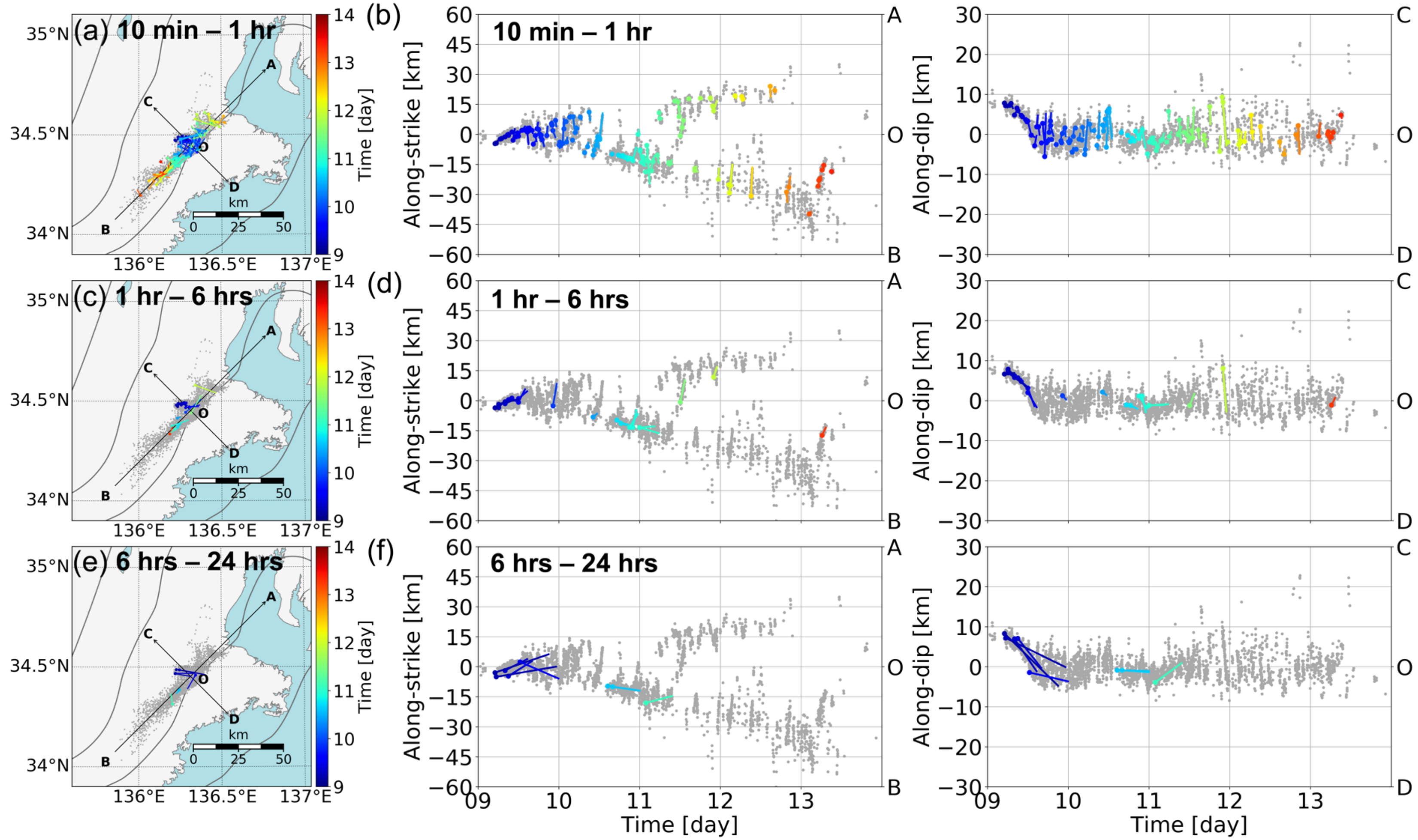

Figure S8. Same as Figure S2, but for tremor episode from January 9th to 13th, 2014.

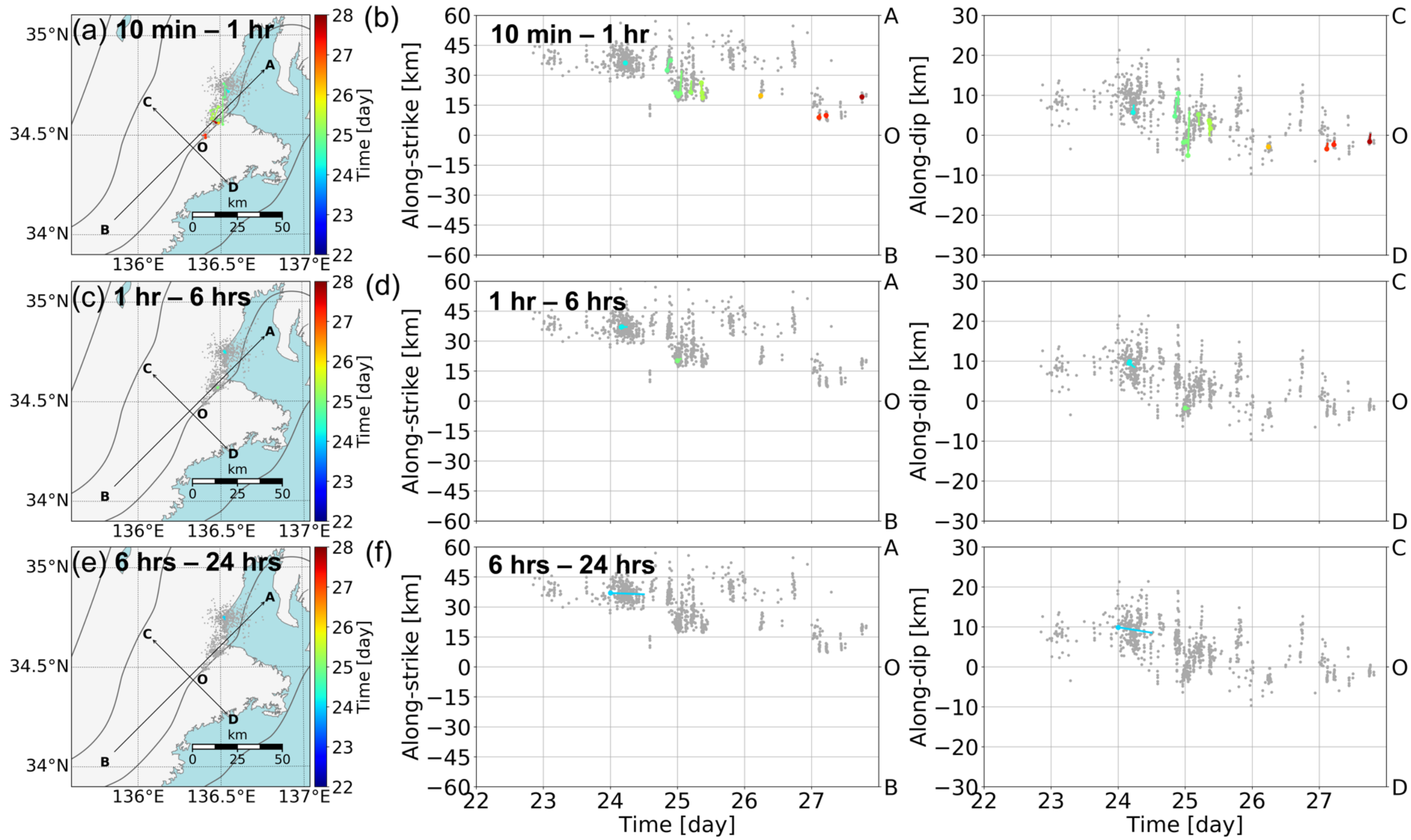

Figure S9. Same as Figure S2, but for tremor episode from January 22nd to 27th, 2014.

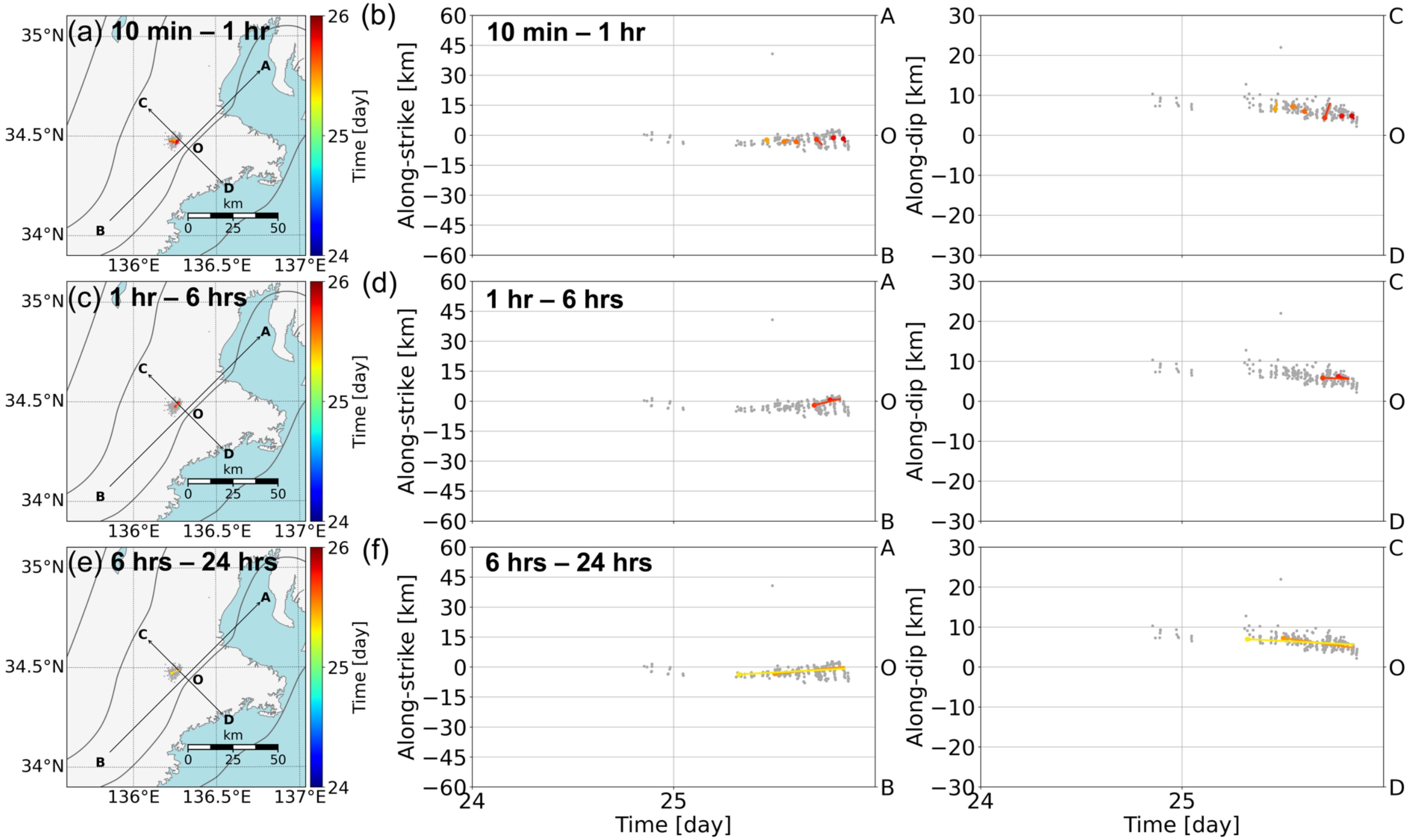

Figure S10. Same as Figure S2, but for tremor episode from April 24th to 25th, 2014.

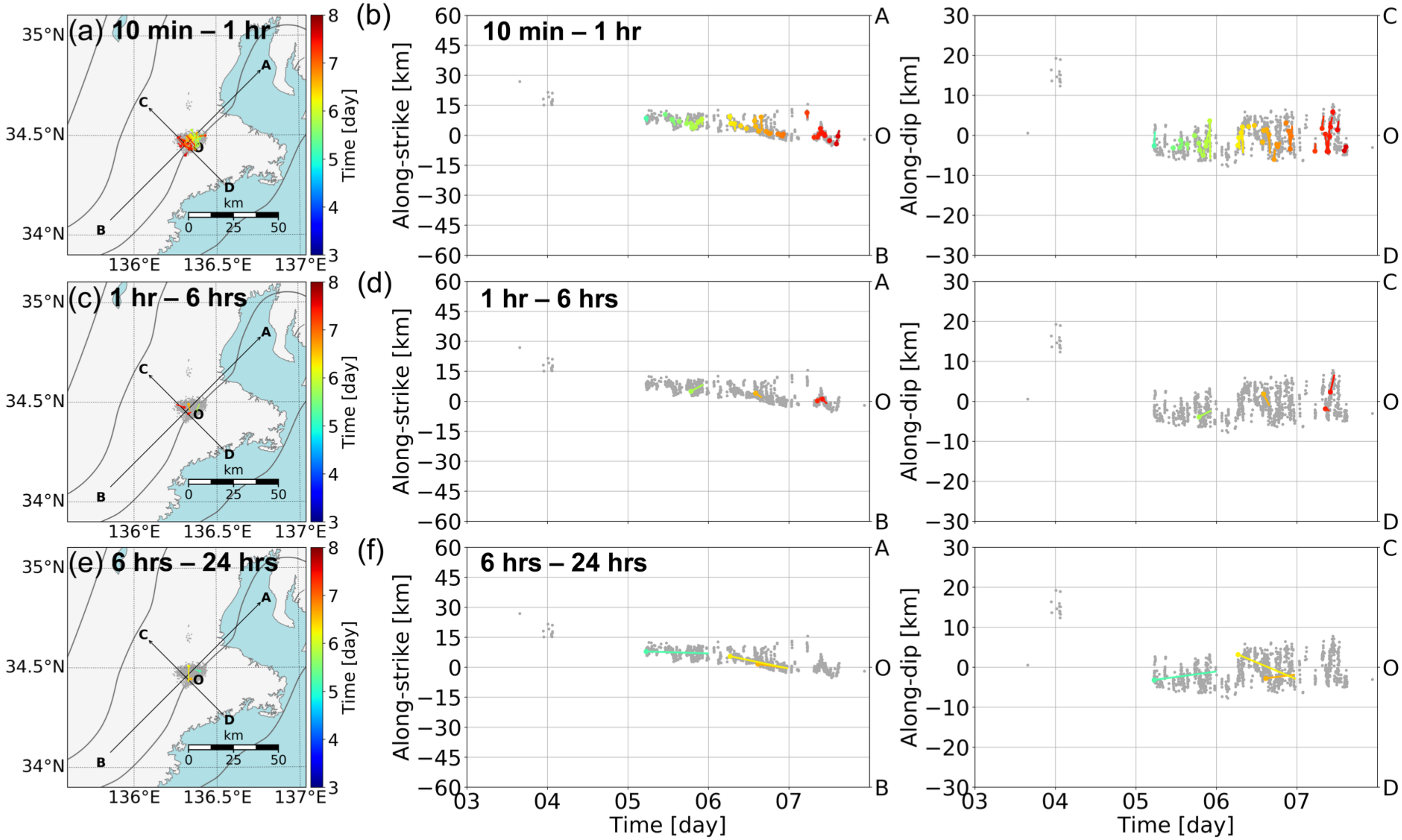

Figure S11. Same as Figure S2, but for tremor episode from May 3rd to 7th, 2014.

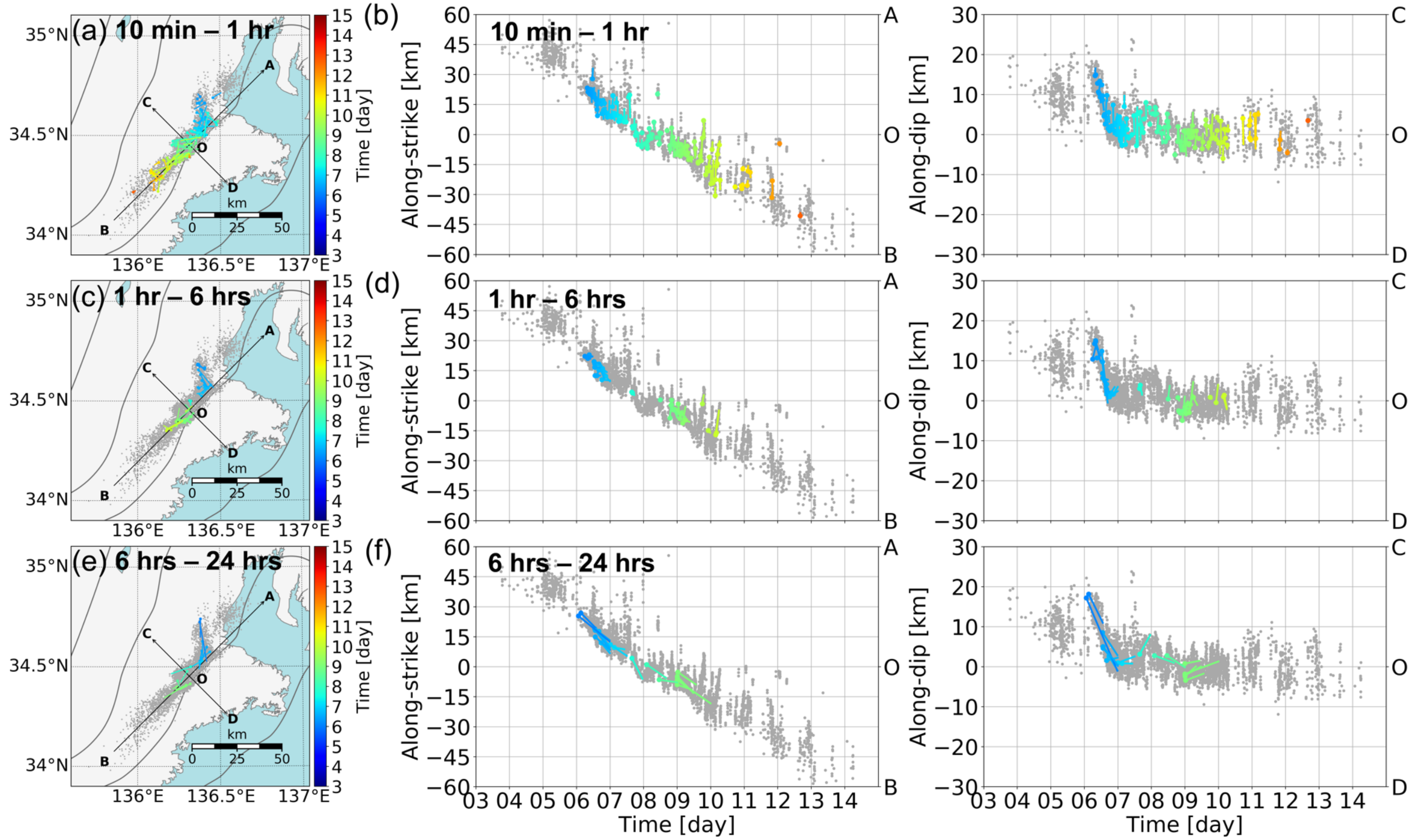

Figure S12. Same as Figure S2, but for tremor episode from July 3rd to 14th, 2014.

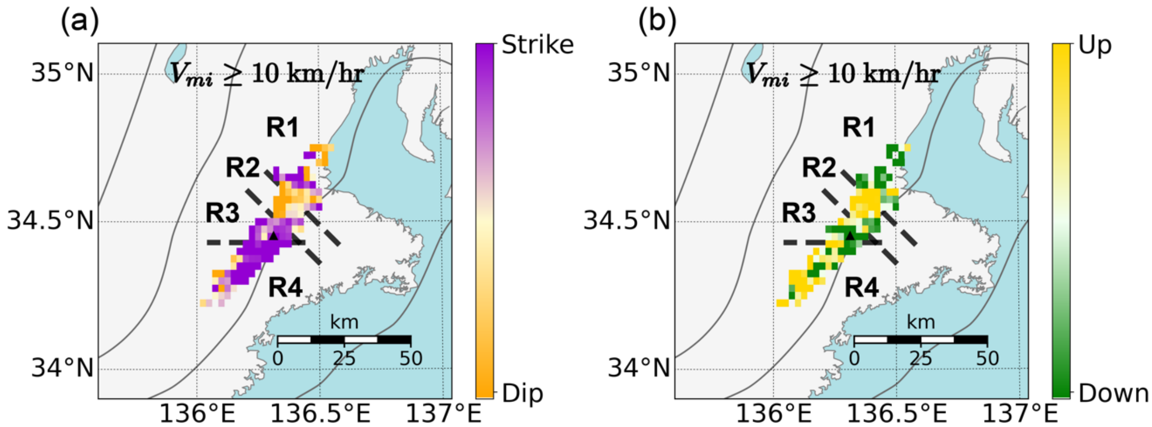

Figure S13. (**a**) Spatial distribution of predominant directions of tremor migrations with speeds of 10 km/hr or more. The black triangle shows the location of the array. The dashed lines are drawn to distinguish the areas R1–R4, where the frequency of tremor events composing tremor migrations is high. The violet color shows that tremor migrations along the strike are predominant (0–90° and 180–270° clockwise from the north), and the orange color shows that tremor migrations along the dip are predominant (90–180° and 270–360°). (**b**) Spatial distribution of predominant directions of tremor migrations with high speeds along the dip. The yellow and green colors show predominant directions of the up-dip (90–180°) and down-dip (270–360°), respectively.

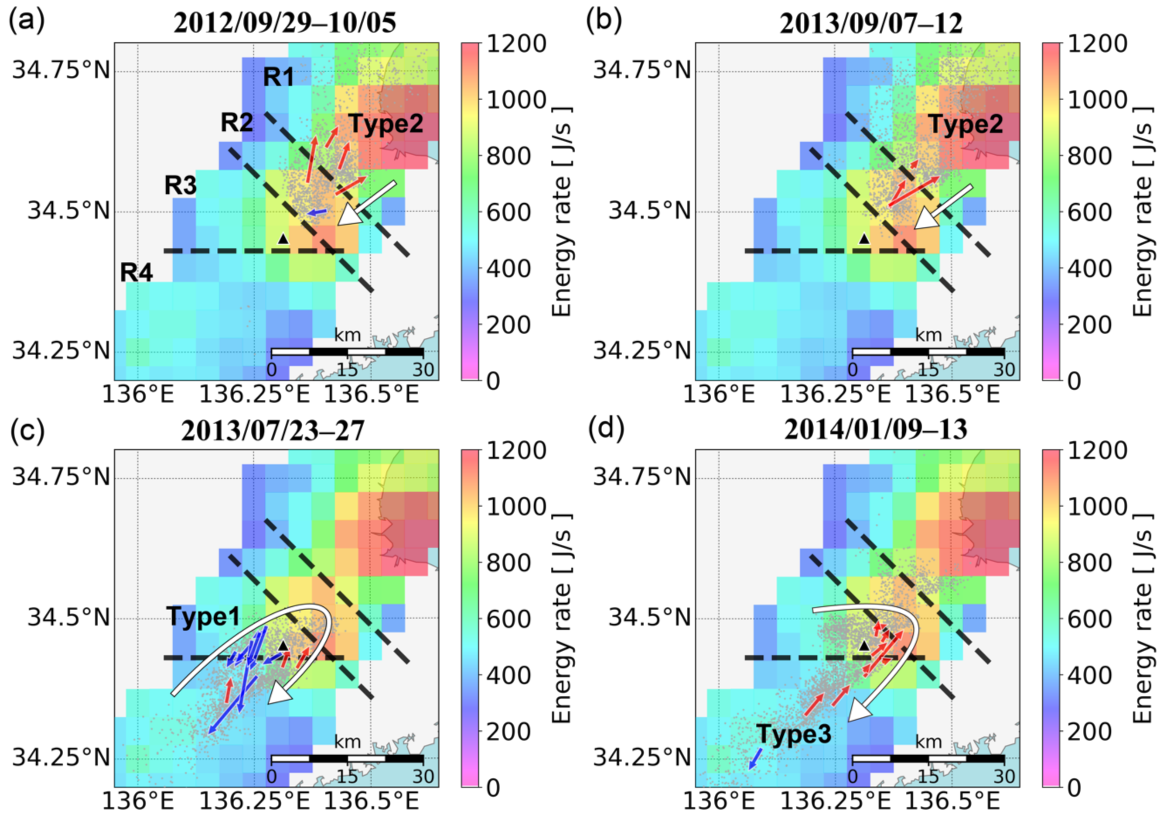

Figure S14. (**a**) Spatial distribution of RTRs during a tremor episode from September 29th to October 5th, 2012. The red arrows show RTRs propagating northeastward, and the blue arrows show those propagating southwestward. The white arrow shows the pattern of the main front and the gray dots show tremor locations. Type1–Type3 show different migration patterns of RTRs. The dashed lines and the black triangle are the same as Figure S13. The background colors show median energy rates (Yabe & Ide, 2014). (**b**) Same as (**a**), but for RTRs during a tremor episode from September 7th to 12th, 2013. (**c**) Same as (**a**), but for RTRs during a tremor episode from July 23rd to 27th, 2013. (**d**) Same as (**a**), but for RTRs during a tremor episode from January 9th to 13th, 2014.

Data Set S1. The catalog of tremor migrations extracted in the present study.

The data format is the followings: Year, Month, Day, Hour, starting time [min], ending time [min], longitude of starting point [deg], longitude of ending point [deg], latitude of starting point [deg], latitude of ending point [deg], ρ [km], migration speed [km/hr], ϕ [deg], and ψ [deg]. The starting time and ending time are elapsed time from Year-Month-Day Hour: 00:00. Time zone is Japan Standard Time (JST, UTC+9). ϕ is the migration direction measured counterclockwise from the east.